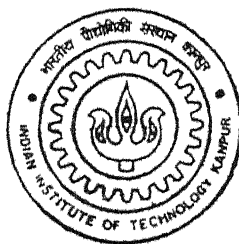


Active Modal Vibration Control of a Car Structure using Discrete PVDF Actuators and Sensors

by
R.Ajay Kumar

TH
AE/2000/M
K96a



DEPARTMENT OF AEROSPACE ENGINEERING
INDIAN INSTITUTE OF TECHNOLOGY, KANPUR

March, 2001

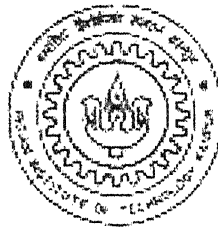
Active Modal Vibration Control of a Car Structure using Discrete PVDF Actuators and Sensors

A Thesis Submitted
in partial fulfilment of the Requirements
for the Degree of

Master of Technology

By

R.Ajay Kumar



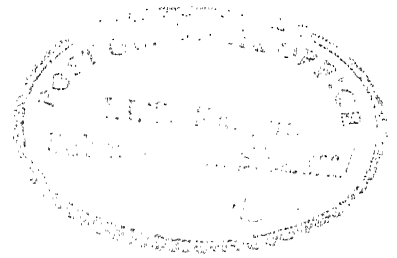
**Department of Aerospace Engineering.
Indian Institute of Technology Kanpur
Kanpur- 208016
India
March, 2001**

133654



A133654

CERTIFICATE



It is certified that the work contained in the thesis entitled **“Active Modal Vibration control of a Car Structure using Discrete PVDF Actuators and Sensors”** by R. Ajay Kumar, has been carried out under my supervision and that this work has not been submitted elsewhere for a degree.

March 1 , 2001

S. Kamle

Dr. Sudhir Kamle

Department of Aerospace Engineering
Indian Institute of Technology, Kanpur

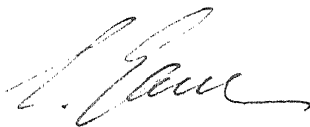
CERTIFICATE

It is certified that the work contained in this thesis entitled
**“ Active Modal Vibration Control of a Car Structure using Discrete PVDF Actuators
and Sensors ”**

by

Mr. R.Ajay Kumar

has been carried out at
Institut A für Mechanik, Universität Stuttgart, Germany,
under the supervision of the undersigned.
This work is not been submitted elsewhere for the award of a degree.



Prof. Dr.-Ing. habil. Lothar Gaul
(Director)
Institute A für Mechanik
Pfaffenwaldring 9, D-70550
Stuttgart

Dedicated

to my

Parents and Teachers

Acknowledgement

I would like to thank my thesis guides Dr. Sudhir Kamle, Associate professor Aerospace Engineering Dept., IIT Kanpur and Prof. Dr.-Ing. habil. Lothar Gaul, Director of Institute A of Mechanics, University Stuttgart, for giving me all the encouragement and support to go ahead with this thesis work. This work would never have been possible but for their guidance and the interest they have shown to me.

I would also like to thank Prof. Dr. N.G.R. Iyengar , Head, Aerospace Engineering Dept. IIT Kanpur, for being a constant source of encouragement and support throughout my stay in IIT Kanpur.

I thank Dipl.-Ing. Uwe Stöbener and Dipl.-Ing. Oliver Fein without whom this project would never have taken off and seen light. I thank them for their constant support all throughout this thesis work.

I thank Mr. Kantesh Balani and Mr. Jinu Paul for being there with me always, and for being a constant source of enlightenment throughout my stay in Stuttgart. They have helped me see through all the lean periods of my stay.

I would fail in my deeds if I don't thank the DAAD batch of students Mr. Phanender Naidu, Mr. Abhijit Sathe, Mr. Vikas Tomar, Mr. Sauvik Banerjee, Mr. Tushar Kandeparkar, Ms Debola Banerjee, Ms. Madhulika Joshi and Ms. Sharmista Sarkar, for their support and encouragement.

Lastly, I thank my Parents and my brothers who have always been there with me and given me the confidence that I can do anything. All that I have achieved and am going to, belongs to them.

R. Ajay Kumar

Contents

Nomenclature	a
List of tables	c
List of figures	d
Synopsis	f
1 Introduction	1
1.1 Motivation for adaptive structures	1
1.2 Adaptive structures terminology	2
1.3 Piezoelectric phenomena	3
1.4 Distributed sensing and vibration control	3
2 The Euler-Bernoulli - Beam	5
2.1 Euler equation for a beam	5
2.2 Modal summation procedure for a beam	8
2.3 Modelling of beams with piezoelectric actuators	10
2.4 Modelling of beams with piezoelectric sensors	14
2.5 Modal amplitudes for excitation by a point sinusoidal excitation and excitation by the actuator	18
3 Modal state space formulation and modal control	19
3.1 Modal state space description for a beam with external excitation	20
3.2 State space form with included modal actuator input	21
3.3 State space form with included sensor output	22
3.4 Active beam with sensors and actuators	23
3.5 Modal control	24
3.5.1 Independent modal space control (IMSC)	24
3.6 Determination of modal gains – Pole allocation	26
3.6.1 Pole allocation	27
3.7 Stability	29
4 Actuator and sensor placements	31
4.1 Norms	32
4.1.1 The H_2 Norm	32
4.1.2 The H_∞ Norm	33
4.1.3 Additive property for a set of actuators / sensors for each mode	34
4.2 Actuator placement	35
4.2.1 Actuator placement indices matrix	35
4.2.2 Control performance indices	36
4.2.3 Design procedure	36
4.3 Sensor placement	37
4.3.1 Sensitivity of single sensor	37
4.3.2 Condition of output matrix	37
4.3.3 Design procedure	38
5 Active vibration control of a beam – simulation and experimental results	40

5.1	Material properties	40
5.2	Modal parameters	41
5.3	Actuator placements	41
5.4	Sensor placements	43
5.5	Simulation	44
5.5.1	Transient vibration	44
5.5.2	Steady state vibration	45
5.6	Bonding procedure	46
5.6.1	PZT actuators	46
5.6.2	PVDF sensors	46
5.7	Experimental set – up	47
5.8	Experimental results	48
6	Active structural and acoustic control of a car structure	50
6.1	Sound radiation of a vibrating surface – the Rayleigh integral	51
6.2	Experimental modal analysis	53
6.2.1	Used hardware	53
6.2.2	Building blocks of the FRF measurement	54
6.2.3	Estimating the frequency response function	54
6.2.4	Post processing	56
6.3	Input and output matrices for plate with distributed PVDF materials	56
6.3.1	Input matrix	56
6.3.2	Output matrix	58
6.4	Interpolation of a shape function	59
6.4.1	Interpolation by using Lagrangian polynomials	59
6.4.2	Determination of coefficients of the Lagrangian polynomials	60
6.5	Experiments and results	61
6.5.1	Set up for experimental modal analysis of the car structure	61
6.5.2	Results of experimental modal analysis	62
6.5.2.1	EMA results with passive damping coat	64
6.5.3	Experimental set up for sound pressure measurement	65
6.5.4	Results of sound pressure measurement	66
6.5.5	Interpolated mode shapes of control modes	68
6.6	Actuator and sensor placements	69
6.6.1	Actuator placement	69
6.6.2	Sensor placement	71
6.7	Experimental set up for vibration control	74
6.8	Experimental results of vibration control	75
7	Summary	80
8	Conclusion / Scope for future work	81
	Bibliography and References	i
	Appendix 1-5	iv

Nomenclature

Symbol	Description
ω_n	natural frequency of n^{th} mode
ζ_n	damping ratio of the n^{th} mode
Ψ_n	normalised mode shape of n^{th} mode
q_n	modal coordinate of the n^{th} mode
\hat{q}_n	modal amplitude of the n^{th} mode
x, y	Cartesian coordinates
ξ	natural coordinate
$[A]$	modal system matrix
$[B], b_n \text{ \& } B_n$	modal input matrix, modal input factor
$[C], C_n$	modal output matrix, modal output factor
$[G]$	gain matrix
$\{x\}$	state variable vector
$\{y\}$	sensor output vector
$\{r\}$	control vector
$\{h\}$	force input vector
G_{FF}, G_{XX}	auto power spectrum
G_{FX}	cross power spectrum
γ^2	coherence
$\tilde{\Psi}$	modal output factor
A	area of cross section
A_e	electrode area
C	capacitance
d_{31}, d_{32}	piezoelectric constant
D_i	electric displacement

E_3	applied electric field
C_s	bending slope
m_x, m_y	line moments
t_p	plate thickness
U	applied voltage
R	resistance
q	charge
ε	permittivity
s	elastic compliance
$S, \varepsilon_{pe}, \varepsilon_0$	strain in the material
T, σ	stress in the material / σ - used as placement index also
$G(\omega)$	transfer function
tr	trace of a matrix
K^f	piezoelectric geometric constant
E	Young's modulus of the material
$\ G\ _2$	system H_2 norm
$\ G\ _\infty$	system H_∞ norm
$\alpha_{a2}, \alpha_{a\infty}, \beta_{a2}, \beta_{a\infty}$	control performance indices
i_s	measurability index
n_c	number of modes to control

Subscripts

a	actuator
b	beam
pe	piezoelectric element
s	sensor
p	plate

Superscripts

E	value measured at constant electric field
T	value measured at constant stress

List of Tables

1.1 Smart materials and examples of their application	2
5.1 Properties of the beam	40
5.2 Properties of the PVDF and PZT materials used in the experiment	41
5.3 Modal parameters of the beam specimen	41
5.4 Coordinates of the actuators	42
5.5 Control performance indices of the actuator location	42
5.6 Coordinates of the sensor on the beam	43
5.7 Performance indices of the selected sensor placements on the beam	43
5.8 Amplitude reduction after control	48
6.1 Eigen frequencies and damping ratios	63
6.2 Modes selected for control of sound radiation	67
6.3 Position of PVDF actuators on the car hood	79
6.4 Control performance indices for actuator locations	71
6.5 Position of PVDF sensors on the car hood	72
6.6 Performance indices for selected sensor combination	73

List of figures

1.1 Terminology of adaptive structures	2
2.1 Beam section with stress resultants	5
2.2 Asymmetric wafer configuration	12
2.3 Antisymmetric wafer configuration	13
2.4 Measurement of sensor voltages using (a) Resistance and (b) Capacitance	17
3.1 State space form of a linear system	19
3.2 System with external excitation	21
3.3 System with actuator input B	22
3.4 System with sensor output matrix C	23
3.5 Block diagram of the active beam with the sensors and actuators	23
3.6 Modal filtered feedback (IMSC) block diagram	25
3.7 Single degree of freedom oscillator (a) Open-loop and (b) Closed-loop poles	29
4.1 H_2 and H_∞ norms (a) of the second mode and (b) of the system	34
5.1 Placement of the actuators on the beam	40
5.2 FRF of the shaker and actuator induced excitation	41
5.3 Sensor placement on the beam	43
5.4 Simulated modal displacement vs time plot of (a) first and (b) fourth mode	44
5.5 Spillover effect on the seventh mode	45
5.6 Simulated modal displacement vs time plot for fourth mode (a) without and (b) with control	45
5.7 Bonding of PZT actuators	46
5.8 Bonding of PVDF sensors	47
5.8 Experimental set up for vibration control of the beam	47
5.9 Modal velocity vs time plot for the fourth mode	49
5.10 Acceleration vs frequency plot for the beam vibration control	49
6.1 General arrangement for ASAC	50
6.2 An elemental sound source associated with plate radiation	51
6.3 Corner monopole model of low frequency plate radiation	52
6.4 Schematic representation of basic hardware for modal testing	53
6.5 FRF measurement system model	54
6.6 Two dimensional piezoelectric wafer element on a plate structure	56
6.7 Cross-section of the plate with the actuators on top and bottom	57
6.8 Experimental set up for experimental modal analysis	62
6.9 Frequency response function	63
6.10 First four mode shapes of the hood	64
6.11 FRF of passive damped hood	65
6.12 Sound pressure measurement set up	65
6.13 Bar chart of the sound pressure measurement	66
6.14 Sound pressure with and without passive damping coat	67
6.15 Measured and interpolated mode shapes	69
6.16 Positions of the PVDF actuators on the car hood	70
6.17 FRF shapes of the shaker and actuator induced sinusoidal excitation	71
6.18 Sensor positions on the car hood	72
6.19 PVDF actuators/sensors placed on (a) top and (b) bottom of the hood	73

6.20 Experimental set up for vibration control	74
6.21 Photograph of the experimental set up for the control of Car hood vibration	75
6.22 Measured acceleration at two points on the hood	76
6.23 Force variation over frequency range	76
6.24 Sound pressure measurement of the car hood with and without control	77
6.25 Modal velocity -time plot for third mode of control- 237 Hz	78
6.26 Comparison plot of modal velocity -time with and without control	78
6.27 Sound pressure measurement of hood vibration control with passive coat	79
6.28 Measured acceleration of hood vibration control with passive coat	79

Synopsis

Structural vibration of a car body, caused by the engine propagates as structure borne sound from its source to the hood. The problem lies in controlling the sound radiation by controlling the vibration of those modes which couple effectively to the acoustic media.

An experimental investigation has thus been performed to determine the feasibility of implementing polyvinylidene flouride (PVDF) as error sensors on the surface of a car hood in a Modal filtered feedback approach to minimise the acoustic radiation . To this end, three PVDF sensors are positioned on the car hood such that the dominant observed responses are due to those modes which are more efficient acoustic radiators. Distributed PVDF actuators are utilised to control vibration of these modes. As a pre-test experiment, the Modal filtered feedback algorithm is first implemented to control the vibration of a simply supported beam with four actuators and sensors. The actuator and sensor placements are decided based on the placement and performance indices which are in-effect dependent on the system and modal norms, outlined by Gawronski in [4]. The modal controller is implemented on a digital controller board by downloading the algorithm from Matlab simulink.

Further more, an active-passive hybrid treatment for control of vibration and sound radiation is investigated by applying a viscoelastic passive damping coat on to the car hood . This approach shows much reduction in sound radiation as the passive materials are good in controlling modes in the higher frequency range, while active control could be utilised to control the modes in the lower frequency band.

Results from these experiments indicate that the PVDF sensors and actuators show much promise for controlling acoustic radiation from the hood, to a large degree overcoming the need for error microphones in the far field. In addition, the Modal filtered feedback proves to be a very productive constrained control algorithm.

Chapter 1

Introduction

The thrust of current research has been to develop intelligent structures that can adapt to their environment such that undesired vibration or acoustic radiation can be minimized. The chapter focuses on the development of this field and its applications briefly. It also gives a general outlay of the control of distributed continuum especially focussing on the Modal control.

1.1 Motivation for Adaptive Structures

Adaptation is typically associated with the modification, change, or adjustment that might occur over some period of time. In biology, adaptation is considered to be a characteristic of an organism that makes it better able to live in its environment. The concept of an adaptive structure is thus biologically inspired and is motivated by the need to modify a structure's response to various stimuli (disturbances) and environmental conditions (design uncertainties) to meet some predetermined response characteristics. Control system design forms a critical path in the development of an adaptive structure and essentially classifies the level of adaptation possible.

The evolution of the adaptive structures technology, and its current knowledge base, was made possible by the explosive growth in the microprocessor industry over the past decade. Digital parameters are more readily adjusted than their analog equivalents, which leads to a real capability to provide adaptation in an online environment. The other critical element for adaptive structure design has been the development of material technologies, primarily electromechanical materials, also well known as smart materials. Table 1.1 gives the names of some smart materials and their applications.

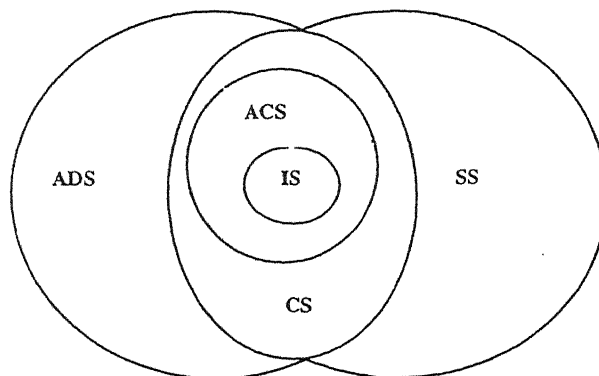
No.	Smart material.	Application.	Example.
1.	Piezoelectric materials	As actuators and sensors	PZT, PVDF
2.	Magnetostrictive materials	As actuator	TERFENOL-D
3.	Shape Memory Alloys (SMA)	As actuator and sensor	NITINOL
4.	Optical fibers	As sensor	Optical fiber

Table 1.1 : Smart materials and examples of their applications

Piezoelectric materials have a recoverable strain of about 0.1 % under electric field. The Magnetostrictive materials have a recoverable strain of about 0.15 % under magnetic field; the maximum response is obtained when the material is subjected to compressive loads. SMAs allow one to recover up to 5 % strain from phase change induced by temperature.

1.2 Adaptive Structure Terminology

The various descriptive terms for adaptive structures were outlined by Wada et al. (1990). fig1.1 illustrates various types of structural entities defined as a subset of other fields of research. As seen in the figure, Intelligent structure (IS) was reserved for those structures which incorporate actuators and sensors that are highly integrated into the structure and have structural functionality, as well as highly integrated control logic, signal conditioning and power amplification electronics. This would be the final stage of the ongoing research in this field.



ADS = Adaptive structure (structures having actuators)

SS = Sensory structure (structures having sensors)

CS = Controlled structure (ADS with closed loop control)

ACS = Active structures (Structures serving some function in the load bearing properties of the system)

Fig 1.1 : Terminology of adaptive structures

The definition of CS is more suited for the experimental works carried out on the beam and hood. The active control is achieved by using piezoelectric polymers namely PVDF and PZT as actuators and sensors. A brief note of the piezoelectric phenomena is thus presented in next section.

1.3 Piezoelectric Phenomena

The discovery of piezoelectric phenomena in 1880 led science and technology into a new dimension. The first observation of piezoelectric phenomena was done by the Curie brothers. Piezoelectricity is an electromechanical phenomena which couples the elastic (dynamic coupling) and electric (static coupling) fields. In general, a piezoelectric material responds to mechanical forces/pressures and generates an electric charge/voltage. This phenomenon is called direct piezoelectric effect. Conversely, an electric charge/field applied to the material induces mechanical stresses or strains, and this phenomenon is called the converse piezoelectric effect. In active piezoelectric structures, the direct effect is used for structural measurements and converse effects for active vibration controls of the continua. Generic theories of structures with distributed piezoelectrics have been explored by numerous researchers and most of the necessary theory has been outlined by Tzou in [5]. Some of the elastic, piezoelectric and dielectric relations have been summed up in Appendix 1. One drawback of the piezoelectric materials that is worth noting is that their performance is restricted by breakdown voltages, hysteresis effects and limited strain rates.

1.4 Distributed Sensing and Vibration Control

Structures are generally distributed in nature, i.e., structural behaviors are functions of time and space, hence called distributed parameter systems. Structural identification and control needs a close coordination of sensors and actuators. Conventional transducers and sensors are generally discrete, i.e., they measure spatially discrete locations of continuum. A severe problem can thus occur when these discrete transducers are placed at modal nodes and on nodal lines. The same problem arises when discrete actuators are used to control the continua. Eventually, these modes are neither observable nor controllable by these transducers and actuators. Thus, in order to observe and control the continua, distributed sensors and actuators are highly desirable. Thus distributed piezoelectric layers can be used as sensors and actuators for structural control applications.

Modal control is an approach to control a structure by controlling its modes. Modal control methods have come to the limelight in the last decade primarily because of the

availability of numerous sensors and actuators which render the control spillover ie ..coupling to truncated modes and unmodelled dynamics manageable. This control is popular because it appeals to our simplistic and intuitive notions of single degree of freedom systems. Mathematically, modal control derives its power from consideration of matrix de-coupling transformations. The Independent modal space control (IMSC) as outlined by Meirovitch [7] is used in the experiments with both the beam and car hood. This method suffers from a drawback that its implementation by point actuators implies control of reduced number of modes ie.. modal truncation. Another approach to control the structure is by using direct output feedback control, whereby sensors are collocated with actuators. Here the difficulty is in deciding the suitable control gains. A good sum up of the application of active modal control for Smart structures has been done by Inman in [18]. The ability to locate Piezoelectric sensors and actuators almost everywhere greatly improves a system's controllability and observability properties and hence allows modal control to become an useful approach. The modal control can be cast either in state space form or physical space form ie.. in terms of the physical modes of the mechanical system. Because of the difficulties in defining such physical modes for mechanical system, the state space approach is used in the experiments. However, the modes derived from the state space analysis can be thought of as being similar to those of the equivalent undamped mechanical system.

Chapter 2

The Euler – Bernoulli – Beam

The Beam is probably the best structure to try implementing the modal control concepts as it serves as a good platform to apply the same concepts to complex structures. This chapter intends to give a brief introduction to the theoretical modal analysis of a beam. It also includes the derivation of the actuator and sensor equations for piezoelectrics attached to a beam element.

2.1 Euler Equation for a Beam

Although it is well known, the derivation of the Euler-Bernoulli thin beam equation is presented here since it outlines the basic procedure used for the analysis of distributed piezoelectrics actuators and sensors attached to beams.

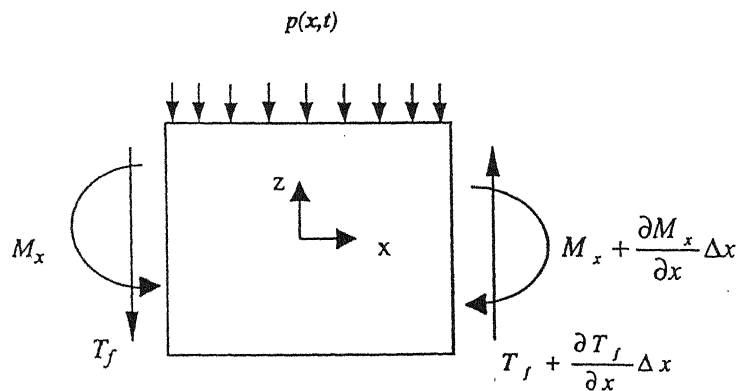


Fig: 2.1 Beam section with stress resultants

The figure above shows an element of a thin beam excited in pure bending . For the following derivation it is assumed that the beam cross-section is symmetrical about the center -line and remains normal to the neutral surface.

The longitudinal displacement u is given by

$$u(x) = -z \frac{\partial w}{\partial x} \quad (2.1)$$

where w is the out of plane displacement of the beam and z is the transverse coordinate of the beam section.

By Hook's law in one dimension the stress in the beam is given by

$$\sigma(z) = -zE \frac{\partial^2 w}{\partial x^2} . \quad (2.2)$$

The resulting moment in the beam can then be obtained by integrating the stress distribution over the beam cross section such that

$$M_x(x) = \int_{-h/2}^{h/2} \sigma(z) z dz, \quad (2.3)$$

which then reduces to

$$M_x(x) = -EI \frac{\partial^2 w}{\partial x^2} \quad (2.4)$$

where , $I = bh^3/12$, is the moment of inertia of the beam where b is the width and h is the height of the beam, respectively. Considering the beam element with the resultant shear forces and moments acting as shown and neglecting rotary inertia of the element, the condition of moment equilibrium gives:

$$\frac{\partial M_x}{\partial x} \Delta x = T_f \Delta x, \quad (2.5)$$

where M_x and T_f are the internal moment and transverse shear forces acting upon the element.

Applying Newton's law of motion in the vertical direction gives

$$-p(x) + \frac{\partial T_f}{\partial x} = \rho A \frac{\partial^2 w}{\partial x^2} . \quad (2.6)$$

Combining (2.6) and (2.5) the following is obtained

$$\frac{\partial^2 M_x}{\partial x^2} = \rho A \frac{\partial^2 w}{\partial t^2} + p(x, t)$$

and finally by using the above equation and (2.6) the Euler Bernoulli equation of beams can be obtained as

$$EI \frac{\partial^4 w}{\partial x^4} + \rho A \frac{\partial^2 w}{\partial t^2} = -p(x, t) \quad (2.7)$$

where $p(x, t)$ is the external load or forcing function (with units of force/unit length) on the beam.

The homogeneous form of the above equation can be written as

$$EI \frac{\partial^4 w}{\partial x^4} + \rho A \frac{\partial^2 w}{\partial t^2} = 0 \quad (2.8)$$

A solution of the form given below can be assumed

$$w(x, t) = \Psi(x) T(t) = \Psi(x) \text{Im} \{e^{i\alpha x}\} \quad (2.9)$$

with $\psi(x)$ as the modal form-function.

By substituting (2.9) in (2.8) the homogeneous differential equation unfolds as

$$\frac{d^4 \Psi}{dx^4} - \lambda^4 \Psi = 0, \quad (2.10)$$

with , $\lambda^4 = \frac{\rho A}{EI} \omega^2$.

The solution of the above differential equation is given by

$$\Psi(x) = A_1 \cosh \lambda x + A_2 \cos \lambda x + A_3 \sinh \lambda x + A_4 \sin x \quad (2.11)$$

Writing down equation (2.8) in the dimensionless form the following can be obtained

$$EI_{yy} \frac{\partial^4 w}{\partial \xi^4} + l^4 \rho A \frac{\partial^2 w}{\partial t^2} = 0. \quad (2.12)$$

One could express the fourth order differential equation in (2.10) as

$$\frac{d^4 \Psi}{d\xi^4} - \kappa^4 \Psi = 0, \quad (2.13)$$

where, $\kappa^4 = \frac{\rho A l^4}{EI_{yy}} \omega^2 = \lambda^4 l^4$.

The dimensionless form of the solution of the differential equation now becomes

$$\Psi(\zeta) = A_1 \cosh \kappa \zeta + A_2 \cos \kappa \zeta + A_3 \sinh \kappa \zeta + A_4 \sin \kappa \zeta \quad (2.14)$$

The constants can be found out by applying the appropriate boundary conditions of the beam under consideration.

Considering a simply supported beam,

$$\Psi(0) = 0 : \quad A_1 + A_2 = 0 \quad (2.15)$$

$$\Psi(l) = 0 : \quad A_1 \cosh \kappa + A_2 \cos \kappa + A_3 \sinh \kappa + A_4 \sin \kappa = 0 \quad (2.16)$$

$$\Psi''(0) = 0 : \quad A_1 - A_2 = 0 \quad (2.17)$$

$$\Psi''(l) = 0 : \quad A_1 \cosh \kappa - A_2 \cos \kappa + A_3 \sinh \kappa - A_4 \sin \kappa = 0 \quad (2.18)$$

The natural frequencies of vibration are found by substituting the above value in the equation (2.13) which yields :

$$\frac{d^4 \Psi_n}{d\xi^4} = n^4 \pi^4 \sin(n\pi\xi), \quad (2.19)$$

As $\sinh \kappa \neq 0$ we have that the constants $A_1 = A_2 = A_3 = 0$, and hence $A_4 \sin \kappa = 0$. As $A_4 \neq 0$,

$\sin \kappa = 0$. The solution of which is $\kappa = n\pi$ where $n \in \mathbb{N}^+$.

Thus the eigen form-function can be written as $\Psi_n(\xi) = \sin(n\pi\xi)$.

Solution of the above expression gives,

$$\sin(n\pi\xi)[n^4 \pi^4 - \lambda^4 l^4] = 0. \quad (2.20)$$

This ultimately leads to the solution

$$(n\pi)^4 = (\lambda l)^4. \quad (2.21)$$

Substituting for λ and solving yields

$$\omega_n = \frac{n^2 \pi^2}{l^2} \sqrt{\frac{EI_{yy}}{\rho A}}. \quad (2.22)$$

2.2 Modal Summation Procedure for a Beam

One could write the distributed force in the right hand side of the Euler-Bernoulli equation as a harmonic function as written below

$$p_z(x, t) = \hat{p}_z \operatorname{Im}\{e^{i\Omega t}\}, \quad (2.23)$$

and the displacement $w(x, t)$ can also be written down in the form

$$w(x, t) = \hat{w}(x) \operatorname{Im}\{e^{i\Omega t}\}. \quad (2.24)$$

Now writing the Euler-Bernoulli equation in the dimensionless form with the natural coordinate ξ ,

$$EI_{yy} \frac{\partial^4 w}{\partial \xi^4} + l^4 \rho A \frac{\partial^2 w}{\partial t^2} = l^4 p(x, t). \quad (2.25)$$

Substituting (2.23) and (2.24) in (2.25) the following equation is obtained

$$EI_{yy} \frac{\partial^4 w}{\partial \xi^4} - l^4 \rho A \Omega^2 \hat{w} = l^4 \hat{p}_z \quad (2.26)$$

The space function part of $w(\xi, t)$ can now be written down as the sum of the product of the amplitude and the form-function as

$$\hat{w}(\xi) = \sum_{n=1}^{\infty} \hat{q}_n \Psi(\xi) \quad (2.27)$$

where \hat{q}_n is the modal amplitude of vibration.

Substituting the above equation in (2.26) the modified differential equation is

$$\sum_{n=1}^{\infty} \hat{q}_n (EI_{yy} \frac{\partial^4 \Psi_n}{\partial \xi^4} - l^4 \rho A \Omega^2 \Psi_n) = l^4 \hat{p}_z. \quad (2.28)$$

For a free vibrating beam the homogeneous beam equation is given by

$$\sum_{n=1}^{\infty} \hat{q}_n (EI_{yy} \frac{\partial^4 \Psi_n}{\partial \xi^4} - l^4 \rho A \omega_n^2 \Psi_n) = 0 \quad (2.29)$$

with ω_n as the n^{th} natural frequencies of the beam.

Subtracting (2.28) from (2.29) the following equation is obtained

$$\sum_{n=1}^{\infty} \hat{q}_n \rho A (\omega_n^2 - \Omega^2) \Psi_n = \hat{p}_z. \quad (2.30)$$

The normal modes $\Psi_n(\xi)$ are also orthogonal functions satisfying the relations

$$\int_0^1 \Psi_n(\xi) \Psi_m(\xi) d\xi = \begin{cases} 0 & \text{for } n \neq m \\ const & \text{for } n = m \end{cases} \quad (2.31)$$

Hence multiplying (2.30) with $\Psi_n(\xi)$ and then integrating the equation over the limits 0 and 1 it could be obtained that

$$\hat{q}_n \rho A (\omega_n^2 - \Omega^2) \int_0^1 \Psi_n^2(\xi) d\xi = \int_0^1 \hat{p}_z \Psi_n(\xi) d\xi. \quad (2.32)$$

In the above equation the constant is called the norm, and is denoted by Λ_n

$$\Lambda_n = \int_0^l \Psi_n^2(\xi) d\xi. \quad (2.33)$$

The modal amplitude of vibration can be written as

$$\hat{q}_n = \frac{\int_0^l \hat{p}_z \Psi_n(\xi) d\xi}{\rho A (\omega_n^2 - \Omega^2) \Lambda_n}. \quad (2.34)$$

The damping effects of the beam can now be included by replacing the Young's modulus of the beam by the complex formulation $E' + iE''$, with E' as the storage modulus and E'' as the loss modulus. The loss factor η is defined as the coefficient E'/E'' .

Hence the equation (2.28) can be modified as

$$EI_{yy} (1 + i\eta) \frac{\partial^4 \Psi_n}{\partial \xi^4} - l^4 \rho A \Omega^2 \Psi_n = l^4 \hat{p}_z. \quad (2.35)$$

Including also the effect of damping into the eigen-frequency yields

$$\omega_n^2 = \omega_n^2 (1 + i\eta) \quad (2.36)$$

and therefore (2.34) can be written as

$$\hat{q}_n = \frac{\int_0^l \hat{p}_z \Psi_n(\xi) d\xi}{\rho A (\omega_n^2 (1 + i\eta) - \Omega^2) \Lambda_n}. \quad (2.37)$$

Multiplying the numerator and denominator of the above equation by its complex conjugate one could obtain

$$\hat{q}_n = \frac{(\omega_n^2 - \Omega^2) - i(\omega_n^2 \eta)}{\rho A \Lambda [(\omega_n^2 - \Omega^2)^2 + \omega_n^4 \eta^2]} \int_0^l \hat{p}_z \Psi_n(\xi) d\xi. \quad (2.38)$$

Taking the modulus of the complex modal amplitude yields

$$|\hat{q}_n| = \frac{\sqrt{(\omega_n^2 - \Omega^2)^2 + \omega_n^4 \eta^2}}{\rho A \Lambda [(\omega_n^2 - \Omega^2)^2 + \omega_n^4 \eta^2]} \int_0^l \hat{p}_z \Psi_n(\xi) d\xi. \quad (2.39)$$

2.3 Modelling of Beams with Piezoelectric Actuators

The common form of arrangement of the Piezoelectric actuator is the anti-symmetric wafer configuration. In this arrangement two identical piezoelectric elements are located

voltage is applied across the electrodes (in the direction of polarization) the actuator induces surface strains in the beam through the d_{31} and d_{32} mode of the piezoelectric material response. This configuration is known as the wafer arrangement since the piezoelectric element is very long (in the x and y directions) compared to thickness (in the z direction) through which it is polarised.

One dimensional antisymmetric wafer actuators

Important assumptions for this configuration are :

- ❖ the beam is covered by a layer of thin piezoelectric material of thickness, h_a which is perfectly bonded to the beam and strains only in the x direction.
- ❖ inertial effects of the piezoelectric element are ignored which is valid if the element is thin and lightweight compared to the beam system.

When a voltage is applied across the unconstrained layer (i.e.. not attached) piezoelectric element the actuator will strain by an amount ϵ_{pe} in the direction 1 which is parallel with the axis as dictated by

$$\epsilon_{pe} = \frac{d_{31}U_a}{h_a} \quad (2.40)$$

where U_a is the applied voltage in the direction of polarization , h_a is the actuator thickness and d_{31} is the piezoelectric material strain constant.

By the assuming that the strain distribution is linear as a result of Kirchoff's hypothesis of laminate plate theory it can be written that

$$\epsilon_b(z) = Cz + \epsilon_0, \quad (2.41)$$

where C is the slope and ϵ_0 is the z intercept. The above equation can be decomposed into the sum of a antisymmetric distribution Cz – due to the flexural component - about the center of the beam and a uniform strain distribution ϵ_0 - due to the longitudinal component . It must be stated here that the longitudinal component is present only in the case of asymmetric wafer arrangement with only one actuator attached to one side of the beam. In case of antisymmetric wafer arrangement, which was investigated in this research, pure bending occurs and the longitudinal component vanishes, i.e. $\epsilon_0=0$. The figure below shows the above stated decomposition for a asymmetric wafer configuration.

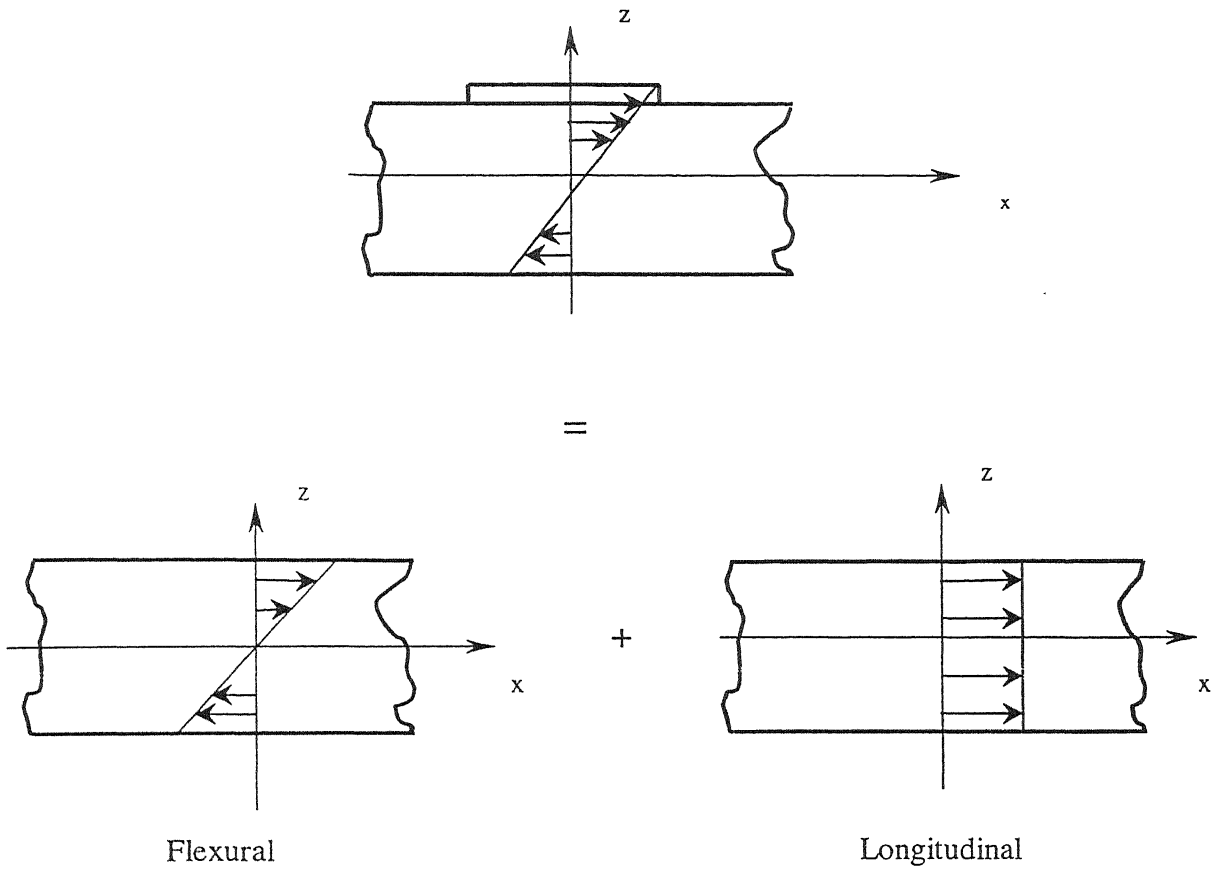


Fig : 2.2 Asymmetric wafer configuration

With the linear strain distribution and Hooke's law , the stress distribution within the beam is given by

$$\sigma_b(z) = E_b (Cz + \varepsilon_0) \quad (2.42)$$

where E_b is the Young's modulus of the beam material. The stress distribution within the piezoelectric actuator $\sigma_{pe}(z)$ is a function of the unconstrained piezoelectric actuator strain, the Young's modulus of the actuator material E_{pe} .

Thus the stress distribution can be written as

$$\sigma_{pe}^1(z) = E_{pe} (Cz + \varepsilon_0 + \varepsilon_{pe}) \quad (2.43)$$

$$\sigma_{pe}^2(z) = E_{pe} (Cz + \varepsilon_0 - \varepsilon_{pe}) \quad (2.44)$$

Now applying moment equilibrium about the center of the beam,

$$\int_{-h_b-h_a}^{-h_b} \sigma_{pe}^2(z) z dz + \int_{-h_b}^{h_b} \sigma_b(z) z dz + \int_{h_b}^{h_b+h_a} \sigma_{pe}^1(z) z dz = 0 \quad (2.45)$$

where the superscripts 1 and 2 denote the piezoelectric elements as shown in the fig. 2.3.

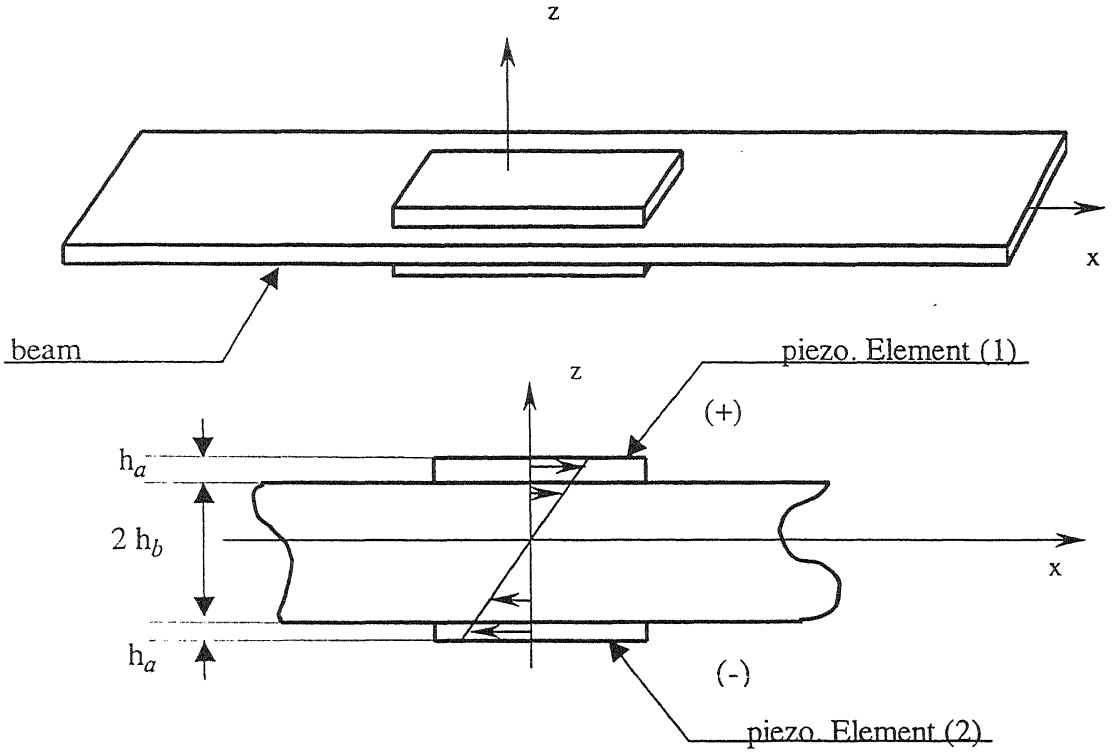


Fig : 2.3 Antisymmetric wafer configuration

After substitution of (2.42), (2.43) and (2.44) in (2.45) the strain slope C is obtained as

$$C = K^f \varepsilon_{pe} \quad (2.46)$$

where the material-geometric constant is specified by,

$$K^f = \frac{3E_{pe}[(h_b + h_a)^2 - h_b^2]}{2\{E_{pe}[(h_b + h_a)^3 - h_b^3] + E_b h_b^3\}} \quad (2.47)$$

The line moment m_x induced in the beam by the actuator is again given by

$$m_x(x) = E_b I K^f \varepsilon_{pe} \quad (2.48)$$

Now writing the Euler-Bernoulli equation of the beam in the moment form including the actuator induced moments, the beam – actuator equation of motion is given by,

$$\frac{\partial^2 [M_x(x) - m_x(x)]}{\partial x^2} - \omega^2 \rho A w = 0 \quad (2.49)$$

where M_x is the internal beam bending moment as shown in fig 2.1 and $m_x(x)$ is the actuator-induced line moment.

For a finite element length L_a of actuator the actuator-moment equation can be modified as

$$m_x(x) = C_0 \varepsilon_{pe} [H(x) - H(x - L_a)] \quad (2.50)$$

where $H(\cdot)$ stands for the unit Heaviside step function defined as

$$H(x) = \begin{cases} 1, & x > 0 \\ 0, & x < 0 \end{cases}$$

and

$$C_0 = E_b I K^f.$$

The above equation implies that the induced moment only exists at every point under the location of the finite actuator. Substituting the moment equation into (2.49), taking the second partial derivative with respect to x and moving the actuator terms to the right hand side of the equation one find

$$\frac{\partial^2 M_x(x)}{\partial x^2} - \omega^2 \rho A w = C_0 \varepsilon_{pe} [\delta'(x) - \delta'(x - L_a)] \quad (2.51)$$

where $\delta'(\cdot)$ represents the derivative of the Dirac delta function with respect to its argument.

Hence by substituting the force per unit length $p_z(x)$ in the Euler-Bernoulli equation corresponding to the actuator force as

$$\hat{p}_z(x) = C_0 \varepsilon_{pe} [\delta'(x) - \delta'(x - L_a)] \quad (2.52)$$

2.4 Modelling of Beams with Piezoelectric Sensors

Point sensors are usually employed in arrays of transducers whose outputs are processed to obtain some estimate of a required variable or state of the system to be controlled. The basis of this approach is that in order for the control to be effective with out observation spillover, the controller has to be designed to observe only those modes which are to be controlled. The main disadvantage of this approach is due to the signal processing requirements necessary to process the transducer outputs and thus obtain estimates of the required variables. The output of the sensor is sensitive to the accuracy of the shape of the sensor as well as its positioning on the structure.

Considering a one –dimensional thin beam covered with a thin layer of piezoelectric material .

- ❖ Its assumed that the piezoelectric material is mechanically isotropic and that the sensor has constant properties along its length and is also thin compared to its length.
- ❖ It is also assumed that the sensor has no effect on the motion of the beam , i.e. the stiffness and inertial force of the sensor are very small compared to the stiffness of the beam.

For a piezoelectric material the electrical and mechanical constitutive equations are coupled and in one-dimension they can be written as

$$S_{11} = s_{11}^E T_{11} + d_{31} E_3, \quad (2.53)$$

$$D_3 = d_{31} T_{11} + \epsilon_{33}^T E_3. \quad (2.54)$$

where,

D_3 is the charge per unit area expressed in Cm^{-2} ,

E_3 is the electric field applied in the poling direction expressed in Vm^{-1}

ϵ_{33}^T is the permittivity under constant stress.

d_{31} is the piezoelectric constant and relates the strain to the electric field E in the absence of mechanical stress. It is expressed in mV^{-1}

T_{11} is the stress in the material

s_{11}^E is the compliance of the piezoelectric material when the electric field is constant

S_{11} the strain in the material

The above equations can be transformed into

$$T_{11} = c_{11}^E S_{11} - e_{31} E_3, \quad (2.55)$$

$$D_3 = e_{31} S_{11} + \epsilon_{33}^T (1 - k^2) E_3. \quad (2.56)$$

where

$c_{11}^E = 1/s_{11}^E$ is the Young's modulus under constant electric field in Nm^{-2}

$e_{31} = d_{31}/s_{11}^E$ is the constant relating the charge per unit area to the strain for short circuited electrodes in Cm^{-2}

$k_{31}^2 = d_{31}^2 / (s_{11}^E \epsilon_{33}^T)$ is called the coupling coefficient of the piezoelectric material, a high value of which is desirable for efficient transduction.

$\epsilon_{33}^S = \epsilon_{33}^T (1 - k_{31}^2)$ is the permittivity under constant strain.

According to the Euler-Bernoulli assumption, the axial strain and the curvature are related by

$$S_{11} = (h_b + h_s) \frac{\partial^2 w}{\partial x^2} \quad (2.57)$$

where h_b is half the thickness of the beam and h_s is the thickness of the piezoelectric sensor.

If U_s is the voltage produced in the poling direction of the piezoelectric material by the deformation, then the electric field E_3 can be written as

$$E_3 = \frac{U_s}{h}. \quad (2.58)$$

Substituting the above equation in (2.56) yields

$$U_s = \frac{D_3 h_s}{\epsilon_{33} s} - \frac{e_{31} S_{11} h_s}{\epsilon_{33} s} \quad (2.59)$$

Defining the quantities:

$$\frac{q^c}{A} = D_3 = \text{free charge per area on the piezoelectric element.}$$

$$\frac{q_p}{A} = eS = \text{Piezoelectric polarization charge per area due to strain, where } A \text{ is the area of electrode}$$

In (2.59) the first term is Zero as there is no voltage applied to the material. Now after substituting the equation (2.58) in (2.59), and also including the aforesaid argument the following expression is obtained

$$U_s = -\frac{h_s}{\epsilon_{33} s} (h_b + h_s) (e_{31} \frac{\partial^2 w}{\partial x^2}). \quad (2.60)$$

It is desired to develop a modal sensor , i.e. a distributed piezoelectric sensor whose output is only related to the motion of one particular mode of the beam. The motion of the simply supported beam can be written as

$$w(x, t) = \sum_{n=1}^{\infty} q_n(t) \Psi_n(x). \quad (2.61)$$

Substituting (2.61) in (2.60) its found that,

$$U_s = \sum_{n=1}^{\infty} -q_n \frac{h_s}{\epsilon_{33} s} (h_b + h_s) e_{31} \frac{\partial^2 \Psi_n(x)}{\partial x^2}. \quad (2.62)$$

Though the concept of point sensors has been used, in reality, the sensors have some definite size. Hence an averaging over the length of the sensor has to be carried out. Thus the modified expression of U_s yields

$$U_s = \sum_{n=1}^{\infty} -q_n \frac{h_s}{\epsilon_{33} s} \frac{(h_b + h_s)}{l_s} e_{31} \int_{l_s} \frac{\partial^2 \Psi_n(x)}{\partial x^2} dx \quad (2.63)$$

where l_s is the length of the piezo sensor.

Now, this sensor voltage can be measured in two different ways either by using a resistor or by using a capacitor in parallel as shown in the figure below.

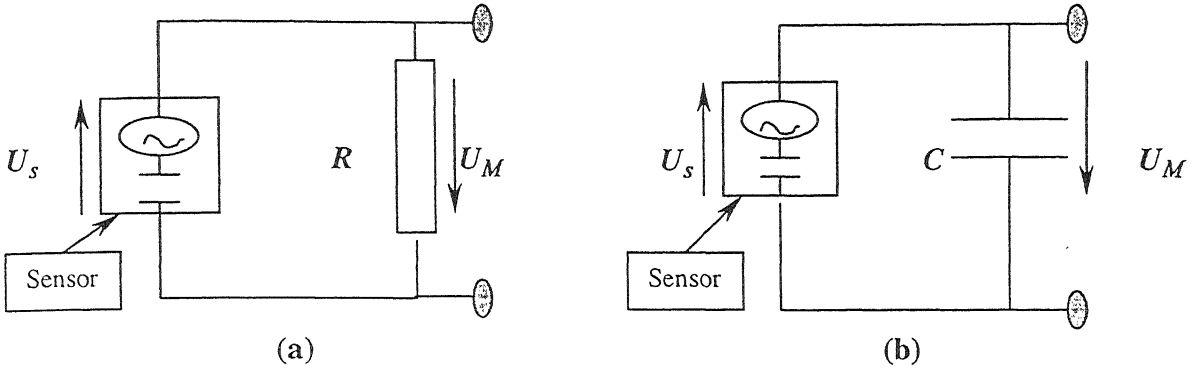


Fig 2.4 : Measurement of sensor voltages using (a) Resistance and (b) Capacitance

For a capacitor with capacitance C , the measured sensor voltage is given by,

$$U_M = Cq_p = C A e_{31} (h_b + h_s) \sum_0^{\infty} q_n \frac{1}{l_s} \int_0^{l_s} \frac{\partial^2 \Psi_n}{\partial x^2} dx \quad (2.64)$$

For a resistor of resistance R , the measured sensor voltage is given by,

$$U_M = R \frac{dq_p}{dt} = R A e_{31} (h_b + h_s) \sum_0^{\infty} q_n \frac{1}{l_s} \int_0^{l_s} \frac{\partial^2 \Psi_n}{\partial x^2} dx. \quad (2.65)$$

When n sensors observe n modes the vector of sensor voltage yields

$$U_s = \bar{\Psi} q. \quad (2.66)$$

Hence

$$\begin{bmatrix} U_{s1} \\ U_{s2} \\ \vdots \\ U_{sn} \end{bmatrix} = \begin{bmatrix} \bar{\Psi}_{11} & \bar{\Psi}_{12} & \dots & \bar{\Psi}_{1n} \\ \bar{\Psi}_{21} & \bar{\Psi}_{22} & \dots & \bar{\Psi}_{2n} \\ \vdots & \vdots & \dots & \vdots \\ \bar{\Psi}_{n1} & \bar{\Psi}_{n2} & \dots & \bar{\Psi}_{nn} \end{bmatrix} \begin{bmatrix} q_1 \\ q_2 \\ \vdots \\ q_n \end{bmatrix} \quad (2.67)$$

where for the i^{th} sensor and n^{th} mode,

$$\bar{\Psi}_{in} = -\frac{h_s}{\epsilon_{33}} (h_b + h_s) \left(e_{31} \int_{xi_1}^{xi_2} \frac{\partial^2 \Psi_n(x)}{\partial x^2} dx \right) \quad (2.68)$$

here xi_1 and xi_2 represent the coordinates of the ends of sensor i .

2.5 Modal Amplitudes for Excitation by a Point Sinusoidal Excitation - Shaker and Sinusoidal Excitation by the Actuator

From (2.39) it is clear that the only difference in computing the modal amplitudes for a shaker excitation and an actuator excitation lies in the integral term containing the force p_z . Here an excitation applied on a simply supported beam is considered..

Distinguishing the integral for both cases, this could be written down that

$$I_s = \int_0^1 p_{zs} \Psi_n(\xi) d\xi, \quad \text{for the shaker.} \quad (2.69)$$

$$I_{act} = \int_0^1 p_{zact} \Psi_n(\xi) d\xi, \quad \text{for the piezoelectric actuator.} \quad (2.70)$$

In the case of a shaker, the property of the Dirac- delta function can be utilised as the represent the point load excitation, which leads to

$$\begin{aligned} I_s &= \int_0^1 \delta(\xi - \xi_0) \hat{F} \sin(n\pi\xi) d\xi \\ &= \hat{F} \sin(n\pi\xi_0). \end{aligned} \quad (2.71)$$

In the case of the piezoelectric actuator, the force vector could be written using (2.52) in dimensionless form as

$$\hat{p}_{zact} = C_0 \varepsilon_{pe} [\delta'(\xi - \xi_1) - \delta'(\xi - \xi_2)] . \quad (2.72)$$

Where ξ_1 and ξ_2 represent the two edges of the actuator in the natural coordinate system. Hence one can arrive at an expression for the integral I_{act} as

$$\begin{aligned} I_{act} &= \int_0^1 C_0 \varepsilon_{pe} [\delta'(\xi - \xi_1) - \delta'(\xi - \xi_2)] \sin(n\pi\xi) d\xi \\ &= C_0 \varepsilon_{pe} n\pi [\cos(n\pi\xi_2) - \cos(n\pi\xi_1)]. \end{aligned} \quad (2.73)$$

This expression helps to calculate the frequency response function of the actuator excitation. Hence it becomes a very important tool for designing the actuator locations and maximum control spillover reduction. The input control function $p(x)$ could thus be tailored to achieve the required modal excitation in the control field.

Chapter 3

Modal State Space Formulation and Modal Control

The design methods based on the state space approach, often called Modern methods , start from a system description using the first order differential equations governing the state variables. The formalism applies equally to single input single output (SISO) and multi input multi output (MIMO) systems.

In the state variable form, a linear system is described by a set of first order linear differential equations,

$$\dot{x} = Ax + Bu + Ew_1 \quad (3.1)$$

$$y = Cx + Du + w_2 \quad (3.2)$$

with the following notations:

- x state vector,
- u input vector,
- y output vector,
- w_1 system noise,
- w_2 measurement noise,
- A system matrix,
- B input matrix,
- C output matrix,
- D feed through matrix,
- E system noise input matrix.

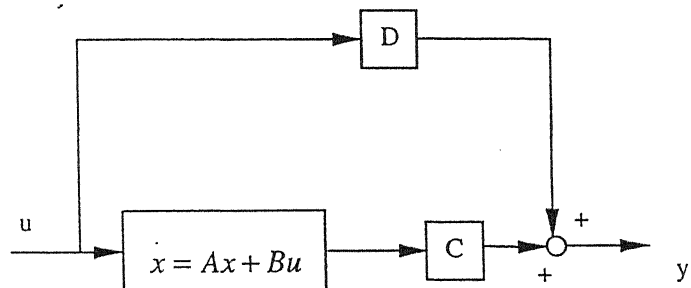


Fig 3.1 : State space form of a linear system

The feed through component D only occurs in special cases where the input quantities, e.g. actuator forces and moments, have a direct influence on the sensor measurement. It could be a result of sensor type - e.g. accelerometer or location - when collocated with the actuator, or as a result of the modal truncation, the so called residual mode. The system noise w_1 may

include environmental loads, modeling errors, non-linearity's and noise in the input vector. The measurement noise w_2 includes the sensor noise and the modeling errors.

3.1 Modal State Space Description for a Beam with External Excitation

By substituting for the displacement as $w(x,t) = \sum q_n(t)\Psi(x)$, the Euler-Bernoulli equation of a thin beam can be written down in the modal coordinate $q_n(t)$ as

$$\ddot{q}_n + 2\zeta_n \omega_n \dot{q}_n + \omega_n^2 q_n = p_{nz} \quad (3.3)$$

where p_{nz} is the modal load and is given by,

$$p_{nz} = \frac{\int_0^l p_z(x,t) \Psi_n(x) dx}{\rho A \int_0^l \Psi_n^2(x) dx}. \quad (3.4)$$

The damping was assumed to be a hysteresis one, by replacing the young's modulus E by a complex formulation $E' + iE''$, with E' as the storage modulus and E'' as the loss modulus.

The loss factor η is defined as

$$\eta = 2\zeta_n = \frac{E''}{E'}. \quad (3.5)$$

The above second order equation implies that there are two state variables. They can be selected as

$$\begin{aligned} x_1 &= q_n, \\ x_2 &= \dot{q}_n \end{aligned} \quad (3.6)$$

With this choice the equation can be written down as a set of two first order equations,

$$\begin{aligned} \dot{x}_1 &= x_2 \\ \dot{x}_2 &= -2\zeta_n \omega_n x_2 - \omega_n^2 x_1 + p_{nz}, \text{ or} \\ \begin{pmatrix} \dot{x}_1 \\ \dot{x}_2 \end{pmatrix} &= \begin{pmatrix} \dot{q}_n \\ \ddot{q}_n \end{pmatrix} = \begin{pmatrix} 0 & 1 \\ -\omega_n^2 & -2\zeta_n \omega_n \end{pmatrix} \begin{pmatrix} q_n \\ \dot{q}_n \end{pmatrix} + \begin{pmatrix} 0 \\ h_n \end{pmatrix} p_z(t) \end{aligned} \quad (3.7)$$

where the input factor h_n can be written down as

$$h_n = \frac{\int_0^l p_z(x) \Psi_n(x) dx}{\rho A \int_0^l \Psi_n^2(x) dx}. \quad (3.8)$$

This can be diagrammatically represented as shown in Fig 3.1.

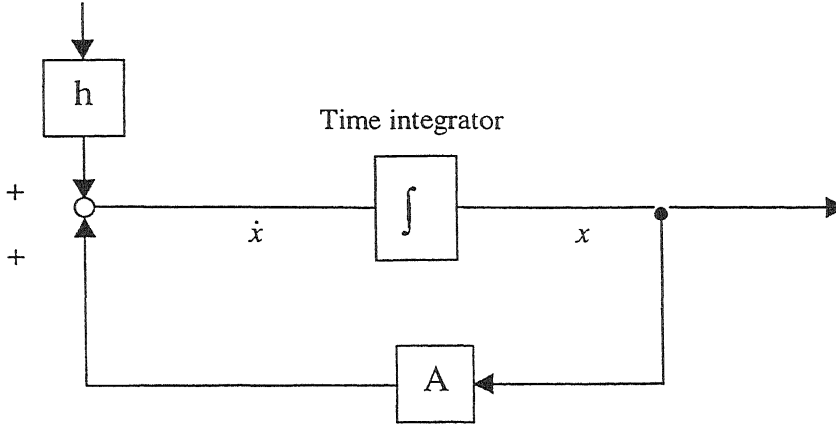


Fig : 3.2 System with external excitation h

where, the vector of input h for mode n can be written down as

$$h = \begin{bmatrix} 0 \\ h_n \end{bmatrix} \quad (3.9)$$

In the shortened form (3.7) could be written down as

$$\dot{x} = Ax + h \hat{p}_z \quad (3.10)$$

3.2 State Space Form with Included Modal Actuator Input

In the same lines as the modal input excitation vector h was described, the actuator input matrix B for a single mode can be written down as

$$B = \begin{bmatrix} 0 \\ b_n \end{bmatrix} \quad (3.11)$$

where the actuator input factor b_n can be expressed as

$$b_n = \frac{\int_l \hat{p}_{zact}(x) \Psi_n(x) dx}{\rho A \int_l \Psi_n^2(x) dx} \quad (3.12).$$

Now including the actuator input into the modal state space form without h , the modified equation is

$$\begin{pmatrix} \dot{x}_1 \\ \dot{x}_2 \end{pmatrix} = \begin{pmatrix} q_n \\ \dot{q}_n \end{pmatrix} = \begin{pmatrix} 0 & 1 \\ -\omega_n^2 & -2\zeta\omega_n \end{pmatrix} \begin{pmatrix} q_n \\ \dot{q}_n \end{pmatrix} + \begin{pmatrix} 0 & \dots & 0 \\ b_{1n} & \dots & b_{mn} \end{pmatrix} \begin{pmatrix} u_1 \\ \vdots \\ \vdots \end{pmatrix} \quad (3.13)$$

where m is the number of actuators and u is the actuator input voltage applied separately to each actuator.

This can be diagrammatically represented as shown below.

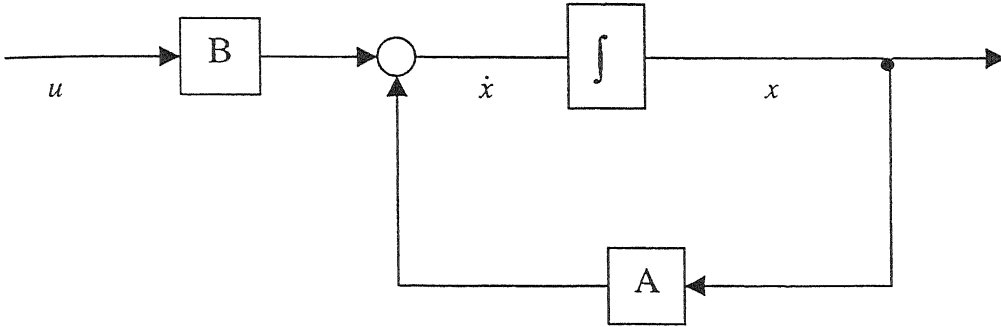


Fig 3.3 : System with actuator input B

3.3 State Space Form with Included Sensor Output

The output vector y , which is the signal generated by the sensors due to the deformation experienced during bending of the beam could now be explained more in detail.

Using (2.65) and replacing the voltage U_s by the state variable y , the following could be obtained

$$\begin{aligned}
 y_w &= C_{amp} \sum_{n=1}^{\infty} \bar{\Psi}_n(x) q_n(t), \\
 y_{\dot{w}} &= C_{amp} \sum_{n=1}^{\infty} \bar{\Psi}_n(x) \dot{q}_n(t).
 \end{aligned} \tag{3.14}$$

If a velocity sensor is used, then the first expression of the above equation can be got by a time integration of the second expression. The constant C_{amp} is the amplification factor of the signal conditioner. The state variable y could thus be represented as shown below

$$\begin{pmatrix} y_w \\ y_{\dot{w}} \end{pmatrix} = C_{amp} \begin{pmatrix} \bar{\Psi}_1 & \dots & \bar{\Psi}_n & 0 & \dots & 0 \\ 0 & \dots & 0 & \bar{\Psi}_1 & \dots & \bar{\Psi}_n \end{pmatrix} \begin{pmatrix} q_1 \\ \vdots \\ q_n \\ \dot{q}_1 \\ \vdots \\ \dot{q}_n \end{pmatrix} \tag{3.15}$$

which can be written down in short form as , $y = Cx$ where C is the sensor output matrix.

The above discussion could be summed up with a block diagram which shows the system along with the sensor output matrix .

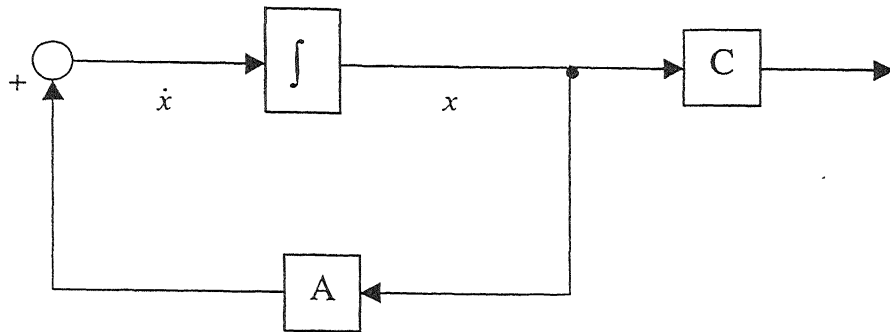


Fig 3.4 : System with the sensor output matrix C

3.4 Active Beam with Sensors and Actuators

Now combining all block diagrams of the excitation, actuator input and the sensor output in to one single equation, the actual state space model of the beam could be formulated. The block diagram in fig 3.4 shows this.

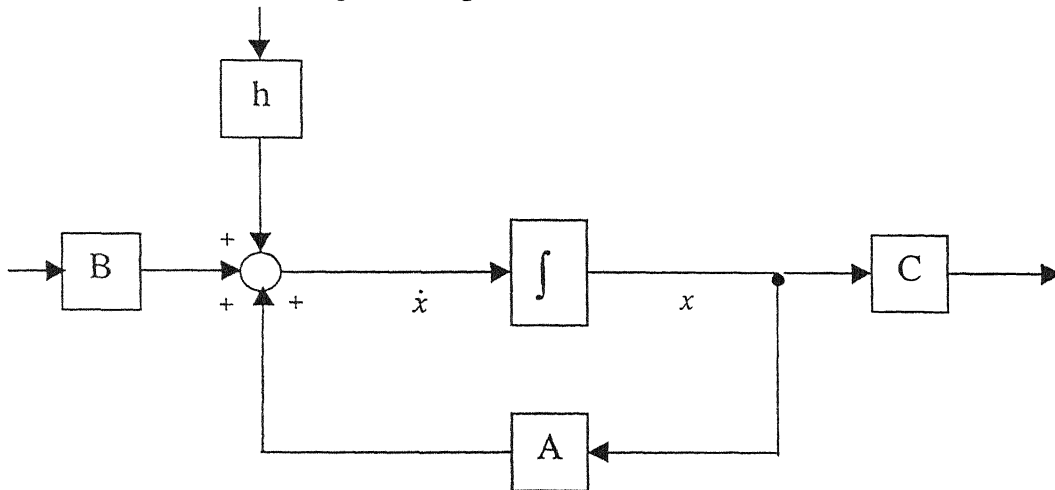


Fig 3.5 : Block diagram of the active beam with the sensors and actuators

Formally the beam equation could thus be written down as

$$\dot{x} = Ax + Bu + hp_z \quad (3.16)$$

$$y = Cx. \quad (3.17)$$

with the matrices A , B , h and C having the values discussed in the earlier sections.

3.5 Modal Control

The signals from the output $y(t)$ weighted by the elements of the gain matrix G could be fed back as the input for the system, where the gain matrix is connected parallel to the system matrix A .

Modal control is a term used to describe a wide variety of control techniques. In general, modal control is an approach to control system design in which the state variable are chosen such that the unforced behavior of each state variable is relatively independent of the behaviour of the other state variables. Here a special modal control technique is used, called the Independent modal space control (IMSC), first coined by Meirovitch [7], in which case a distributed feedback control is possible. This is because the gain factor for the displacement (G_1) and the gain factor for the velocity (G_2) satisfy the eigenvalue problem of the system. It is to be stated here that this control is only possible when the number of actuators (m) is equal to the number of control modes (n_c) or in other words the number of actuators is equal to the number of sensors. In the above stated cases the closed-loop modal equations are independent of each other as G_1 and G_2 are diagonal. If $n_c > m$ then IMSC is not possible as G_1 and G_2 are no more diagonal and hence coupled control has to be resorted to. [Meirovitch]

3.5.1 Independent Modal Space Control (IMSC)

The block diagram of the system and the controller is shown in Fig 3.5. The system is represented by the system matrix A , the actuator input matrix B , and the sensor output matrix C_v . The index v indicates that the sensor signals are proportional to the velocity of the structure in motion. The matrix M is the filter matrix which transforms the desired displacement w into appropriate actuator voltages $\{u_s\}$. Since the object of vibration control is to reduce the vibration amplitudes, the values of the displacement w and the actuator voltages $\{u_s\}$ are set to zero. The output vector $\{y^*\}$ contains the sensor signals of n PVDF point sensors which are located on the surface of the structure. Since the positions, the geometry and the material constants of the sensors are known, the output matrix can be calculated by using (2.64). Assuming that the output matrix C_v is non-singular, the inverse matrix C_v^{-1} exists. The inverse matrix C_v^{-1} becomes the so-called *mode filter/ analyser* as by multiplying it by the output vector $\{y^*\}$, this yields the vector of modal velocities $\{q_v\}$. Therefore a

system of linear equations is created as shown in (3.18). This type of filtering state space quantities by using the output vector is called output feedback.

$$\begin{pmatrix} \dot{q}_1 \\ \dot{q}_2 \\ \vdots \\ \dot{q}_n \end{pmatrix} = \begin{pmatrix} \bar{\Psi}_{11} & \bar{\Psi}_{12} & \dots & \bar{\Psi}_{1n} \\ \bar{\Psi}_{21} & \bar{\Psi}_{22} & \dots & \bar{\Psi}_{2n} \\ \vdots & \vdots & \ddots & \vdots \\ \bar{\Psi}_{n1} & \bar{\Psi}_{n2} & \dots & \bar{\Psi}_{nn} \end{pmatrix}^{-1} \begin{pmatrix} y_1^* \\ y_2^* \\ \vdots \\ y_n^* \end{pmatrix} \quad (3.18)$$

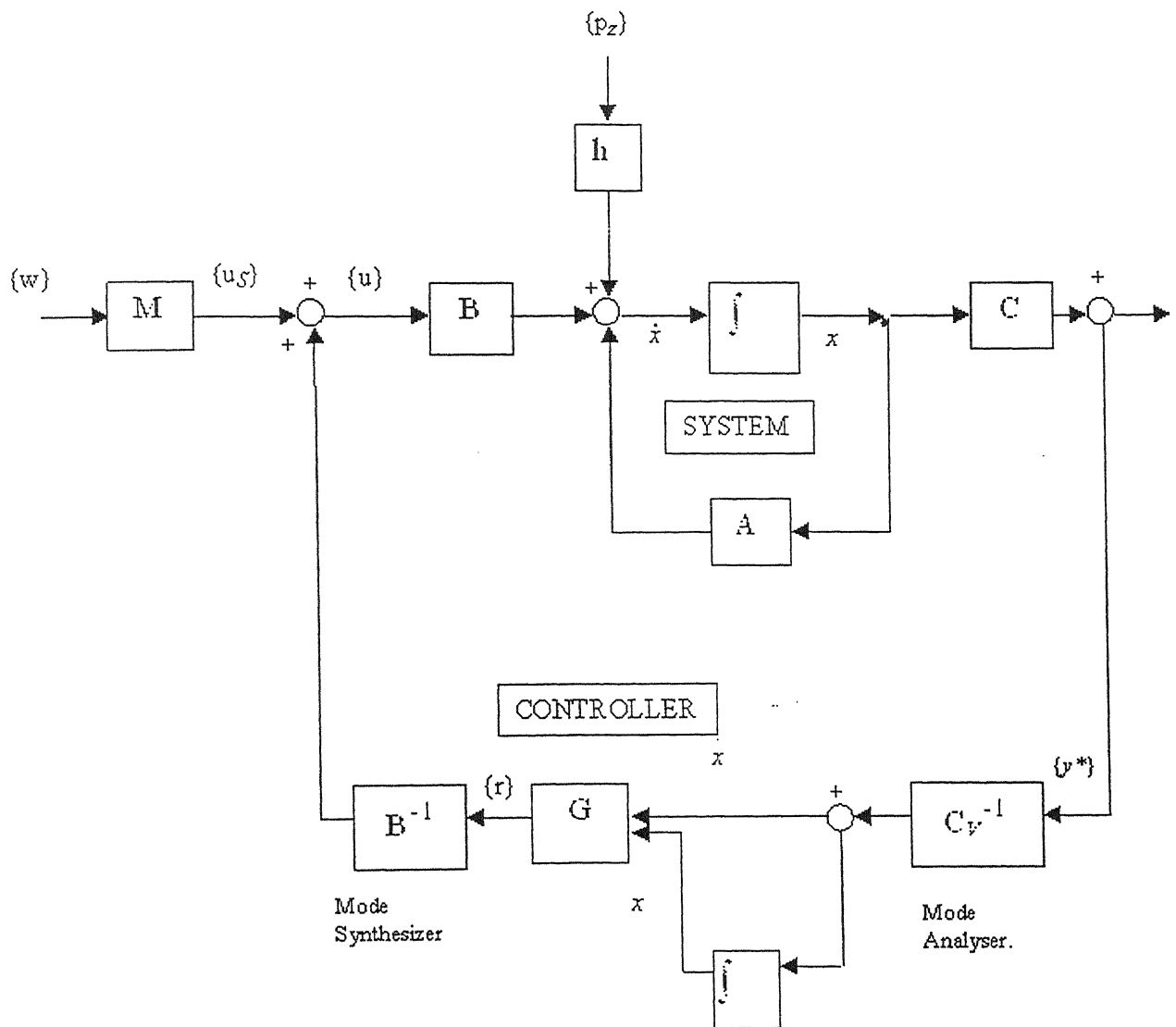


Fig 3.5 : Modal filtered feedback (IMSC) block diagram

$$\{x\} = \begin{pmatrix} 0 \\ \cdot \\ \cdot \\ 0 \\ \dot{q}_1 \\ \cdot \\ \cdot \\ \dot{q}_n \end{pmatrix} + \begin{pmatrix} \int \dot{q}_1 dt \\ \cdot \\ \cdot \\ \int \dot{q}_2 dt \\ 0 \\ \cdot \\ \cdot \\ 0 \end{pmatrix} = \begin{pmatrix} q_1 \\ \cdot \\ \cdot \\ q_n \\ \dot{q}_1 \\ \cdot \\ \cdot \\ \dot{q}_n \end{pmatrix}. \quad (3.1)$$

The multiplication of the gain matrix G and the state space vector x results in the control vector $\{r\}$.

$$\begin{pmatrix} r_1 \\ \vdots \\ r_2 \end{pmatrix} = \begin{pmatrix} g_{q_1} & & & \\ & \ddots & & \\ & & g_{q_1} & \\ & & & \ddots \\ & & & & g_{q_2} & \\ & & & & & \ddots \\ & & & & & & g_{q_2} \end{pmatrix} \begin{pmatrix} q_1 \\ \vdots \\ q_n \\ q_1 \\ \vdots \\ q_n \end{pmatrix} \quad (3.20)$$

Formally (3.20) can be written down in short form as

$$\{r\} = [G_1 \quad G_2] \{x\}. \quad (3.21)$$

The elements of the control vector $\{r\}$ are related to the filtered modes. Therefore, the controller works within the modal state space and a retransformation of the control vector $\{r\}$ into the physical space is required. The retransformation is carried out by the so-called *mode synthesiser* which is defined by the inverse modal actuator matrix B^{-1} . The multiplication of the inverse matrix B^{-1} and the control vector $\{r\}$ leads to the input vector $\{u\}$. The input vector $\{u\}$ has as many elements as actuators are available.

$$\begin{pmatrix} u_1 \\ u_2 \\ \vdots \\ u_m \end{pmatrix} = \begin{pmatrix} b_{11} & b_{12} & \dots & b_{1n_c} \\ b_{21} & b_{22} & \dots & b_{2n_c} \\ \cdot & \dots & \dots & \cdot \\ \cdot & \dots & \dots & \cdot \\ \cdot & \dots & \dots & \cdot \\ b_{m1} & b_{m2} & \dots & b_{mn_c} \end{pmatrix}^{-1} \begin{pmatrix} r_1 \\ r_2 \\ \vdots \\ r_3 \end{pmatrix}. \quad (3.22)$$

The whole of the above discussion can thus be summed up in state-space form as

$$\{u\} = B^{-1} G C_v^{-1} y \quad (3.23)$$

and hence

$$\dot{x} = (A + B[B^{-1} G C_v^{-1} C]) x \quad (3.24)$$

$$y = C x. \quad (3.25)$$

3.6 Determination of Modal Gains– Pole Allocation

One fact that has to be laid down is how to determine the modal gains G_1 and G_2 . Two of the most widely used methods, both of which have been used this study are *pole allocation and optimal control* (Fuller [1], Meriovitch [7]). In this section a brief description of the pole allocation method is outlined.

3.6.1 Pole allocation

In pole allocation, the closed-loop poles are selected in advance and the gains are determined so as to produce these poles. In other words, this technique is based on equating

the characteristic equation of the system matrix for the closed-loop system to some desired polynomial of same order.

The equation for the full state feedback can be written down

$$\dot{x} = (A - BG^T)x + Hp_z. \quad (3.26)$$

The characteristic equation for the closed-loop system can be expressed as

$$|sI - A + BG^T| = 0. \quad (3.27)$$

When the eigenvalues $(s + \lambda_1)(s + \lambda_2) \dots (s + \lambda_n)$ of the desired system can be specified, it is possible to write a corresponding desired characteristic polynomial of the same order as equation (3.27):

$$\Delta_d = (s + \lambda_1)(s + \lambda_2) \dots (s + \lambda_n) = 0. \quad (3.28)$$

Equating (3.27) and (3.28) we can solve for the gain G so that the equality is satisfied.

In the *IMSC*, the procedure is simple. Denoting the closed-loop eigenvalues associated with the n^{th} mode by $-\alpha_n + i\beta_n$, the solution of (3.26) can be written as

$$x_n(t) = c_n e^{(-\alpha_n + i\beta_n)t}. \quad (3.29)$$

Inserting (3.29) into (3.26) and separating the real and imaginary parts yields

$$g_{1n} = \alpha_n^2 + \beta_n^2 - \omega_n^2 \quad \text{and} \quad g_{2n} = 2\alpha_n \quad n=1,2,3,\dots,n_c. \quad (3.30)$$

To guarantee asymptotic stability, however, it is only necessary to impart the open-loop eigenvalues some negative real part and it is not necessary to alter the frequencies. This can be achieved by letting $\beta_n = (\lambda)^{1/2} = \omega_n$, where ω_n is the n^{th} eigen frequency of the open-loop system.

Hence, the frequency-preserving control gains are

$$g_{1n} = \alpha_n^2 \quad \text{and} \quad g_{2n} = 2\alpha_n \quad \text{with} \quad n=1,2,3,\dots,n_c. \quad (3.31)$$

The fig (3.7) below sketches the Pole Placement method for a single degree of freedom oscillator. Here it is clearly shown how the real part is shifted more to the left of the complex plane.

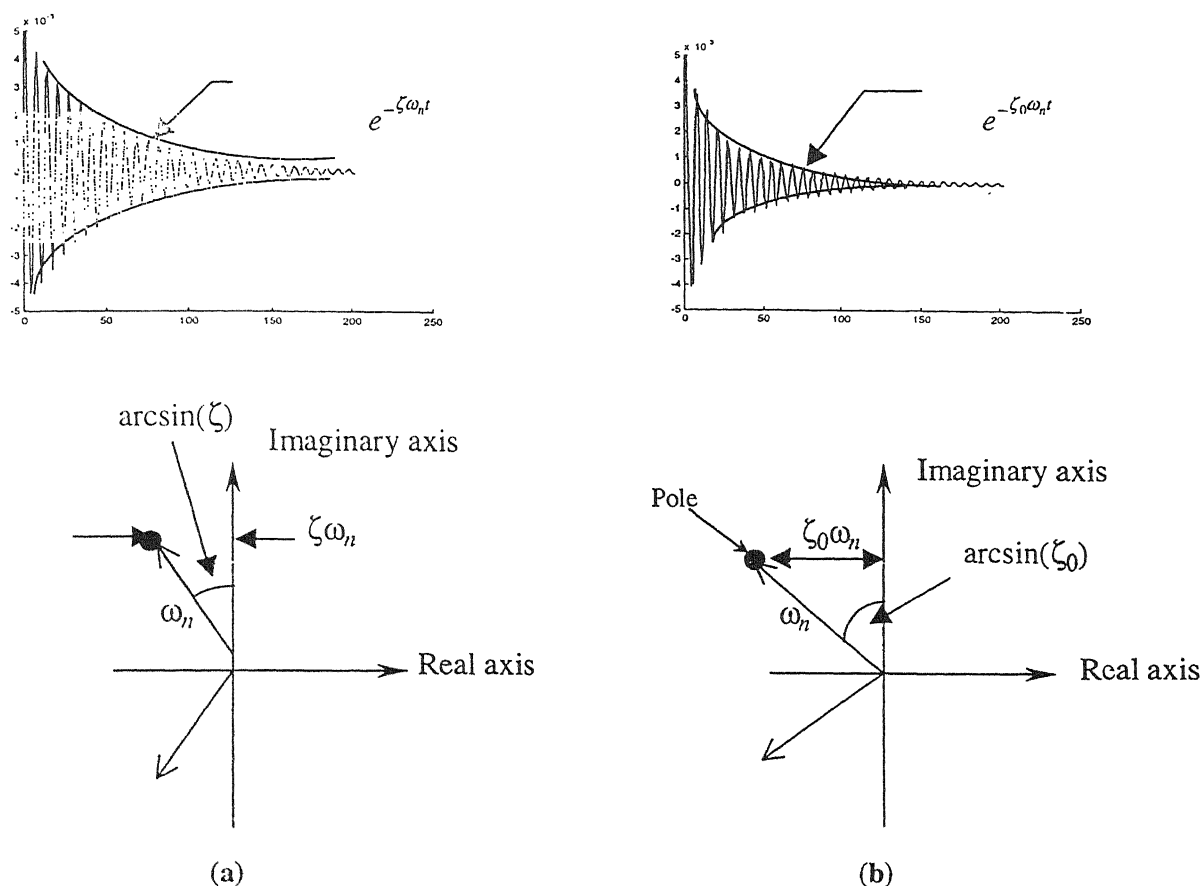


Fig. 3.7 Single degree of freedom oscillator: (a) Open-loop and (b) Closed-loop poles

Though the fact that poles of the closed-loop system can be located arbitrarily in the complex plane is remarkable, this can always be done provided the system is controllable. Although, it is important to state that even if the above stated condition is satisfied, pole placement may not be feasible because the control effort involved would be too large, or because the large values of the feedback gains would render the system oversensitive to noise or modeling errors.

3.7 Stability

As stated in the earlier section, the stability of a linear feedback system can be most readily be determined by inspection of the position of its closed loop poles. The equilibrium state $x = 0$ is stable in the sense of *Liapunov* if, for every $\epsilon > 0$ there is some $\delta < \epsilon$ such that, if

$\|x_0\| < \delta$, then $\|x\| < \varepsilon$ for all $t < t_0$. In this statement $\|\cdot\|$ stands for a norm, measuring the distance to the equilibrium. States which are not stable in the sense of Liapunov are unstable. A linear system is stable if the real parts of all its poles (eigenvalues of $[A]$) are negative i.e. $\text{Re}(\lambda_i) < 0$, or in other words, if all poles of A are to the left of the imaginary axis when plotted in the complex s plane. It is worth noting that any system with a pole lying exactly on the imaginary s axis, i.e. having zero real part, is not stable as according to the definition stated in the above sentences. Meirovitch [7] has described such systems as also to be stable, and describing the systems satisfying the definition of stability as stated above to be asymptotically stable.

It is often the case in practice, however, that the closed polynomial forms of the transfer functions are generally not directly available, and stability must be assessed from input-output measurements made on the systems before control. The Nyquist stability criterion provides such a method, using the open loop frequency response. The Nyquist criterion states, that a closed loop system is stable only if the polar plot of the open loop frequency response does not enclose the point $(-1,0)$ in the s plane.

Chapter 4

Actuator and Sensor Placements

An important question to ask in designing a closed loop system is where to place the sensors and actuators on the structure. It is also important to decide the shape of them. Control theory provides an answer to these questions by introducing the concepts of controllability and observability. A structure is controllable if the installed actuators excite all its structural modes. It is observable if the installed sensors detect the motions of all the modes. Classically, according to control theory the system is if the *controllability matrix* - in this case input matrix B - is of full rank and it is observable if the *observability matrix* - in this case output matrix C - is of full rank. This approach is often not enough for practical engineering problems where a more quantitative information is needed. In this study the quantitative approach is used in terms of the controllability and observability grammarians - in terms of H_2 and H_∞ norms - which represent a degree of controllability and observability of each mode. Thus the approach used consists of the determination of the norm of each sensor / actuator for selected modes which is the normalized input B and output C matrix, and then grade them according to their participation in the system norm. This is a computational effective approach with clear physical interpretation.

The problem can thus be summarized in the following way: Given a large set of sensors and actuators, the placement problem consists of determining the location of a smaller subset of sensors or actuators such that the H_2 or H_∞ norms of the subset is as close as possible to the norm of the original set.

4.1 Norms

System norms serve as a measure of the system size and in this capacity they are used in the actuator / sensor placement procedures. For flexible structures the H_2 norm has an additive property. It is a root-mean-square (rms.) sum of the norms of the individual modes. The H_∞ norm can also be determined from the corresponding modal norms, by choosing the largest one. In addition both of these norms of a structure with multiple inputs (or outputs) can be decomposed into the rms. sum of norms of a structure with a single input (or output). These properties allow for the development of unique and efficient actuator / sensor placements.

4.1.1 The H_2 Norm

If A , B and C be the system state-space representation of a linear system, and if $G(\omega)=[C](j\omega[I]-[A])^{-1}[B]$ be its transfer function and I is the unity matrix, the H_2 norm of the system is defined as (Gawronski [4])

$$\| [G(\omega)] \|_2^2 = \frac{1}{2\pi} \int_{-\infty}^{\infty} \text{tr}([G^*(\omega)][G(\omega)]) d\omega, \quad (4.1)$$

where $*$ stands for the complex-conjugate-transpose of a matrix and tr stands for the trace of the matrix.

Mode Norm

If $G_n(\omega)=[C_n](j\omega[I]-[A_n])^{-1}[B_n]$ is the transfer function of the n^{th} mode, the H_2 norm of the n^{th} mode can be derived as (Gawronski [4])

$$\| [G_n] \|_2^2 = \frac{\| [B_n] \|_2 \| [C_n] \|_2}{2\sqrt{\zeta_n}\omega_n}, \quad (4.2)$$

where B_n and C_n are the input and output matrices of the n^{th} mode for S inputs (actuators) and R outputs (sensors).

$$B_n = [B_{n1} \ B_{n2} \ \dots \ B_{nS}] \quad , \quad C_n = \begin{bmatrix} C_{1n} \\ C_{2n} \\ \vdots \\ C_{Rn} \end{bmatrix}$$

In (4.2) ζ_n stands for the damping ratio and ω_n stands for the eigen frequency of the n^{th} mode.

System Norm

If $G(\omega)=[C](j\omega[I]-[A])^{-1}[B]$ is the transfer function of a structure then the system H_2 norm is approximately the rms sum of the modal norms i.e.

$$\| [G] \|_2 = \sqrt{\sum_{n=1}^{n_c} \| [G_n] \|_2^2} \quad (4.3)$$

where n_c is the number of control modes.

4.1.2 H_∞ Norm

The H_∞ norm of a stable system is defined as (Gawronski [4])

$$\| [G(\omega)] \|_\infty = \max_{\omega} \sigma_{\max}([G(\omega)]), \quad (4.4)$$

where $\sigma_{\max}([G(\omega)])$ is the largest singular value of $G(\omega)$. The H_∞ norm of a SISO system is the peak of the transfer function magnitude, see also fig. 4.1.

Mode Norm

The H_∞ Norm of the n^{th} mode is estimated as

$$\| [G_n] \|_\infty \cong \frac{\| [B_n] \|_2 \| [C_n] \|_2}{2\zeta_n \omega_n}, \quad (4.5)$$

where ζ_n and ω_n stands for the modal damping and the eigenfrequency of the n^{th} mode, respectively.

System Norm.

Due to the almost independence of the modes, the system H_∞ norm is the largest of the mode norms i.e.

$$\| [G] \|_\infty \cong \max_n \| [G_n] \|_\infty. \quad (4.6)$$

This property says that the largest modal peak response of a lightly damped structure determines the worst-case response.

From the above definitions, $\| [G] \|_2$ can be interpreted as the area enclosed by the transfer function and $\| [G] \|_\infty$ is the value of the largest peak of the transfer function. This is shown in the fig. 4.1 for a system with three controlled modes, e.g. $n_c = 3$.

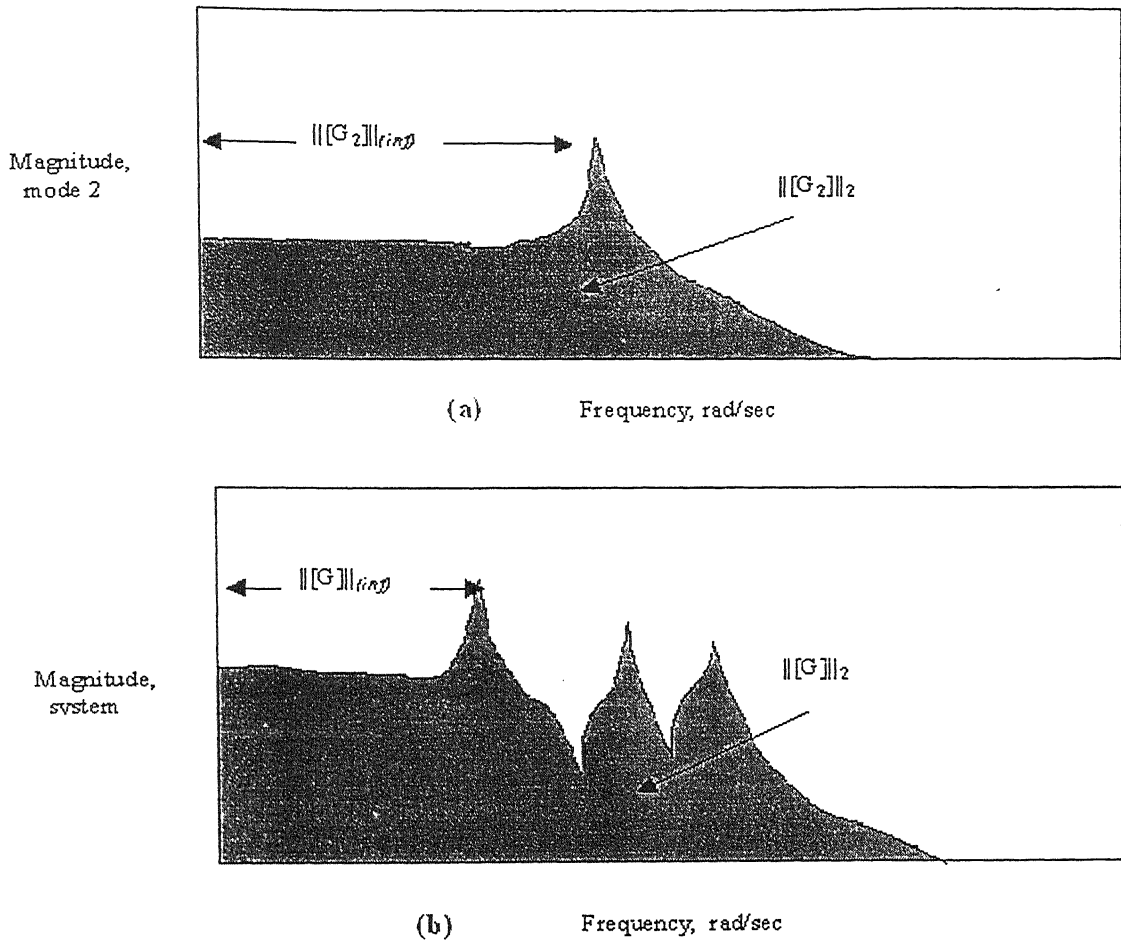


Fig. 4.1 : H_2 and $H(\infty)$ norms (a) of the second mode, and (b) of the system. There is one more important property of these norms which make them so vital for the use in placing actuators and sensors. This is the additive property of a set of actuators/sensors for each mode.

4.1.3 Additive Property for a Set of Actuators / Sensors for each Mode

The two norms of the n^{th} mode of a structure with a set of S actuators is the rms sum of the norms of the mode with each single actuator from this set

$$\|G_n\|_2 \cong \sqrt{\sum_{j=1}^S \|G_{nj}\|_2^2} \quad n=1,2,\dots,\eta \quad , \quad (4.7)$$

$$\text{where } \|G_{nj}\|_2 = \frac{\|B_{nj}\|_2 \|C_n\|_2}{2\sqrt{\zeta_n \omega_n}} .$$

Similarly the two norm of the n^{th} mode of a structure with a set of R sensors is the rms sum of norms of the mode with each single actuator from this set

$$\|G_n\|_2 \equiv \sqrt{\sum_{k=1}^R \|G_{nk}\|_2^2} \quad n=1,2,\dots,\eta \quad , \quad (4.8)$$

$$\text{where } \|G_{nk}\|_2 = \frac{\|B_n\|_2 \|C_{kn}\|_2}{2\sqrt{\zeta_n \omega_n}}$$

4.2 Actuator Placement

The actuators in our case are distributed piezoelectric sheets which are bonded to the surface of the structure. The efficiency of the actuators can be expressed in scalar performance indices.

4.2.1 Actuator Placement Indices Matrix

The placement index indicates the controllability of the j th actuator with respect to the n th mode and is defined as :

$$\sigma_{2jn} = \frac{\|G_{jn}\|_2}{\|G\|_2} \quad (\text{where } j=1,\dots,S) \text{ by using the } H_2 \text{ norm} \quad (4.9)$$

and

$$\sigma_{\infty jn} = \frac{\|G_{jn}\|_{\infty}}{\|G\|_{\infty}} \quad \text{by using the } H_{\infty} \text{ norm} \quad (4.10)$$

The placement indices are then arranged into the placement indices matrices $[\Sigma]_2$ and $[\Sigma]_{\infty}$

$$[\Sigma]_2 = \begin{bmatrix} \sigma_{211} & \dots & \dots & \dots & \sigma_{21S} \\ \dots & \dots & & & \dots \\ \dots & & \dots & & \dots \\ \sigma_{2n1} & \dots & \dots & \dots & \sigma_{2nS} \end{bmatrix} \quad \text{and} \quad [\Sigma]_{\infty} = \begin{bmatrix} \sigma_{\infty 11} & \dots & \dots & \dots & \sigma_{\infty 1S} \\ \dots & \dots & & & \dots \\ \dots & & \dots & & \dots \\ \sigma_{\infty n1} & \dots & \dots & \dots & \sigma_{\infty nS} \end{bmatrix} \quad (4.11)$$

Each row of these matrices is related to a mode and each column corresponds to an actuator. Since the output matrix is included in the calculation of the modal norms the actuator placement indices are dependent on the sensors. Therefore the actuator performance is estimated with respect to the sensor performance. If the performance of the actuator is required without including the sensors, then the input matrix has to be replaced by the unity matrix. The unity matrix does not influence the actuator norm calculated by equation (4.7) and emulates the ideal sensor array which enables the observation of all modes.

4.2.2 Control Performance Indices

The actuator placement indices are evaluated for each actuator and each mode. In order to determine the performance of all actuators together a control performance index is introduced. The calculation of the performance index starts with the summation of all S actuator placement indices of the n^{th} mode in the way of root-mean square values for $\sigma_{a_{2n}}$ or by choosing the largest actuator placement index related to the n^{th} mode for $\sigma_{a_{\infty k}}$.

$$\sigma_{a_{2n}} = \sqrt{\sum_{j=1}^S \sigma_{2ni}^2} \quad (4.12)$$

$$\sigma_{a_{\infty n}} = \max_n (\sigma_{\infty nj}) \quad (4.13)$$

These values indicate the control performance of a selected number of actuators with respect to a selected mode and they are collected into the modal control performance vector as

$$\left[\sum \right]_{a_2}^T = [\sigma_{a_{21}} \quad \dots \quad \sigma_{a_{2n_c}}]^T \quad \text{and} \quad (4.14)$$

$$\left[\sum \right]_{a_{\infty}}^T = [\sigma_{a_{\infty 1}} \quad \dots \quad \sigma_{a_{\infty n_c}}]^T \quad (4.15)$$

To obtain the numerical expression for the control performance for all modes the values $\sigma_{a_{2n}}$ or $\sigma_{a_{\infty n}}$ are summarized by

$$\alpha_{a_2} = \frac{1}{n_c} \sum_{n=1}^{n_c} \sigma_{a_{2n}} \quad (4.16) \quad \beta_{a_2} = \sqrt[n_c]{\prod_{n=1}^{n_c} \sigma_{a_{2n}}} \quad (4.17)$$

$$\alpha_{a_{\infty}} = \frac{1}{n_c} \sum_{n=1}^{n_c} \sigma_{a_{\infty n}} \quad (4.18) \quad \beta_{a_{\infty}} = \sqrt[n_c]{\prod_{n=1}^{n_c} \sigma_{a_{\infty n}}} \quad (4.19)$$

α_{a_2} and $\alpha_{a_{\infty}}$ are the so - called arithmetic mean (am) control performance indices of an actuator array and β_{a_2} and $\beta_{a_{\infty}}$ are the geometric mean (gm) control performance indices.

4.2.3 Design procedure

The design procedure its done by the following steps:

1. The modes to be controlled are selected.
2. The actuator array is created according to the shape of the lowest mode.
3. The control performance indices β_{a_2} and $\beta_{a_{\infty}}$ are calculated.
4. If β_{a_2} and $\beta_{a_{\infty}}$ are equal to zero, then an actuator array is created according to the shape of the next higher mode.

5. The control performance indices α_{a2} and $\alpha_{a\infty}$ are then calculated.
6. If the α_{a2} and $\alpha_{a\infty}$ values were lower than a certain limit -got from practical experience, then an actuator array according to the shape of the next higher mode is created and the procedure was repeated from step 3.
7. The design was stopped if the α_{a2} and $\alpha_{a\infty}$ values are higher that the above specified limit.

The above mentioned limit for the control performance indices α_{a2} and $\alpha_{a\infty}$ has to be chosen from practical experience. As a rule of thumb values above 0.2 were considered to be acceptable.

4.3 Sensors Placement

The optimal sensor placement depends in twofold respect on the output matrix C. On one hand the magnitudes of the single elements indicate the sensitivity of a single sensors, and on the other hand the condition of C indicates their correlation.

4.3.1 Sensitivity of Single Sensor

The first objective is to obtain preferably high elements of C. This can be performed by the vivid placement of the sensors on the antinodes of the controlled modes as these are the points of maximum curvature. However, this approach is limited to simple structures and a small number of modes. In more complicated cases a sensitivity performance index for each sensor arrangement has to be calculated. Hence, this is carried out in the same lines as the control performance indices derived in (4.9) to (4.19). The only difference being that the placement indices now indicates the controllability of the sensor with respect to the n^{th} mode. The B_n has now to be inserted as a unity matrix, since it is assumed that the actuators are placed ideally. The sensitivity indices α_{s2} , $\alpha_{s\infty}$, β_{s2} and $\beta_{s\infty}$ for the sensors are determined like their respective actuator performance indices.

4.3.2 Condition of The Output Matrix

The solid computational solubility of the equation system determined by C depends primarily on its condition. As the same kind of sensors and measurement conditions is used for each sensor to obtain the velocity, the C matrix becomes C_v matrix which is quadratic. The mathematical most precise way to solve a system of linear equations is given when its matrix is orthogonal. In case of linearly dependent rows of the matrix considered, the solution gets singular. If C_v is near to singularity, the calculation of the desired modes will be

5. The control performance indices α_{a_2} and α_{a_∞} are then calculated.
6. If the α_{a_2} and α_{a_∞} values were lower than a certain limit -got from practical experience, then an actuator array according to the shape of the next higher mode is created and the procedure was repeated from step 3.
7. The design was stopped if the α_{a_2} and α_{a_∞} values are higher than the above specified limit.

The above mentioned limit for the control performance indices α_{a_2} and α_{a_∞} has to be chosen from practical experience. As a rule of thumb values above 0.2 were considered to be acceptable.

4.3 Sensors Placement

The optimal sensor placement depends in twofold respect on the output matrix C. On one hand the magnitudes of the single elements indicate the sensitivity of a single sensors, and on the other hand the condition of C indicates their correlation.

4.3.1 Sensitivity of Single Sensor

The first objective is to obtain preferably high elements of C. This can be performed by the vivid placement of the sensors on the antinodes of the controlled modes as these are the points of maximum curvature. However, this approach is limited to simple structures and a small number of modes. In more complicated cases a sensitivity performance index for each sensor arrangement has to be calculated. Hence, this is carried out in the same lines as the control performance indices derived in (4.9) to (4.19). The only difference being that the placement indices now indicates the controllability of the sensor with respect to the n^{th} mode. The B_n has now to be inserted as a unity matrix, since it is assumed that the actuators are placed ideally. The sensitivity indices α_{s_2} , α_{s_∞} , β_{s_2} and β_{s_∞} for the sensors are determined like their respective actuator performance indices.

4.3.2 Condition of The Output Matrix

The solid computational solubility of the equation system determined by C depends primarily on its condition. As the same kind of sensors and measurement conditions is used for each sensor to obtain the velocity, the C matrix becomes C_v matrix which is quadratic. The mathematical most precise way to solve a system of linear equations is given when its matrix is orthogonal. In case of linearly dependent rows of the matrix considered, the solution gets singular. If C_v is near to singularity, the calculation of the desired modes will be

impossible because this will lead to mathematically unprecise results. Therefore a scalar quantity to classify the status of C_v between orthogonality and singularity is needed. This scalar quantity can be found by computing the condition number of the matrix considered.

The condition number is calculated as

$$cond([C_v]) = \frac{w_{\max}([C_v])}{w_{\min}([C_v])}, \quad (4.20)$$

where w_{\max} , w_{\min} indicates the highest and lowest singular value of the matrix C_v , respectively.

The singular values are computed using a Singular Value Decomposition (Numerical Recipes [20]) An orthogonal matrix has a condition number of one, a singular matrix has a condition number of infinity and a arbitrary matrix a real number in between.

A measurability index can thus be formulated which includes the condition number and one of the developed sensitivity indices α or β . The measurability index of the sensor array i_s is

$$i_s = \frac{mag_s}{cond([C])} \quad (4.21)$$

where mag_s is the magnitude index α or β . The index ranges between one for the best possible configuration and zero for a defective one.

4.3.3 Design procedure

The design is done by the following steps:

1. The mode shapes of the structure is to be found out.
2. The modes to be controlled (n_c) are then identified. The number of these modes equals the number of sensors.
3. The sensors are placed near the bending antinodes of the mode shapes.
4. The output matrix C_v and the the measurability index i_s are then calculated.
5. If the index i_s is low, then the condition number and the magnitude index has to be checked.
6. If one of the β indices is too low then it means one of the sensors is placed awkward. The line of the output matrix with the lowest values indicates which sensor is then changed.
7. If the condition number is too high, then the column with the lowest values has to be found and one of the sensors must be moved to one of the antinodes of this referring mode. If it is to possible to identify one particular line or row which contains only low values then one of the sensor is moved arbitrary.

8. A new placement combination is then used and the steps from 4 of this procedure is repeated until the measurability index fits the requirements.

Chapter 5

Active Vibration Control of a Beam - Simulation and Experimental Results

This chapter introduces the simulation and experimental results for the IMSC applied to a vibrating simply-supported beam. The optimum actuator and sensor placements are found out for controlling the modal amplitudes of the first four modes. The control problem is simulated for different vibration cases and the effects of spillover are inspected. The experimental work is carried out and the results are discussed.

5.2 Material Properties

The material and geometric properties of the steel beam specimen is listed in the table below.

Property	Parameter	Value	Unit
Length	l	1.126	m
Breadth	b	0.04	m
Height	h	0.005	m
E-Modulus	E	$2.1E11$	Nm^{-2}
Density	ρ	7890	kgm^{-3}

Table 5.1: Properties of the beam

To control the vibration of a beam, PZT materials are used as actuators and PVDF materials are used as sensors. The electrical and mechanical properties of these materials are listed in Table 5.2.

Property	Parameter	PVDF	PZT	Unit
Thickness.	t	110E-6	0.9	m
Piezo strain Constant	d_{31}	23E-12	-210	mv^{-1}
Electromechanical coupling factor	k_{31}	12	34	%
Youngs-Modulus	E	3E9	6.66E10	Nm^{-2}
Relative permittivity	ϵ/ϵ_0	12.5	2400	-

Table 5.2 : Properties of PVDF and PZT materials used in the experiment

5.4 Modal Parameters

An experimental modal analysis is carried out in order to determine the modal parameters namely eigen frequencies (ω), mode shapes(ψ) and the modal damping ratios(ζ) of the structure under consideration. The values determined from the Experimental Modal Analysis (EMA) closely resemble the computed values calculated from the analytical closed form solution. The table below gives the modal information of the first four modes desired to be controlled.

Mode No:	Eigen frequency [Hz]	Damping ratio [%]	Eigen frequency (analytical) [Hz]
1.	10.27	11.43	9.2256
2.	37.65	3.86	36.902
3.	83.49	1.4	83.0304
4.	149.49	1.18	147.609

Table 5.3 : Modal parameters of the beam specimen

5.3 Actuator Placements

The PZT actuators are placed based on the actuator placement indices and control performance indices. If the values of α_{a_2} and α_{a_∞} are higher than a satisfactory limit, in this study the limits are set to $\alpha_{a_2} > 0.4$ and $\alpha_{a_\infty} > 0.2$, the positions of the actuators are accepted. Further, the frequency response functions (FRF) of the beam, excited by a shaker, are compared with the FRFs obtained by exciting the beam with the actuators. Thus this is a good method to check the actuator positions selected by using a good control performance index. Table 5.5 shows the values of various control performance indices for the selected actuator position, which are shown in fig 5.1.

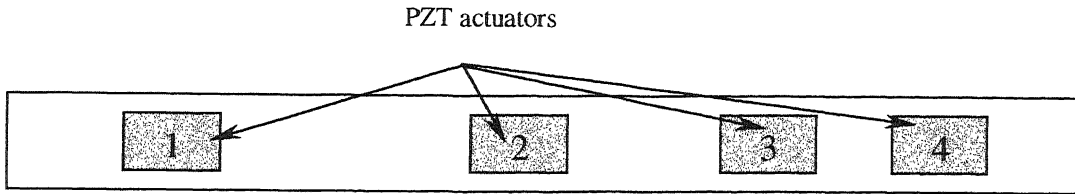


Fig 5.1: Placement of Actuators on the beam

The table below gives the coordinates of the actuators placed on the beam.

Actuator Nr.	x_1 Coordinate [m]	x_2 Coordinate [m]
1	0.133	0.203
2	0.529	0.599
3	0.819	0.889
4	0.903	0.973

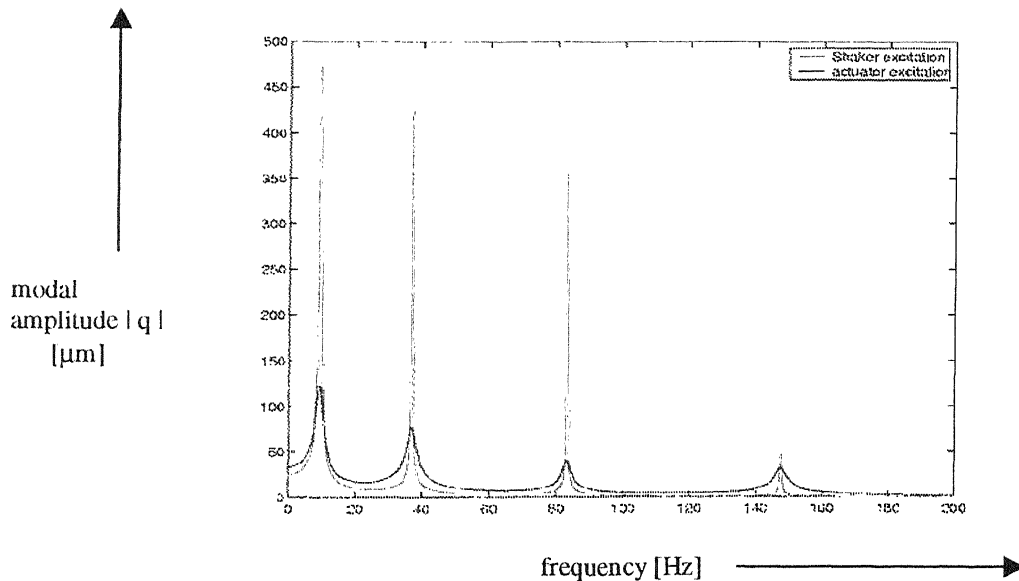
Table 5.4 : Coordinates of the actuators

The control performance indices for this actuator location was obtained as:

α_{a2}	0.41600
$\alpha_{a\infty}$	0.26559
β_{a2}	0.28440
$\beta_{a\infty}$	0.18575

Table 5.5 : Control performance indices for actuator locations

The figure below gives the comparison of the Shaker excited and actuator excited FRF for sinusoidal excitation. The program to calculate the FRF is based on (2.39).



5.4 Sensor Placements

The placement of PVDF sensors are based on both the calculation of the sensitivity indices and the condition of the output matrix [Chapter 4]. The initial sensor locations for iteration were selected to be the points of antinodes of the control modes. The positions were changed to get the best condition and hence the best measurability index . The table below gives the values for the sensitivity indices, condition and the measurability index for the selected sensor location shown in fig 5.3.

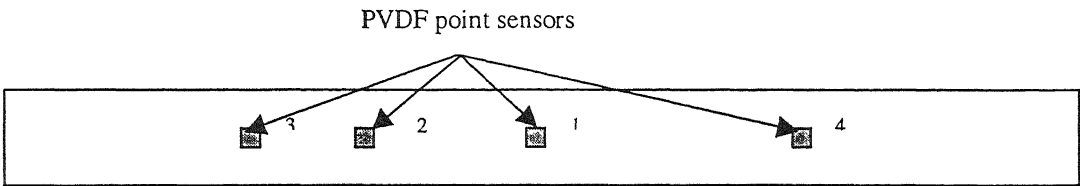


Fig 5.3 : Sensor placement on the beam

The table 5.6 below gives the coordinates of the sensor positions on the beam.

Sensor Nr.	x_1 – Coordinate [m]	x_2 – Coordinate [m]
1	0.5625	0.5775
2	0.3525	0.3675
3	0.2525	0.2675
4	0.8325	0.8475

Table 5.6 : Coordinates of the sensors on the beam

The performance indices and the condition number for the selected sensor placements is outlined in table 5.7 below.

α_{a2}	0.4369
$\alpha_{a\infty}$	0.32808
β_{a2}	0.3419
$\beta_{a\infty}$	0.2383
<i>Cond [C]</i>	8.7085
i_s	0.0501

Table 5.7 : Performance indices of the selected sensor placements on the beam

Photographs of the beam specimen with actuators and sensors bonded to it is shown in Appendix 5.

5.5 Simulation

A program was written down in Matlab in order the simulate the modal filtered feedback control of a simply-supported beam for both the transient and the steady state excitation. The time-modal displacement plots of the beam with and without control and the effects of spillover are simulated. The Runge-Kutta fourth order integration, which is outlined in Appendix 2, is used for time integration.

5.5.1 Transient vibration

The free vibration of the beam with and without control, after displacing the beam in the middle by 5 mm is studied. The figures below gives the time-modal displacements plot of the first and fourth modes with and without control. For control, the time lag for application of control is also taken into consideration into simulation.

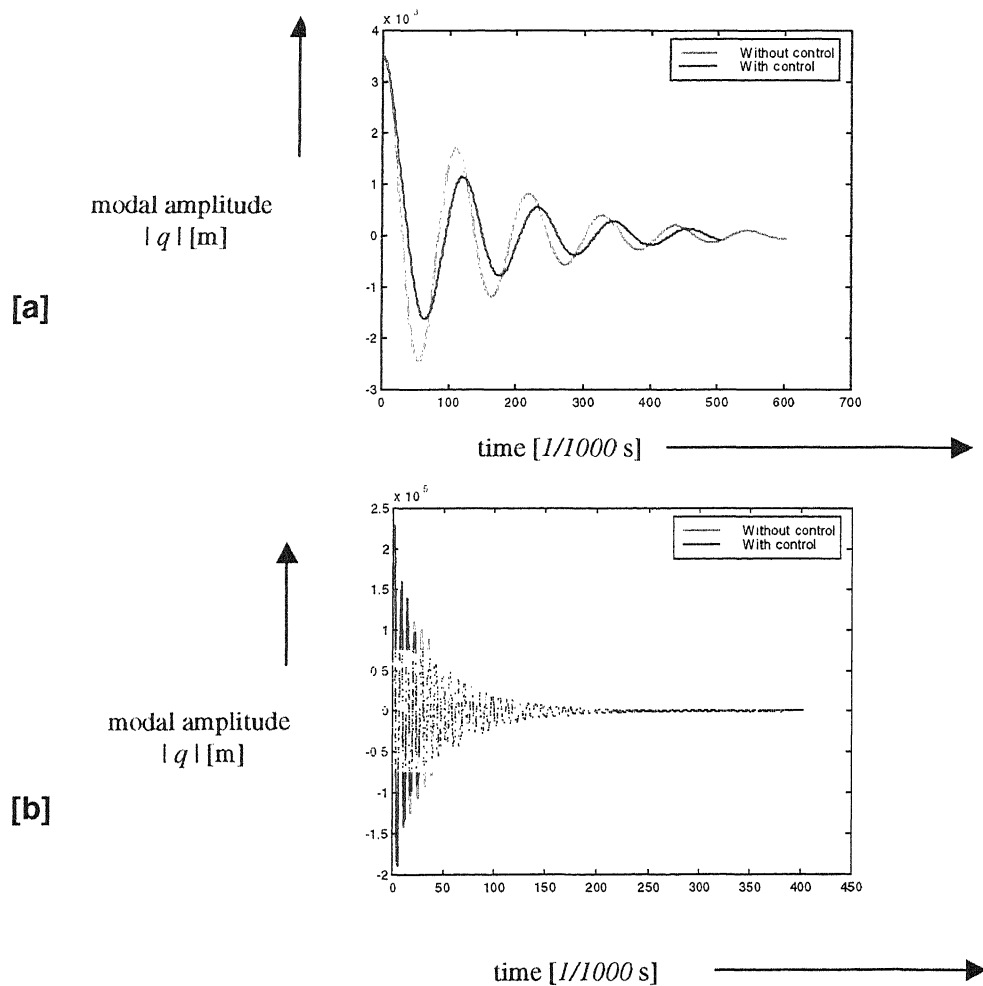


Fig 5.4 : Simulated Modal displacement vs time plot of [a] first and [b] fourth mode

The largest contribution to the response $w(x,t)$ of the beam comes from the lowest mode. Control spillover does exist. By including the effects of fifth, sixth and seventh modes into the previous algorithm, the spillover effect is able to be observed although it is very small. The figure below gives the time-modal displacement plot of the seventh mode when the vibration of the structure is controlled by focusing control of the first four eigen modes. The increase in modal displacement q is a clear indication, that this particular mode is excited at $t=20$ ms as a result of the controller.

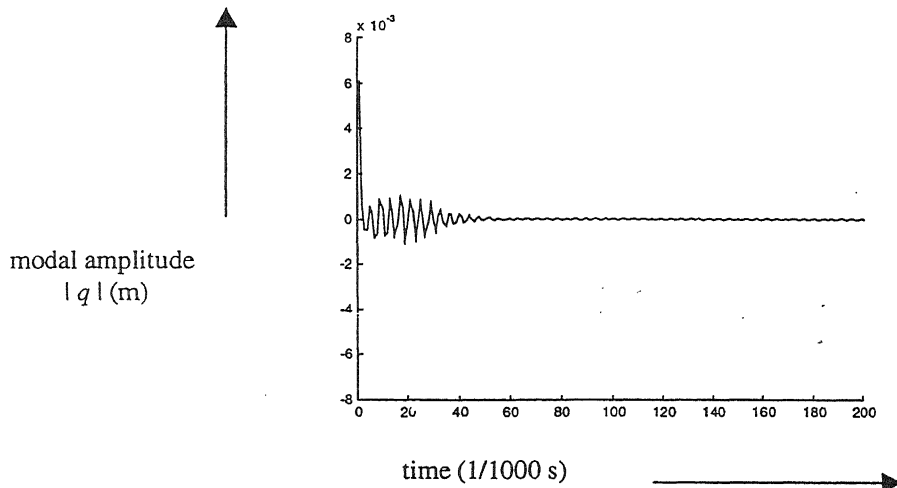


Fig 5.5 : Spill-over effect on the seventh mode

5.5.2 Steady State Vibration

The vibration of a simply-supported beam by exciting it by a harmonic excitation of magnitude $1N$ is studied. The figure below gives the modal displacement vs time plot of the fourth mode when the structure is excited at the fourth eigen frequency. The excitation is removed after the vibration reaches steady state condition and the die down of vibration is simulated with and without control.

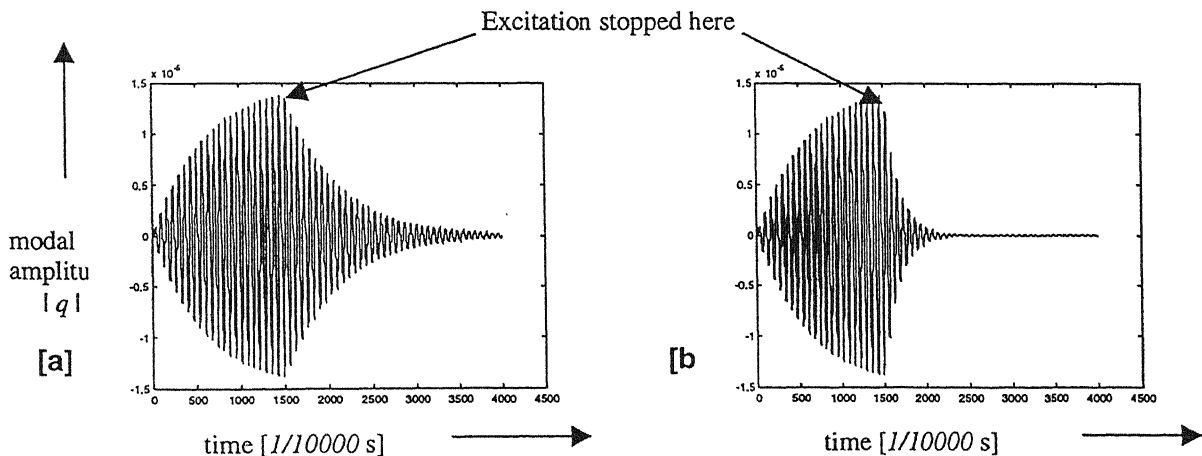


Fig 5.6 : Simulated modal displacement vs time plot for fourth mode [a] without and [b]

5.6 Bonding Procedure

The bonding of the PZT and PVDF layers on the beam is one of the most important detail which has a large impact on the performance of the piezoelectric as an active damping material. In this section a brief note on the bonding of actuators and sensors have been touched upon.

5.6.1 PZT Actuators

The PZT materials are obtained in a standard rectangular size 75x25 mm. After marking the positions of their placement, they are bonded to the structure taking an epoxy glue. This glue has a good resistance to shear forces and provides good metal – PZT bonding. The beam PZT contact is established by means of silver ink glue which provides a good electrical contact so as to ground the structure. The anti-symmetric wafer configuration, see chapter 2, is used for the experiments. The poling directions are adjusted as shown in fig 5.5. Here a voltage is applied to one electrode of the PVDF-actuator, where the other electrode is grounded.

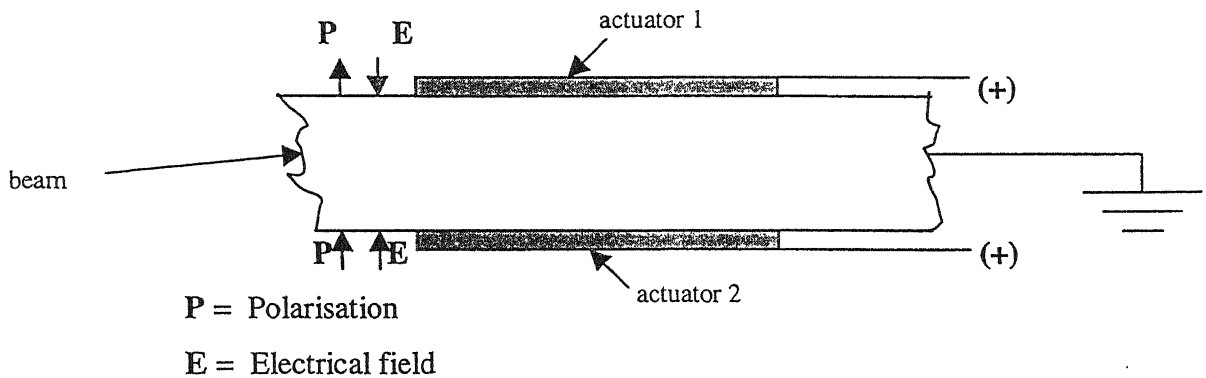


Fig 5.6 : Bonding of PZT actuators

5.6.2 PVDF Sensors

PVDF point sensors of size 1.5 x 1.5 cm are bonded to the structure as shown in the figure below. The sensors are covered by an aluminum foil and are connected with shielded cables to the signal amplifier in order to shield the signal from interfering with the surrounding electro-magnetic field. The outputs of the sensor are then connected to the amplifier which then combines both the output signals and amplifies them.

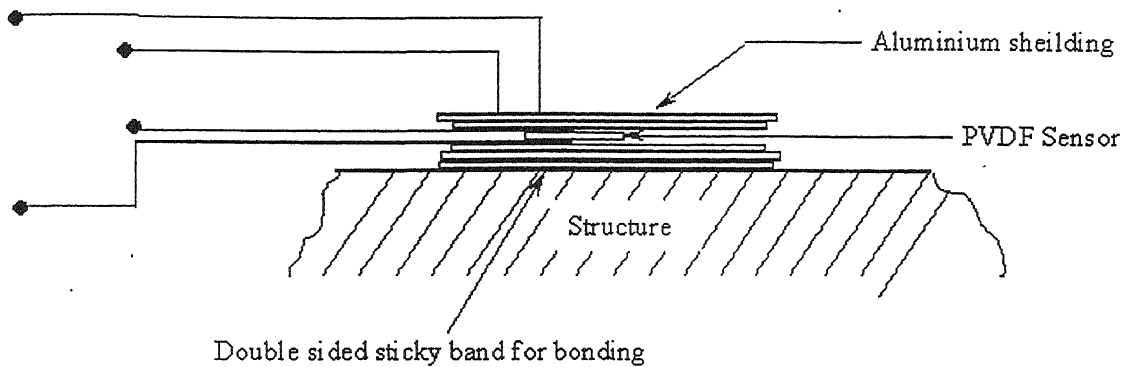


Fig 5.7 : Bonding of PVDF sensors

5.7 Experimental Set-Up

The experimental set up for the vibration control of the beam is shown in the Fig 5.7. The set up consists of two independent circuits. One circuit is used for the vibration control of the beam , whereas the other circuit is used to monitor the resulting vibration.

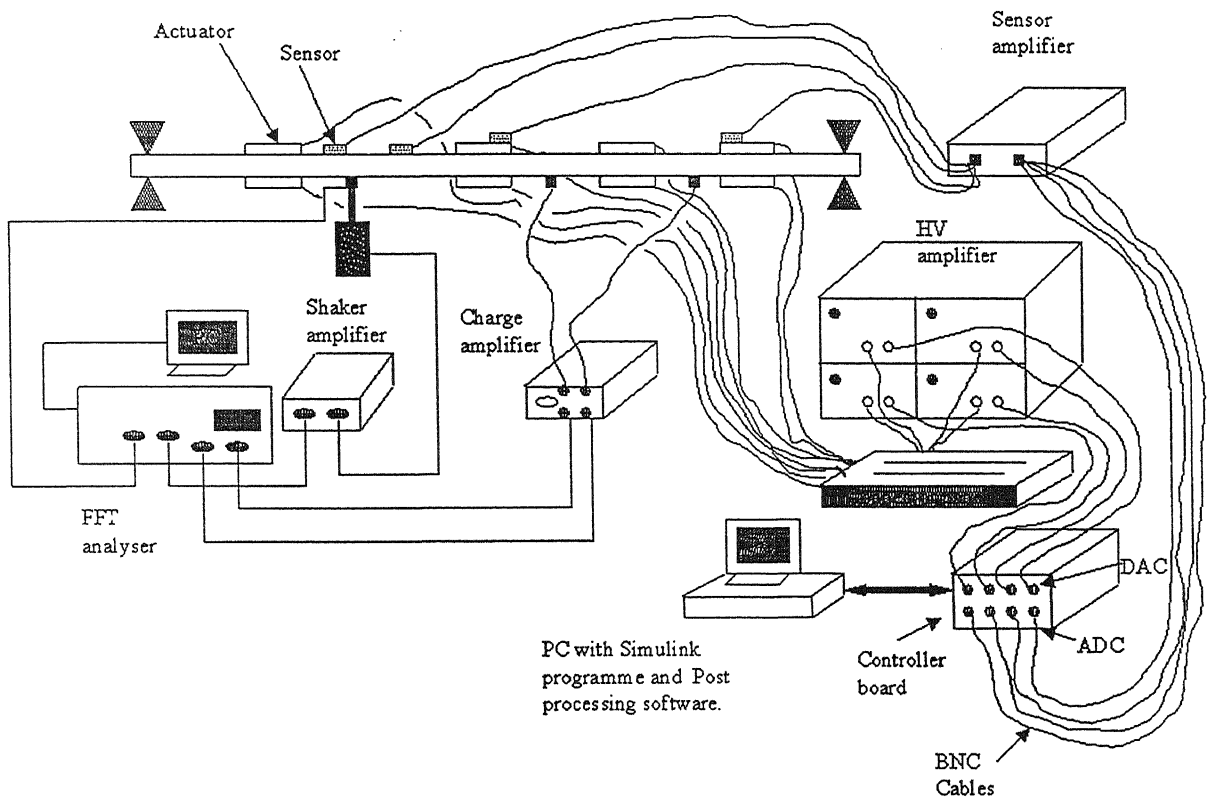


Fig 5.8 : Experimental set up for vibration control of the beam

The main part of the controller circuit is a four channel digital signal processor (DSP). After the control algorithm is generated on the PC and downloaded to the DSP, the DSP works stand alone with a sampling frequency of 20 kHz. The input channels of the DSP are connected via sensor amplifiers to four PVDF sensors. The PVDF material is mono oriented with $e_{31} = 4\text{pC/N}$ and $e_{32} = 0$. The amplification factor of the sensor amplifier is set to about 100. The controller board converts the analog signals into digital ones, calculates the modal velocities, integrates the modal velocities, multiplies the state vector with the gain matrix, calculates the retransformation by using the inverse input matrix and converts the digital result into analog signals. These signals are amplified by four high voltage amplifiers. The maximum amplifier voltage is limited to 100 volts so as to be well below the breakdown voltage of PZT, which would otherwise damage it. The output of all high voltage amplifiers is connected to the four PZT actuators.

The monitor circuit is independent from the control circuit. An electrodynamic shaker is used as vibration source and is integrated in the monitor circuit. ...The excitation force is sensed by a piezoelectric force transducer at the mounting of the gear box. The response of the structure is measured with two accelerometers at two different locations of the beam. These locations are selected to obtain significant peaks in the FRFs at the four controlled modes. The acceleration response from the accelerometers is obtained by writing a program on a HP-VEE machine which helps in generating sinusoidal excitation, sweeping through the frequency range 0-150 Hz and to record the acceleration response at each frequency.

5.8 Experimental Results

The control of the beam vibration is carried out After inserting the right gain coefficients. A good reduction of the vibration amplitude was observed after control. The fig 5.8 shows the modal velocity vs time plot with / without control for the fourth control mode at 148 Hz. The table 5.7 below shows the amount of reduction obtained in the amplitude of vibration for each mode as obtained from fig 5.9.

Mode No.	Frequency[Hz]	Reduction [%]
1	10	40%
2	37	62%
3	83	28%
4	149	74%

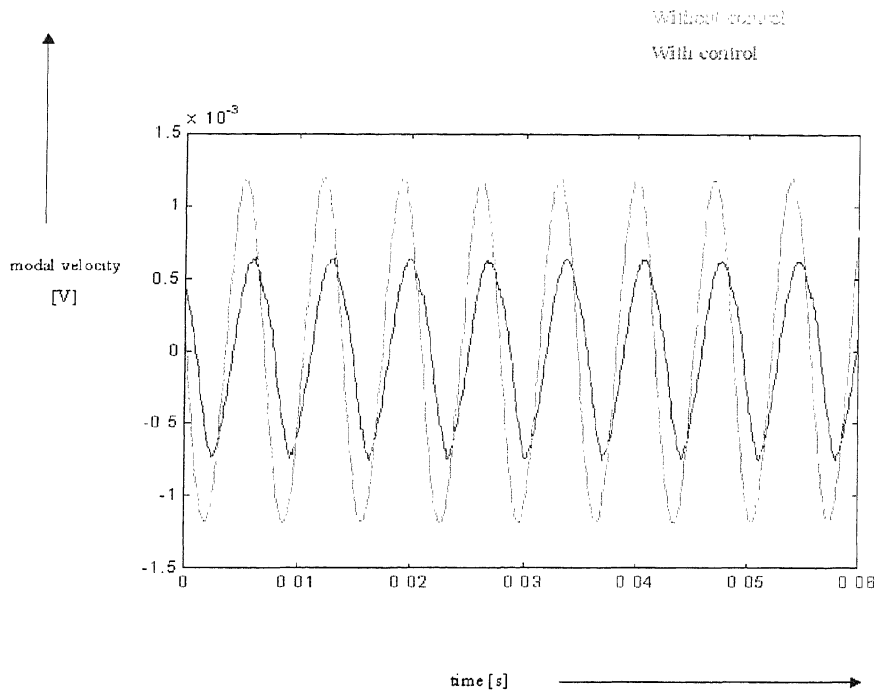
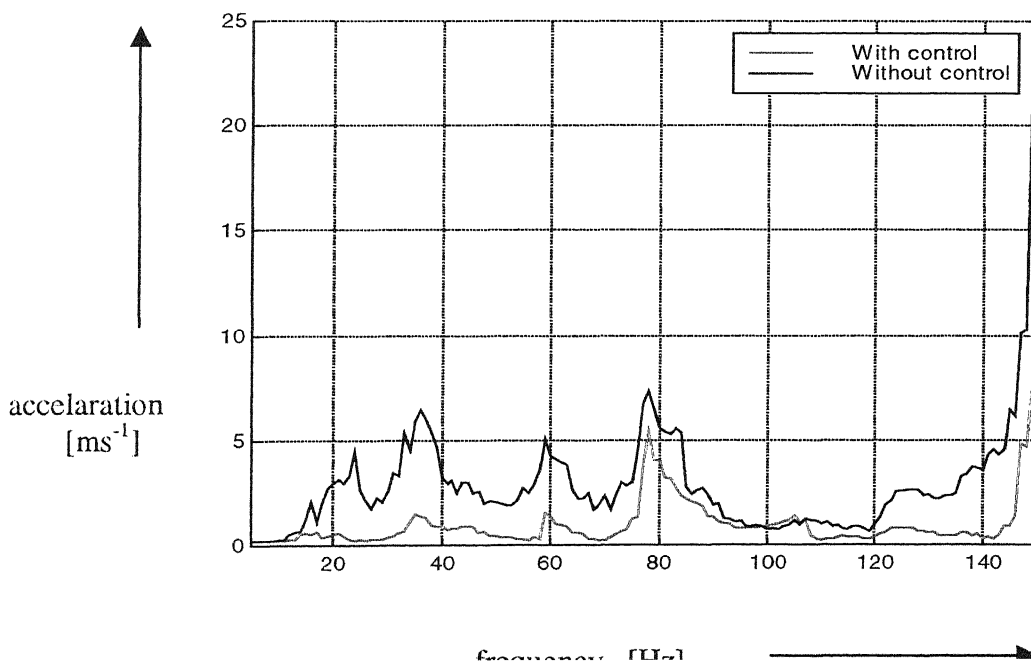


Fig 5.8 : Modal velocity vs time plot for the fourth mode

The above plot shows that there is a good reduction in the modal amplitudes for the fourth mode at 149 Hz. The acceleration vs frequency plot for the beam with and without control obtained after measuring the acceleration for each frequency at a point of maximum displacement is shown in the fig 5.9 below. It is clear from the figure that a good reduction in vibration is obtained for the first, second and fourth modes respectively. The shaker excitation was positioned at 23 cm along the x axis. The excitation was of 7 N magnitude.



Chapter 6

Active Structural Acoustic Control of a Car Structure

In numerous industrial applications, structurally radiated noise is a persistent problem which is often poorly alleviated by passive means, particularly at low frequencies. In ASAC the control inputs are applied directly to the structure in order to reduce or change the vibration distribution with the objective of reducing the overall sound radiation. Though it is obvious that completely reducing the overall structural response with active vibration control would lead to the attenuation of the sound radiation, various modes of vibrations have differing radiation efficiencies and some modes are better coupled to the radiation field than others. Hence, only selected modes need to be controlled, rather than the whole response. This chapter gives the details of experiment and results obtained after carrying out ASAC on a car hood. . Fig 6.1 shows a generic arrangement of a distributed elastic system excited by an oscillating disturbance.

In the experiment the car hood is the structural specimen. The car hood can be considered as a plate, although its shape is quite complex. The excitation is done with a point load excitation applied by a shaker. The modal information is obtained after performing an experimental modal analysis (EMA). The better radiating modes are identified by measuring the sound pressure. Effort to control these modes are done with the help of PVDF materials, applying the theory of plates with piezoelectric materials and controlling the vibration with help of modal filtered feedback.

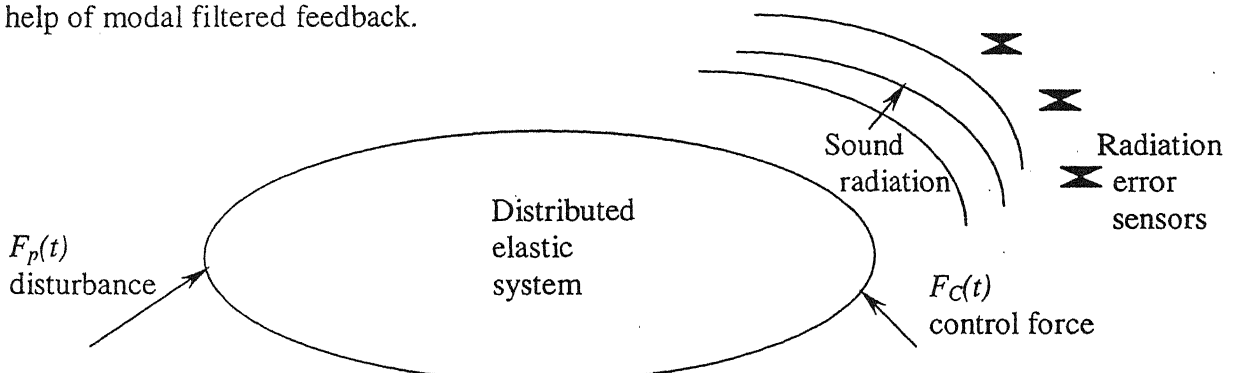


Fig 6.1 : General arrangement for ASAC

6.1 Sound Radiation of a Vibrating Surface – The Rayleigh Integral

A very brief introduction of the sound radiation of vibrating surfaces which is understood to perform the experiments is outlined here. The evaluation of the Rayleigh integral is probably the conceptually simplest approach for calculation of the sound field radiated by a vibrating flat surface which is imbedded into a rigid infinite plane. The Rayleigh integral gives the complex valued pressure at a given field point $p(r)$ in terms of the complex velocities $v(r_s)$ field onto the structure S .

It is given as follows

$$p(r) = \int_S \frac{j\omega\rho_0 v(r_s) e^{-jkR}}{2\pi R} dS, \quad (6.1)$$

where $R = |r - r_s|$ and $v(r_s)$ is the component of the complex velocity normal to the surface S , while ρ_0 is the density of the acoustic medium. Essentially the integral evaluates the sum of the fields of a distribution of elemental sources, each having a complex volume velocity $v(r_s)dS$. Fig 6.1 shows the rectangular plate in an infinite baffle showing nodal lines, coordinate system (r, θ, ϕ) and an elemental sound source associated with the plate motion.

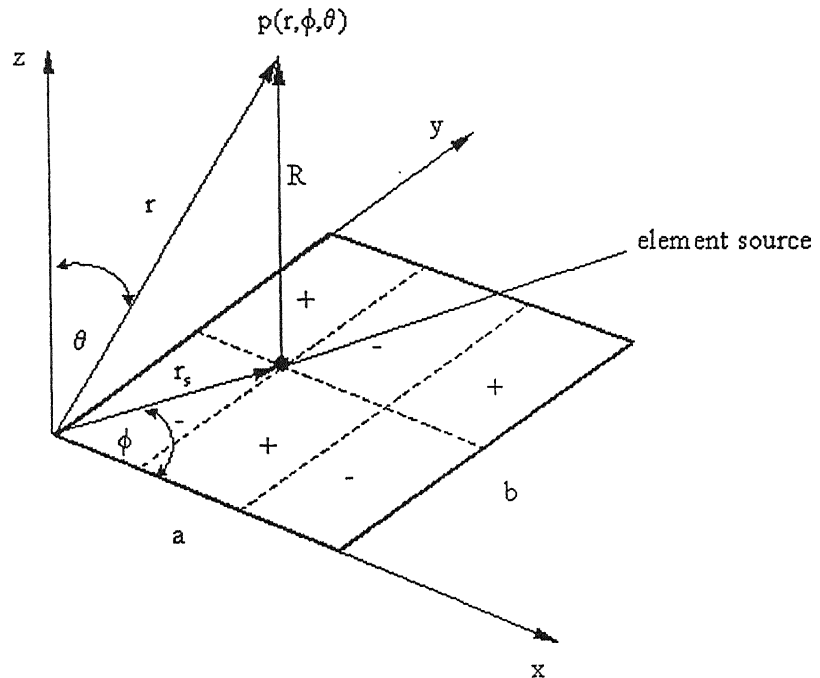


Fig 6.2 : An elemental sound source associated with plate radiation

The radiation efficiency (σ_{mn}) of different mode types in the low frequency range when the acoustic wavelength is much greater than the plate dimensions

ka (wave number) $\ll 1$, $a = b$ can be given as (Fuller [1])

for m, n both odd,

$$\sigma_{mn} \approx \frac{32(ka)^2}{m^2 n^2 \pi^5}, \quad (6.2)$$

for m odd , n even,

$$\sigma_{mn} \approx \frac{8(ka)^4}{3m^2 n^2 \pi^5}, \quad (6.3)$$

for m, n both even,

$$\sigma_{mn} \approx \frac{2(ka)^6}{15m^2 n^2 \pi^5}. \quad (6.4)$$

The dependence of the radiation efficiency of these mode classes on increasingly high powers of ka shows that the three classes exhibit radiation efficiencies which are respectively characteristic of monopole, dipole and quadrupole type sources as shown in the fig 6.2 below which illustrates the corner monopole model of low frequency plate radiation.

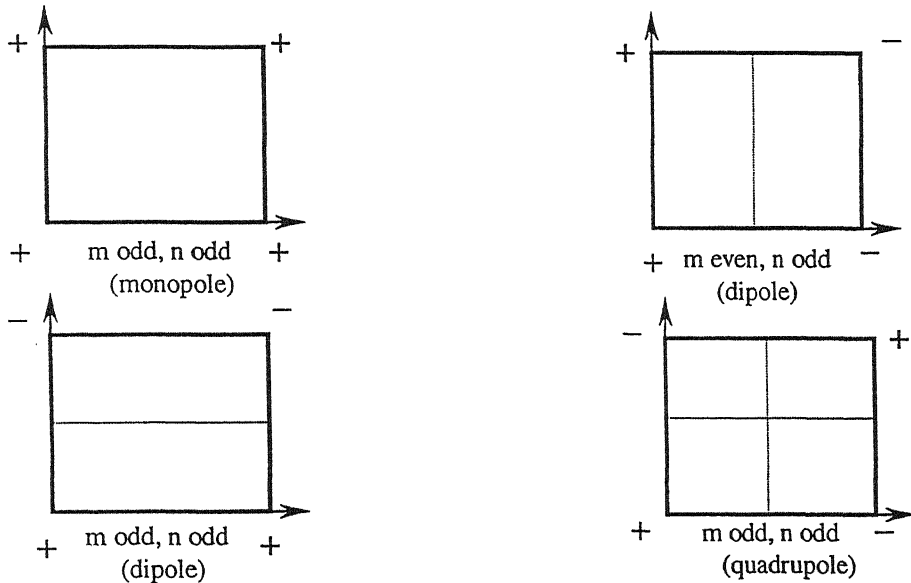


Fig 6.3 : Corner monopole model of low frequency plate radiation

Thus, it is clear that the odd-odd modes contribute more to sound radiation as compared to the other classes. In even-even mode case there is a perfect cancellation of the neighboring cells thus reducing the sound radiation. In the experiment with the car hood, the modes

The radiation efficiency (σ_{mn}) of different mode types in the low frequency range when the acoustic wavelength is much greater than the plate dimensions $ka(\text{wave number}) \ll 1$, $a = b$ can be given as (Fuller [1])

for m, n both odd,

$$\sigma_{mn} \approx \frac{32(ka)^2}{m^2 n^2 \pi^5}, \quad (6.2)$$

for m odd, n even,

$$\sigma_{mn} \approx \frac{8(ka)^4}{3m^2 n^2 \pi^5}, \quad (6.3)$$

for m, n both even,

$$\sigma_{mn} \approx \frac{2(ka)^6}{15m^2 n^2 \pi^5}. \quad (6.4)$$

The dependence of the radiation efficiency of these mode classes on increasingly high powers of ka shows that the three classes exhibit radiation efficiencies which are respectively characteristic of monopole, dipole and quadrupole type sources as shown in the fig 6.2 below which illustrates the corner monopole model of low frequency plate radiation.

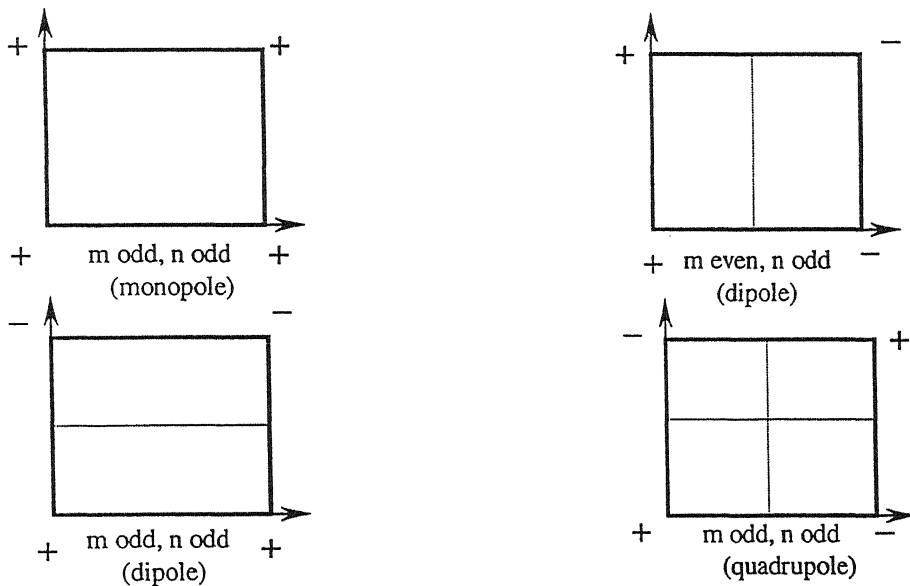


Fig 6.3 : Corner monopole model of low frequency plate radiation

Thus, it is clear that the odd-odd modes contribute more to sound radiation as compared to the other classes. In even-even mode case there is a perfect cancellation of the neighboring cells thus reducing the sound radiation. In the experiment with the car hood, the modes

which contribute to the sound radiation are identified after carrying out a sound pressure measurement, see also section 6.5.3.

6.2 Experimental Modal Analysis

An experimental modal analysis is decided to be carried out for finding the modal system parameter, namely the eigen frequencies ω_n , modal damping ratios ζ_n and the modal shape-function Ψ_n . This is the best procedure to obtain results from the car structure as it is quite difficult to model the geometry and the boundary conditions of the structure for a FEM analysis. In this sections the important concepts understood in order to carry out EMA are highlighted.

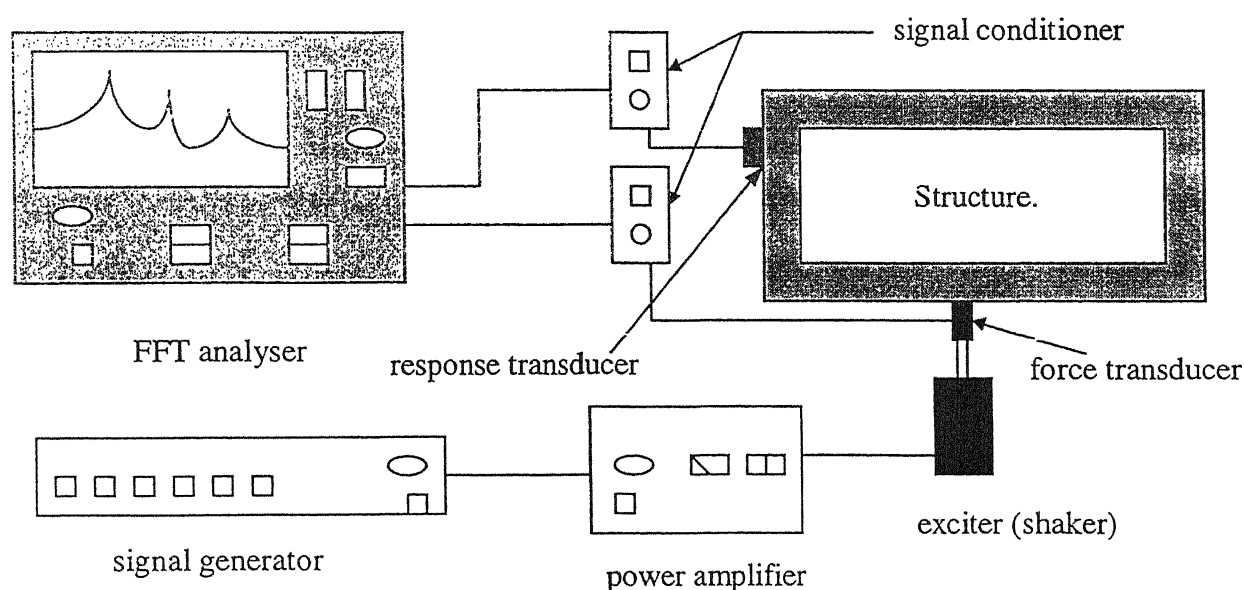
6.2.1 Used Hardware

Basically, there are three main measurement mechanisms for EMA, namely:

1. Excitation mechanism
2. Sensing mechanism
3. Data acquisition and processing mechanism

A schematic representation of the basic hardware is shown in Fig 6.3. In this figure the basic set up for an experimental modal analysis is illustrated.

The analyzer converts the analogue time domain signals generated by the transducers into digital frequency domain data that can be subsequently processed with the help of digital computers. The validity and accuracy of the experimental results basically depend on the understanding of signal acquisition and processing.



6.2.2 Building Blocks of the FRF Measurement

Linear Spectrum ($S_X(\Delta f)$, $S_F(\Delta f)$)

The linear spectrum is the frequency domain representation of the time history. Transformation from time to the frequency domain is accomplished with the Fast Fourier Transform (FFT). The linear spectrum is a complex function of frequencies with values at discrete frequencies determined by the frequency resolution (Δf) of the measurement. The response spectrum S_X is given by

$$S_x(m\Delta f) = \left(\frac{2}{T}\right) \Delta t \sum_{n=0}^{N-1} x(n\Delta t) e^{-j2\pi(m\Delta f)(n\Delta t)} \quad (6.5)$$

Auto power Spectrums : (G_{XX} , G_{FF})

The Auto power spectrum is the magnitude-squared of the linear spectrum and is real valued function of frequency. It is formed as the product of a linear spectrum S_X and its complex conjugate S_X^*

$$G_{XX} = S_X S_X^* . \quad (6.6)$$

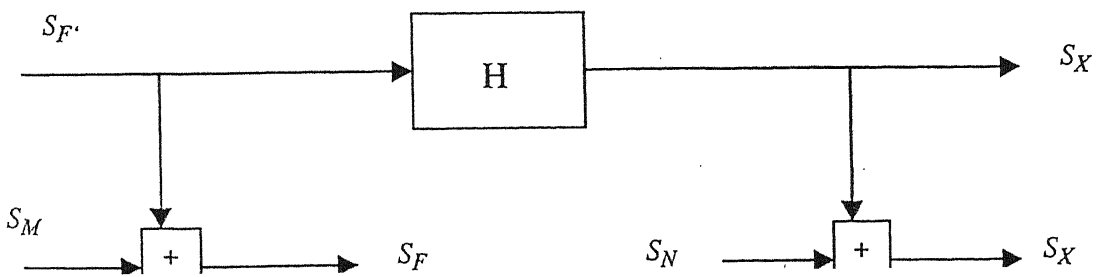
Cross power Spectrum : (G_{XF})

The Cross power spectrum is a measure of the mutual power between two measurements (e.g. input force and response). It is a complex valued function of frequency and contains relative phase information between each measurement component. It is formed as the product of the linear spectrum of the response and the complex conjugate of the linear spectrum of the input signal.

$$G_{XF} = S_X S_F^* . \quad (6.7)$$

6.2.3 Estimating the Frequency Response Function

A traditional measurement-system model used to describe the FRF measurement when noise is present on both measured input and response signals is shown in the block diagram below.



Linear spectrums :

$S_{F'}$ = Actual input force to the structure

S_M = Noise, uncorrelated with the input force

$S_F = S_{F'} + S_M$ = Measured force

$S_{X'}$ = Actual structural response

S_N = Noise, uncorrelated with response

$S_X = S_{X'} + S_N$ = Measured response

Required measurement :

It is required to measure the transfer function in the frequency domain (FRF) as

$$H = \frac{S_{X'}}{S_F} \quad (6.8)$$

The conventional frequency response function estimator H_1 (noise on the response only) is determined by using the cross input-output spectrum and the input auto-spectrum.

$$H_1 = \frac{G_{XF}}{G_{FF}} \quad (6.9)$$

Another version of the frequency response function estimator H_2 is obtained by normalizing the output auto-spectrum by the cross input-output spectrum:

$$H_2 = \frac{G_{XX}}{G_{FX}} \quad (6.10)$$

As H_1 and H_2 should give the same result, an indicator of the quality of the analysis can be defined as the ratio of these two estimators. Thus

$$\frac{H_1}{H_2} = \frac{G_{XF}}{G_{FF}} \frac{G_{FX}}{G_{XX}} = \frac{G_{XF}}{G_{FF}} \frac{G_{XF}^*}{G_{XX}} = \frac{|G_{XF}|^2}{G_{FF} G_{XX}} = \gamma^2 \quad \text{where } 0 \leq \gamma^2 \leq 1 \quad (6.11)$$

γ^2 is called the ordinary coherence function. It is a normalized coefficient of correlation between the measured input and response signals evaluated at each frequency. It is a real valued function of frequency which indicates the amount of response that is linearly related to the input signal. Its value ranges between zero (no relationship) and one (100% relationship).

The cross-section of the area where the actuator is placed on the plate is shown in fig 6.6 below. The strain distribution for the antisymmetric wafer configuration used is shown here.

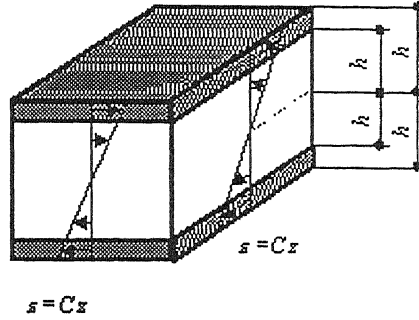


Fig 6.7 : Cross-section of the plate with the actuators on top and bottom

The actuator, which is bonded to the surface of the plate, generates the line moments m_x and m_y along the x- and y- axis (Fuller [1])

$$m_x = B_p C_x (H(x - x_1) - H(x - x_2)) (H(y - y_1) - H(y - y_2)), \quad (6.12)$$

$$m_y = B_p C_y (H(x - x_1) - H(x - x_2)) (H(y - y_1) - H(y - y_2)). \quad (6.13)$$

The constants C_x and C_y represent the gradient of the actuator induced strain and are given as

$$C_x = \frac{3h_I [(h_{ii} + h_{iv} E^*) (\frac{d_{31}}{h_a} + \nu_a \frac{d_{32}}{h_a}) + (h_{iii} \nu_a - h_{iv} E^* \nu_p) (\frac{d_{32}}{h_a} + \nu_a \frac{d_{31}}{h_a})]}{2[(h_{ii} + h_{iv} E^*)^2 - (h_{iii} \nu_a - h_{iv} E^* \nu_p)^2]}, \quad (6.14)$$

$$C_y = \frac{3h_I [(h_{ii} + h_{iv} E^*) (\frac{d_{32}}{h_a} + \nu_a \frac{d_{31}}{h_a}) + (h_{iii} \nu_a - h_{iv} E^* \nu_p) (\frac{d_{31}}{h_a} + \nu_a \frac{d_{32}}{h_a})]}{2[(h_{ii} + h_{iv} E^*)^2 - (h_{iii} \nu_a - h_{iv} E^* \nu_p)^2]}, \quad (6.15)$$

where

$$\begin{aligned} h_I &= h_4^2 + h_1^2 - h_3^2 - h_2^2, \\ h_{ii} &= h_4^3 + h_2^3 - h_3^3 - h_1^3, \\ h_{iii} &= h_3^3 + h_1^3 - h_4^3 - h_2^2, \\ h_{iv} &= h_3^3 - h_2^3. \end{aligned} \quad (6.16)$$

and

$$E^* = \frac{E_p (1 - \nu_a^2)}{E_a (1 - \nu_p^2)} \quad (6.17)$$

$H(\cdot)$ in (6.12) and (6.13) represents the Heaviside step function and x_1, x_2, y_1 and y_2 are the cartesian coordinates of the actuator boundaries. The line moments can be replaced by the equivalent loads as (Fuller [1])

$$\hat{p}_{zact}(x, y) = - \left(\frac{\partial^2 m_x(x, y)}{\partial x^2} + \frac{\partial^2 m_y(x, y)}{\partial y^2} \right). \quad (6.18)$$

The modal amplitude for vibration of a plate can be written down as, see also chapter 2.

$$\hat{q}_n = \frac{(\omega_n^2 - \Omega^2) - i(\omega_n^2 \eta)}{\rho t_p \Lambda [(\omega_n^2 - \Omega^2)^2 + \omega_n^4 \eta^2]} \int_{x_1}^{x_2} \int_{y_1}^{y_2} \hat{p}_{zact} \Psi_n(x, y) dy dx. \quad (6.19)$$

By substituting (6.18) in the above equation, the integral term can be written as

$$\int_{x_1}^{x_2} \int_{y_1}^{y_2} \hat{p}_{zact} \Psi_n(x, y) dx dy = -B_p \left(C_x \left[\frac{d\Psi_{1n}(x)}{dx} \right] \int_{x_1}^{x_2} \Psi_{2n}(y) dy + C_y \left[\frac{d\Psi_{2n}(y)}{dy} \right] \int_{y_1}^{y_2} \Psi_{1n}(x) dx \right) \quad (6.20)$$

where, $\Psi_n(x, y)$ is substituted as $\Psi_{1n}(x) \Psi_{2n}(y)$ and B_p is the bending stiffness of the plate

$$B_p = \frac{Et_p^3}{12(1-\nu^2)}.$$

Finally the input matrix can be created by calculating the modal input factors of each actuator and each mode. The input factors of an actuator are collected into a column and the input factors of a row are related to a mode. The input factor b_n for the n^{th} mode can be written down as

$$b_n = \frac{\int_{x_1}^{x_2} \int_{y_1}^{y_2} \hat{p}_{zact}(x, y) \Psi_n(x, y) dy dx}{\rho t_p \int_{x_1}^{x_2} \int_{y_1}^{y_2} \Psi_n^2(x, y) dx dy} \quad (6.21)$$

6.3.2 Output Matrix

The concept of point sensors allocated in an array is used in order to find the output matrix. PVDF point sensors are defined as thin piezoelectric films with small size compared to the wavelength of structural deformation. The modal sensor output factors can be arrived at after following the same procedure as outlined in chapter 2.

They are given by

$$\Psi_{in} = \frac{h_s}{\epsilon_{33}} \frac{(\frac{t_p}{2} + h_s)}{A} \left(e_{31} \int_{x_i}^{x_{i2}} \int_{y_i}^{y_{i2}} \frac{\partial^2 \Psi_n(x, y)}{\partial x^2} dy dx + e_{32} \int_{x_i}^{x_{i2}} \int_{y_i}^{y_{i2}} \frac{\partial^2 \Psi_n(x, y)}{\partial y^2} dy dx \right) \quad (6.2)$$

where A is the area of the sensor and x_{i1} , x_{i2} , y_{i1} and y_{i2} are the coordinates of the i^{th} sensor.

6.4 Interpolation of a shape-function

As illustrated in the section 6.3 the shapefunction $\psi_n(x, y)$ is required in an analytical closed form in order to calculate the input and output factors. The experimental results of the mode-shapes are available in the form of a table. Since small non-linearity's of the structure and curve fit errors lead to local deviations from the experimentally evaluated mode shapes, a direct use of the table is not possible. Hence an interpolation of the measured mode shapes with polynomials is required in order to smoothen out the local deviations and to generate a analytically closed form solution.

6.4.1 Interpolation by Using Lagrangian Polynomials

The interpolating polynomial of degree $N - 1$ through N points $z_{x1} = f(x_1)$, $z_{x2} = f(x_2)$, ..., $z_{xN} = f(x_N)$ is given explicitly by Lagrange's interpolation formula

$$\begin{aligned} \Psi_{1n}(x) = & \frac{(x - x_2)(x - x_3) \dots (x - x_N)}{(x_1 - x_2)(x_1 - x_3) \dots (x_1 - x_N)} z_{x1} + \frac{(x - x_1)(x - x_3) \dots (x - x_N)}{(x_2 - x_1)(x_2 - x_3) \dots (x_2 - x_N)} z_{x2} + \dots \\ & + \frac{(x - x_1)(x - x_2) \dots (x - x_{N-1})}{(x_{N1} - x_2)(x_{N1} - x_3) \dots (x_{N1} - x_{N-1})} z_{xN} . \end{aligned} \quad (6.2)$$

In the above expansion, there are N terms, each a polynomial of degree $N - 1$ and each constructed to be zero at all x_j except one, at which it is constructed to be z_{xj} . The same interpolation is used in the y - direction.

$$\begin{aligned} \Psi_{2n}(y) = & \frac{(y - y_2)(y - y_3) \dots (y - y_N)}{(y_1 - y_2)(y_1 - y_3) \dots (y_1 - y_N)} z_{y1} + \frac{(y - y_1)(y - y_3) \dots (y - y_N)}{(y_2 - y_1)(y_2 - y_3) \dots (y_2 - y_N)} z_{y2} + \dots \\ & + \frac{(y - y_1)(y - y_2) \dots (y - y_{N-1})}{(y_{N1} - y_2)(y_{N1} - y_3) \dots (y_{N1} - y_{N-1})} z_{yN} . \end{aligned} \quad (6.2)$$

The displacement field in x - and y -direction is composed into a product of the polynomials $\Psi_{1n}(x)$ and $\Psi_{2n}(y)$,

$$\Psi_n(x, y) = \Psi_{1n}(x) \Psi_{2n}(y). \quad (6.2)$$

The sampling points x_j and y_j are selected from the measured data. In practice the sampling points are chosen by regarding the mesh plots of each single mode shape. The lines of the mesh which show the maximum displacements and no local displacements are chosen to be the reference lines. For each coordinate x and y one reference line has to be defined. The sampling points are selected from the reference lines and plugged into the interpolation expansions (6.23) and (6.24). The necessary number of sampling points depended on the complexity of the mode shape considered.

6.4.2 Determination of Coefficients of the Lagrangian Polynomials

The determination of the input / output matrices starts with the calculation of the integrals involving the form function Ψ . To make the integration easier, a method of finding the coefficients of the interpolating polynomial is used. The idea is thus to write down the interpolating polynomial as

$$z_x = \Psi_{1n}(x) = c_1 + c_2x + c_3x^2 + \dots + c_Nx^{N-1} \quad (6.26)$$

where the c_i^s are required to satisfy the linear equation

$$\begin{bmatrix} 1 & x_1 & x_1^2 & \dots & x_1^{N-1} \\ 1 & x_2 & x_2^2 & \dots & x_2^{N-1} \\ \vdots & \vdots & \vdots & \ddots & \vdots \\ \vdots & \vdots & \vdots & \ddots & \vdots \\ 1 & x_N & x_N^2 & \dots & x_N^{N-1} \end{bmatrix} \begin{bmatrix} c_1 \\ c_2 \\ \vdots \\ c_N \end{bmatrix} = \begin{bmatrix} z_{x1} \\ z_{x2} \\ \vdots \\ z_{xN} \end{bmatrix} \quad (6.27)$$

(This is the so called *Vandermonde matrix* which has the problem of being quite ill-conditioned.)

Similarly it could be written that,

$$z_y = \Psi_{2n}(y) = c_1^* + c_2^*y + c_3^*y^2 + \dots + c_N^*y^{N-1}. \quad (6.28)$$

The coefficients c_i and c_i^* can be found out by making use of the function value interpolation written down in (6.23) and (6.24). If (6.23) is interpolated to find the value of the interpolating polynomial at $x = 0$, then this value is evidently c_1 . Now c_1 is subtracted from z_{xj}^s and each is divided by corresponding x_i . Throwing out one point (one with the smallest

x_i being the best candidate) the procedure could be repeated to find c_2 and so on (Numerical Recipes [20]).

After getting the coefficients and plugging in (6.25), the values of $\Psi_n(x,y)$ is then substituted into (6.21) and (6.22). The integration is then carried out and the values of input and output matrices can be found.

6.5 Experiments and Results

The experiments carried out to control the vibration and sound radiation of the car hood is outlined in this section.

6.5.1 Set Up for Experimental Modal Analysis of the Car Structure

The first and foremost part to perform the EMA on the car structure is to form the grid on the hood to approximate the geometry of it. The size of the hood is 130 x 138 cm. 400 grid points are set out on the hood, with a resolution of each grid being 5x5 cm approximately. The geometry is subsequently build up in the post-processing software with the approximation that the car hood closely represents a plate structure. The structure is checked up for linearity before going on with the EMA. This is done using the reciprocal theorem according to which the FRF of the response at one point due to the excitation at a second point must be same as the FRF of the response of second point due to excitation of the first. The impulse hammer is used as the exciter. Three acceleration transducers are used for obtaining the response.

The experimental set up is illustrated in fig 6.8. After choosing a good excitation point the response function (FRF) from each point is found by exciting this point with the hammer. Since the FFT analyzer is equipped with only four channels the measurement is repeated several times by changing the position of the acceleration transducers. The coherence function provides a check on how good the measurements are thereby helping in evaluating the influence of noise and uncorrelated signals. Results with coherence between 0.9 and 1 are the ones, accepted for further processing. The measured data are windowed with the help of a exponential window.

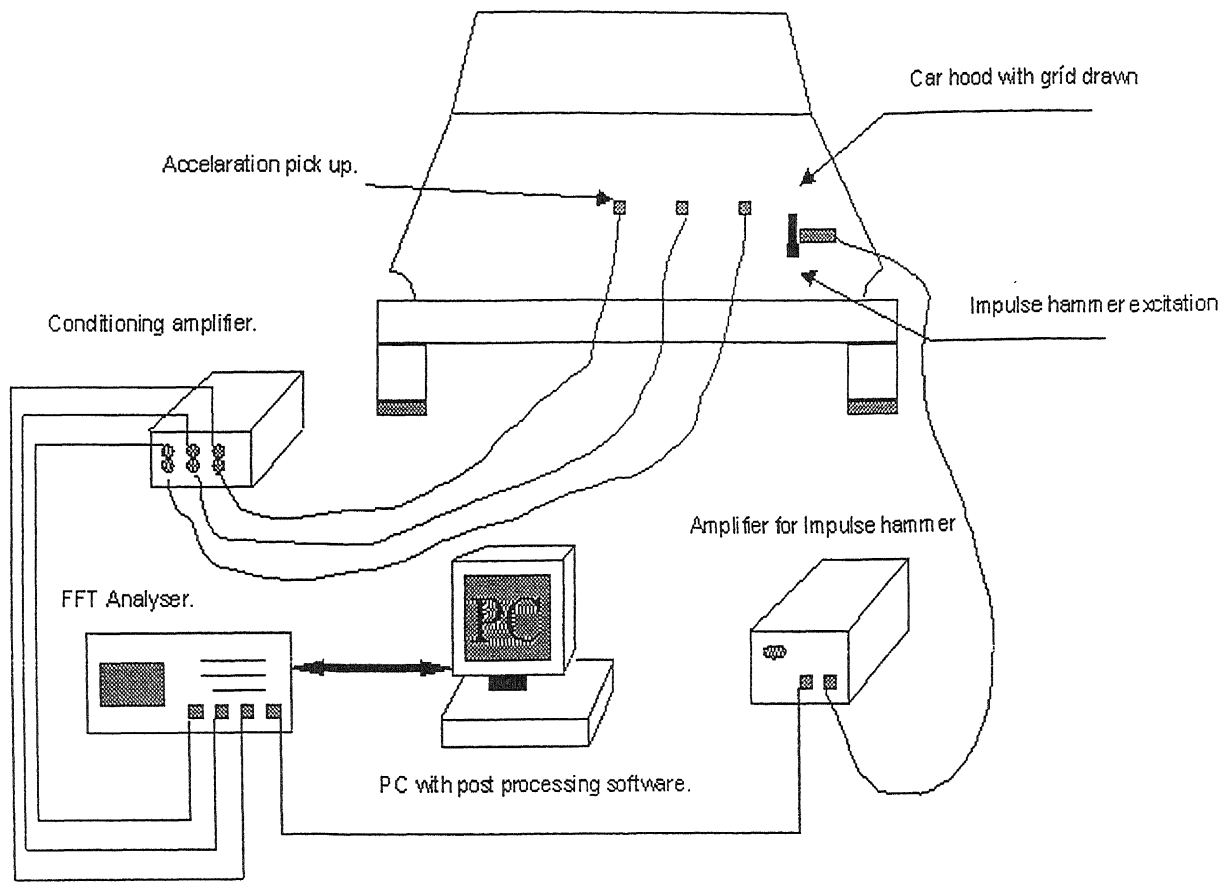


Fig 6.8 : Experimental set up for experimetal modal analysis

After measurement is complete the curve-fit process is used to obtain the modal parameters. The curve fit is done with various methods. The global and residues curve fit yields reasonable form-functions.

6.5.2 Results of the Experimental Modal Analysis

After carrying out the EMA on the car hood, and finishing the curve fit process the modal information is found. The table 6.1 gives the values of natural frequencies and the modal damping ratios of the first 10 modes.

The shape of the frequency response function is obtained after a modal peak search , which is an average of all FRFs at 400 points, is shown in fig 6.9.

No	Frequency [Hz]	Damping ratio [%]
1	36.14	6.42
2	50.60	3.92
3	53.81	6.02
4	76.32	2.64
5	82.23	3.94
6	90.87	2.51
7	97.08	4.30
8	99.73	2.16
9	107.88	2.89
10	119.84	2.31

Table 6.1 : Eigen-frequency and damping ratios

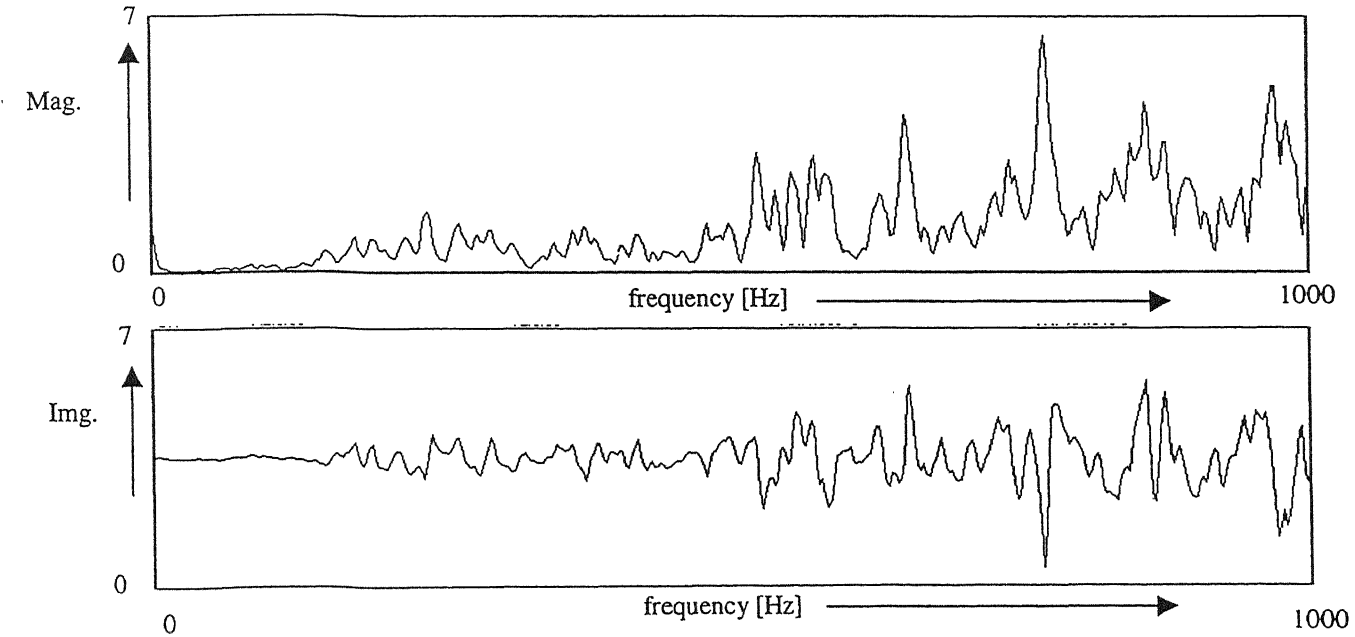
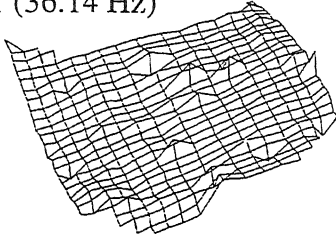


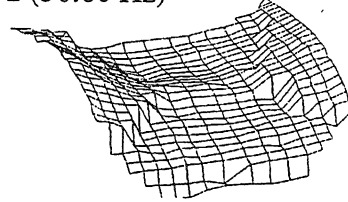
Fig 6.9 : Frequency response function

The first four computed mode shapes are shown below. The mode shapes are found to be separate modes with no coupling after looking into the modal assurance criteria which gives a check of orthornormality of the eigen modes.

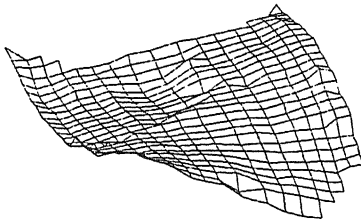
Mode 1 (36.14 Hz)



Mode 2 (50.60 Hz)



Mode 3 (53.81 Hz)



Mode 4 (76.32 Hz)

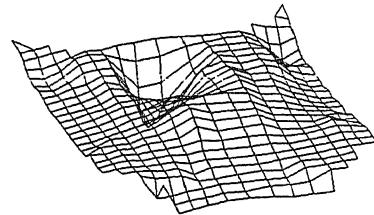


Fig 6.10 : First four mode shapes of the hood

All mode shapes in the lower frequency range of interest (100 – 400 Hz), are very complex in nature. In addition, the density of modes is high. Around 20 modes are present in the first 200 Hz. Hence, a visco-elastic passive damping coating is applied onto the bottom of the hood, to decrease the density of the mode shapes.

6.5.2.1 EMA results with Passive Damping Coat

The passive damping coating is cut out from a large viscoelastic sheet and fixed under of the hood. By using a passive layer non-linearity is introduced into the structure. However, since the coherence function is still of good quality it is assumed that the non-linearity is not large, therefore EMA can be carried out. The results of the EMA shows that the eigen modes in the lower frequency range are still present and the modes in the higher frequency range are damped out. In addition the eigen frequencies in the lower frequency band are found to be the same as these without the passive treatment. The FRF of the hood with passive coating is shown below, it is clearly seen that the peaks have blunted out showing that more damping is present. The magnitude of FRF has reduced and the modes in the higher frequency range have been damped out

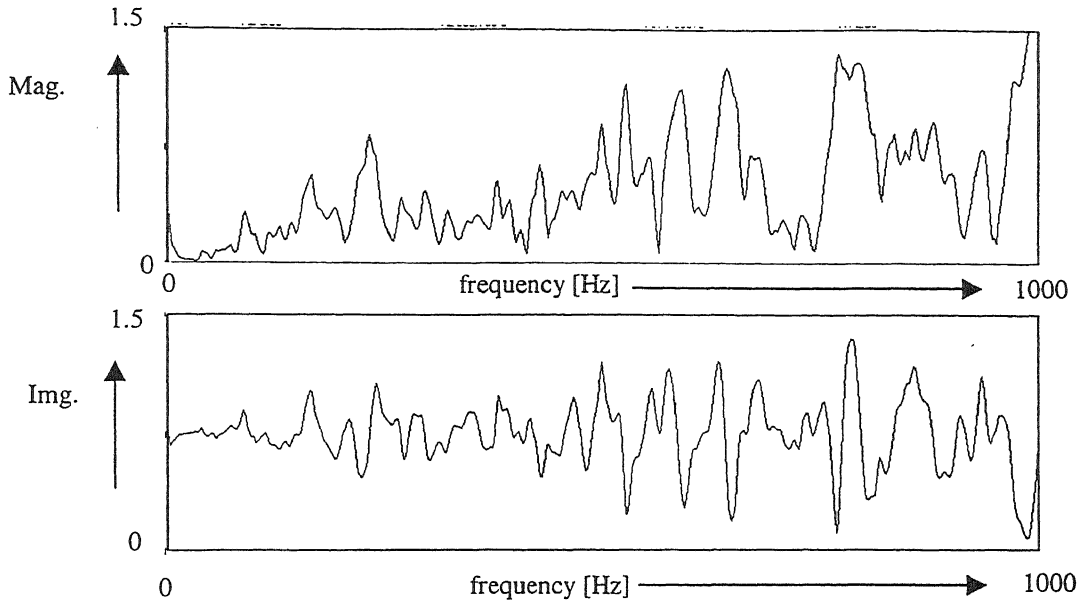
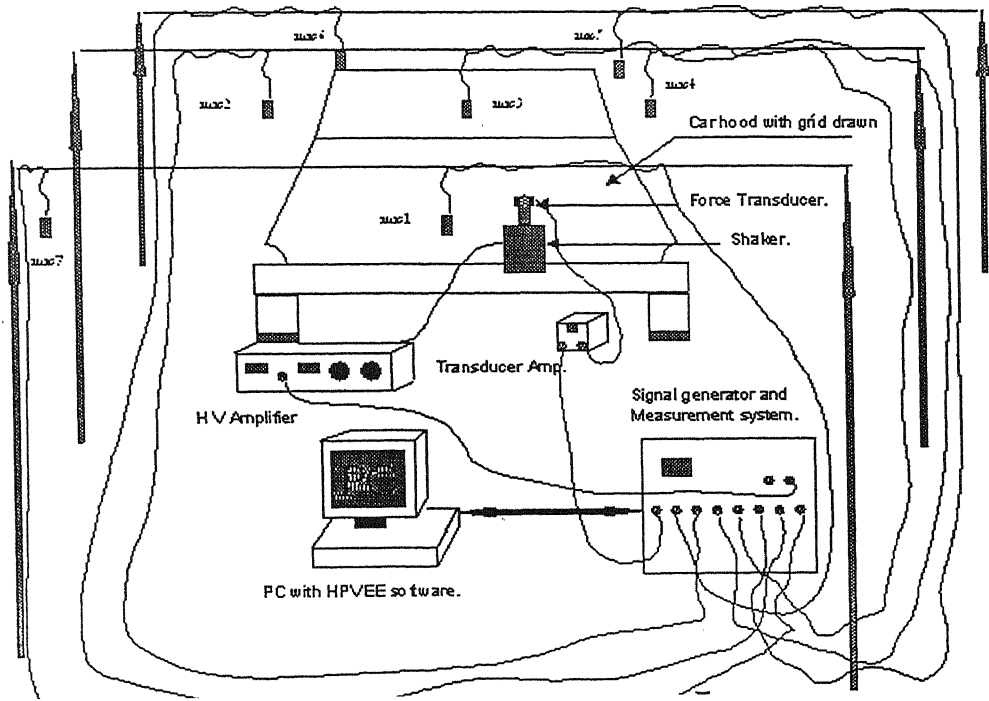


Fig 6.11 FRF of the passive damped hood

6.5.3 Experimental Set Up for Sound-Pressure Measurement

The purpose of the sound-pressure measurement is to identify those modes which make a maximum contribution to the sound radiation. For this an experimental set up as shown in the Fig. 6.7 is utilized. Seven microphones are used to find out the far-field acoustic radiation of the hood. The electrodynamic shaker is used for the excitation of the structure. The point of excitation is chosen that the shaker excitation could excite all the modes in the frequency range of interest (100 - 400 Hz).



The more accurate sound power measurement is not carried out here. Hence the microphones are placed in such a manner that maximum local information could be obtained from various parts of the hood. Microphones are placed above the center, at the outer edges, in the front and back of the hood by placing them such that the information from the far field is obtained. The readings from the microphones helps in the identification of the modes which couple effectively to the acoustic media. A HP-VEE measurement system is used for generation of sinusoidal signals for excitation of the hood. The signal is swept through the frequency range of interest with a step size of 0.5 Hz. A PI-control algorithm is written to ensure constant force excitation into the structure. A stand alone time of 30 seconds is set before the measurements from the microphones are recorded. This is done to achieve steady state condition for the vibration.

6.5.4 Results of Sound Pressure Measurement

The sound pressure measurement is carried out with and without the passive damping coating applied on the car hood. The graph below shows the sound pressure distribution over the frequency range of interest for a constant steady state sinusoidal excitation of 45 N, which is the average of the readings obtained from each microphone.

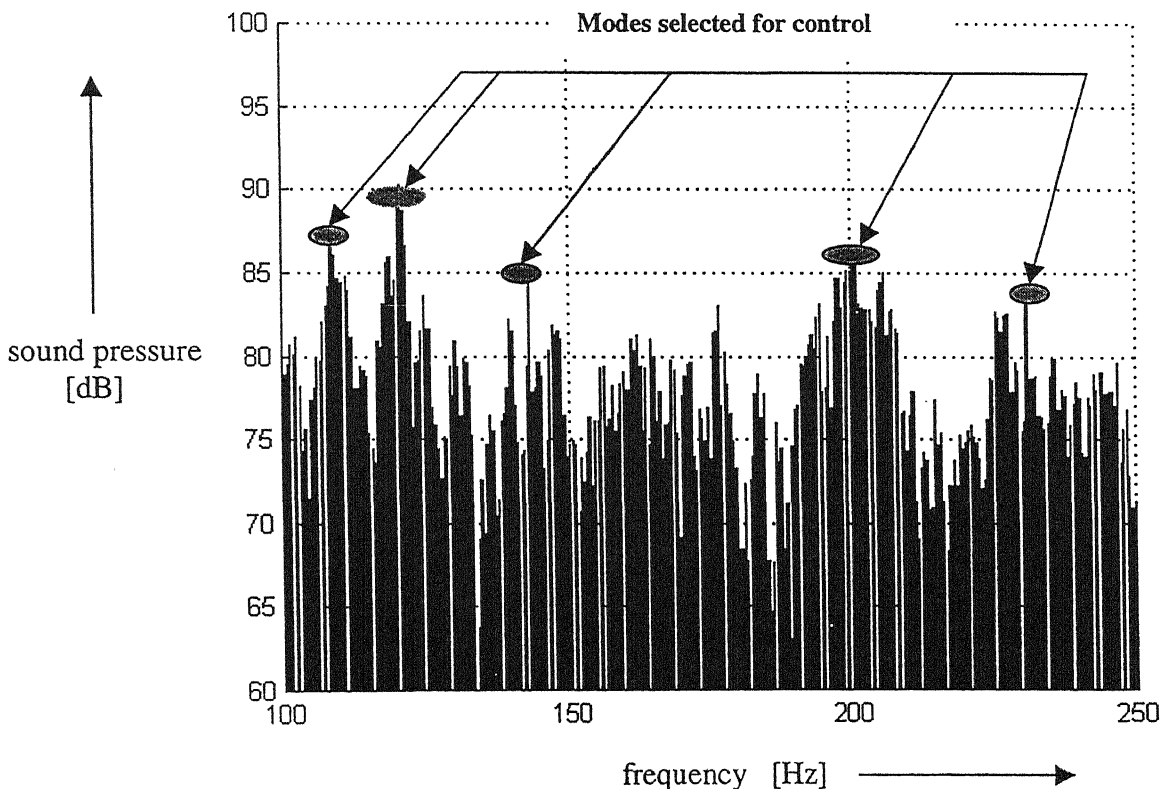


Fig 6.13 : Bar chart of the sound pressure measurement

Five modes which contribute significantly to the sound radiation characteristics are identified and selected for control. These five modes in the frequency range of interest are listed in table 6.2 .

No:	1	2	3	4	5
Eigenfrequencies of selected modes [Hz]	107 Hz	119 Hz	144 Hz	200 Hz	237 Hz

Table 6.2 Modes selected for control of sound radiation

Another interesting observation is that the effectiveness of the passive damping treatment on controlling sound radiation is more predominant in the higher frequency range and less effective in the lower frequency range. The figure below gives an illustration of comparison of the sound pressure measurement, which are averaged of all microphones conducted on the hood with and without passive coating.

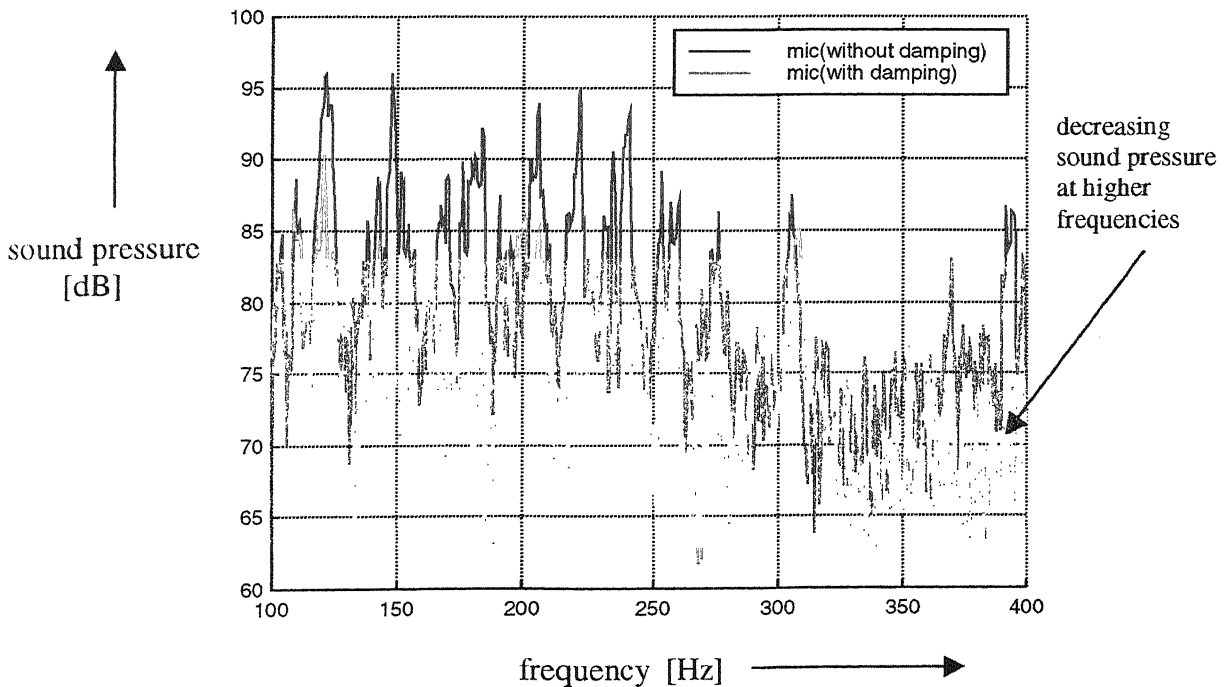
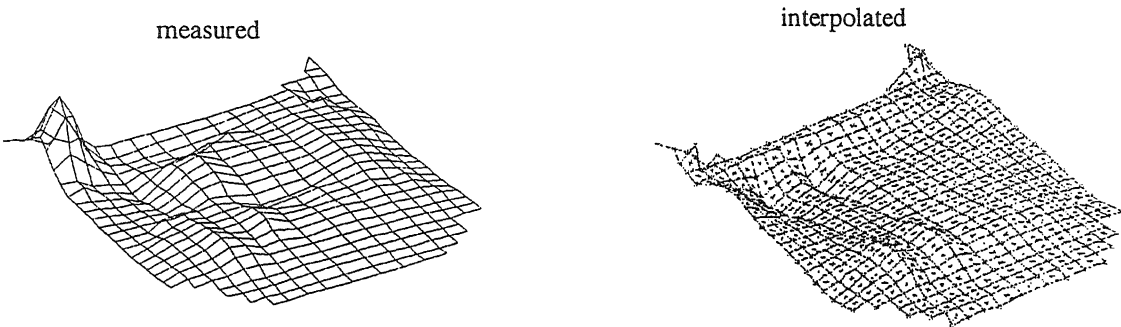


Fig 6.14 : Sound pressure with and without passive damping coat

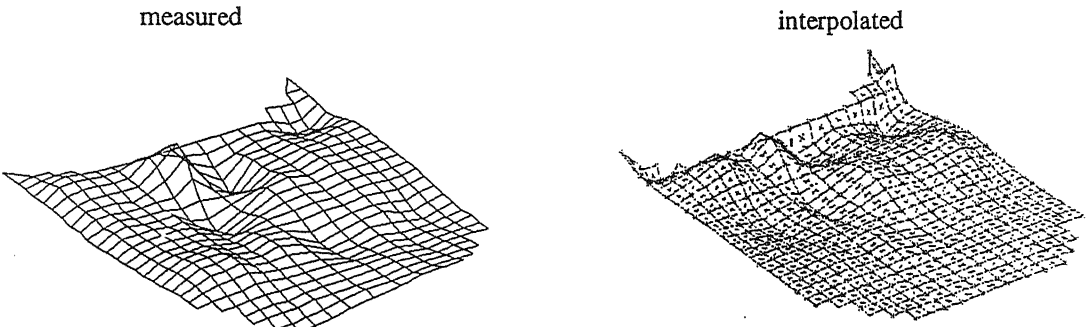
6.5.5 Interpolated Mode Shapes of Controlled Modes

Interpolation of the eigen function (ψ) of all five identified modes for control is carried out as stated in section 6.5. Thus, the eigen function could be computed into an analytical form for finding the B and C matrices. The original and interpolated mode shapes are shown in fig 6.12. The interpolated mode shapes are more or less free from the local faults in the original modes. The interpolated mode shapes are accepted to resemble the original shapes based on the number of points in phase and error in displacement of each point. The best shape which shows a low value for both the aforesaid comparison parameters are used as the interpolated eigen function for further analytical work. The fig 6.14 gives both the original and interpolated mode shapes for all five modes selected for control.

MODE 1 (109 Hz)



MODE 2 (119 Hz)



MODE 3 (144 Hz)



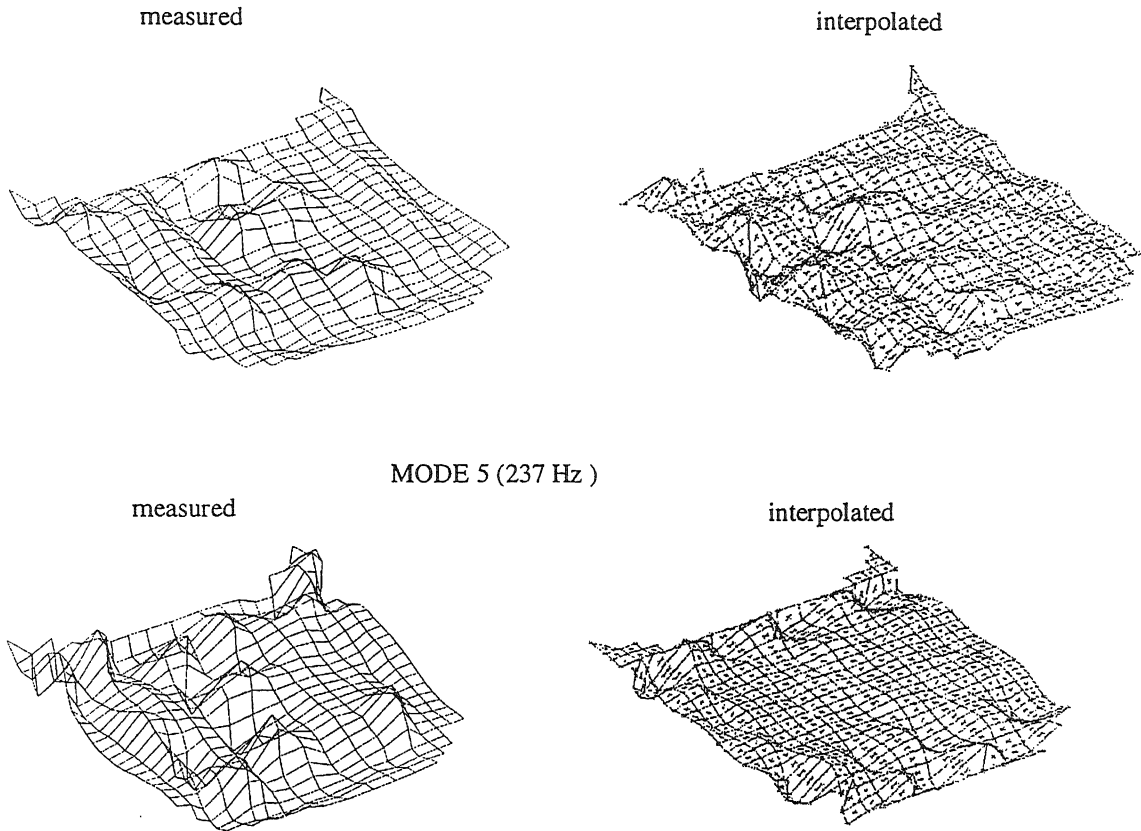


Fig 6.15 : Measured and interpolated mode shapes

6.6 Actuator and Sensor Placements

The sensor and actuator placements are decided by going through the procedure outlined in Chapter 4. In this section the placement of five actuators and sensors on the car hood is illustrated.

6.6.1 Actuator Placement

The PVDF actuators are placed based on the actuator placement indices and control performance indices. If the values of α_{a2} and $\alpha_{a\infty}$ are higher than a satisfactory limit, the positions of the actuator are accepted for control. Further, the FRF's of the structure excited by a shaker is compared with that of the structure excited by the actuators. Thus the actuator positions selected by getting a good control performance index is further checked for good performance in controlling the selected modes. Big sheets of PVDF materials, which measure 24x20 cm, are used to obtain larger line moments induced into the structure. Table 6.3 and fig.

6.15 give the positions of the selected PVDF actuators on the hood. The values of various control performance indices for the selected actuator position are shown in the Table 6.4.

No.	x_1 coordinate	x_2 coordinate	y_1 coordinate	y_2 coordinate	unit
1	-94	-67.5	2.3	21.3	cm
2	-94	-67.5	23	42	cm
3	-94	-67.5	50.5	69.5	cm
4	-51	-24.5	-15.5	3.5	cm
5	-44	-17.5	29.5	48.5	cm

Table 6.3 : Positions of PVDF actuators on the car hood

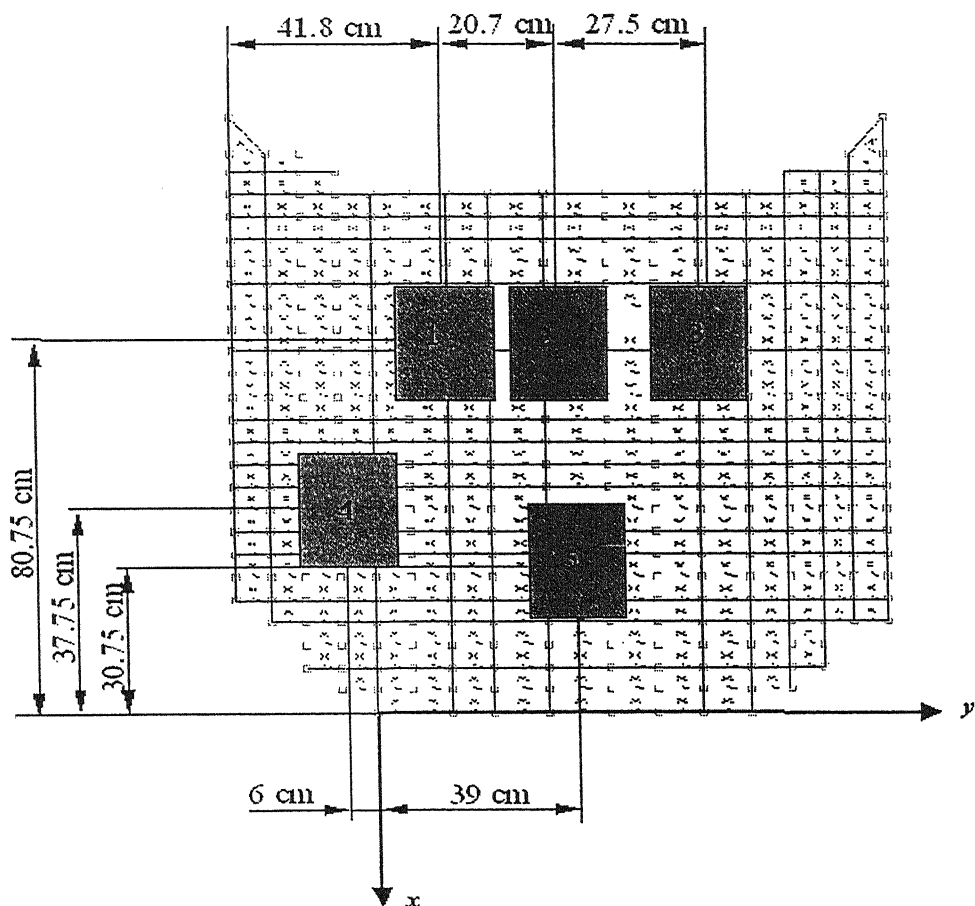
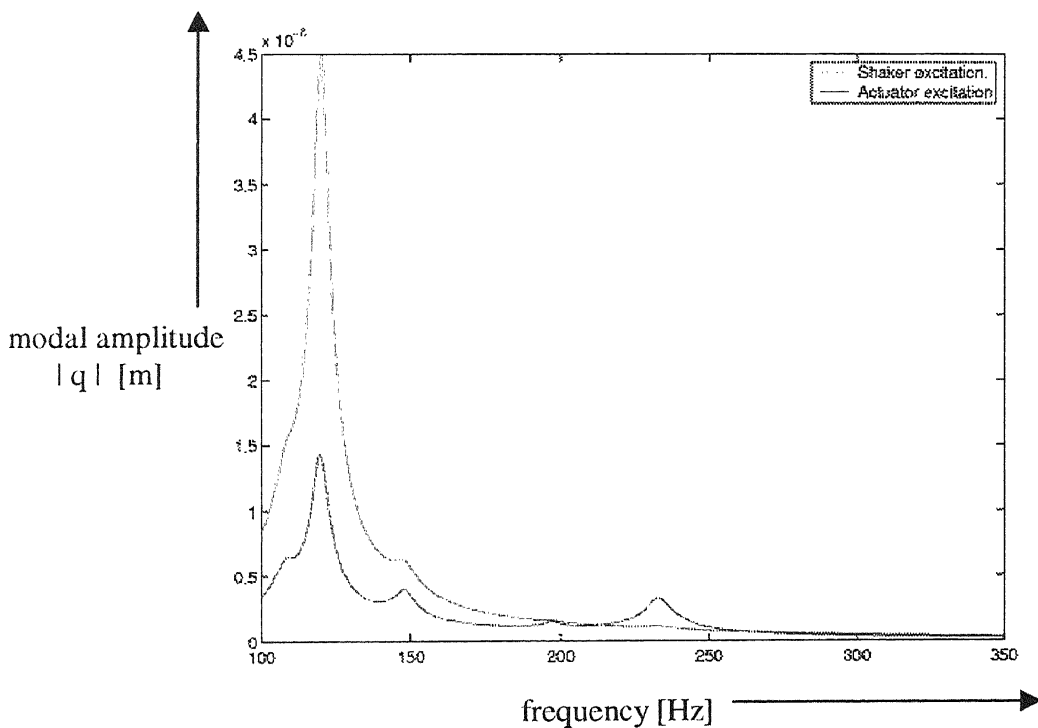


Fig 6.16 : Positions of PVDF actuators on the car hood

α_{a2}	0.35060
$\alpha_{a\infty}$	0.26350
β_{a2}	0.19774
$\beta_{a\infty}$	0.14918

Table 6.4 : Control performance indices for actuator locations

The above obtained values of control performance indices for the actuator position is the best obtained after iteration of different positions of the actuators. The fig. 6.16 below gives the comparison of a shaker excited FRF and actuator excited FRF for sinusoidal excitation. The program to calculate the FRF is based on (6.19). The actuator positions are adjusted so that the shape of the FRF of the actuator position excites the modes in the same way as excited by the shaker.

**Fig 6.17 : FRF shapes of the shaker and actuator induced sinusoidal excitation**

6.6.2 Sensor Placement

The placement of PVDF sensors which are bioriented ($e_{31}=e_{32} = 4\text{pC/N}$) is based on the modal analysis of the structure, its indices and the condition of the output matrix. The

initial sensor locations for iteration are selected to be the points of antinodes of the control modes as these are the points of maximum curvature. The positions are changed to achieve the best condition and hence the best measurability index. The table 6.6 gives the values for the performance indices, condition and the measurability index for the selected sensor locations shown in fig 6.17 and documented in table 6.5.

No.	x_1 coordinate	x_2 coordinate	y_1 coordinate	y_2 coordinate	unit
1	-75.75	-74.25	46.25	47.75	cm
2	-35.75	-34.25	-0.75	0.75	cm
3	-30.75	-29.25	46.25	47.75	cm
4	-20.75	-19.25	22.75	24.25	cm
5	-15.75	-14.25	46.25	47.75	cm

Table 6.5 : Position of PVDF sensors on the car hood

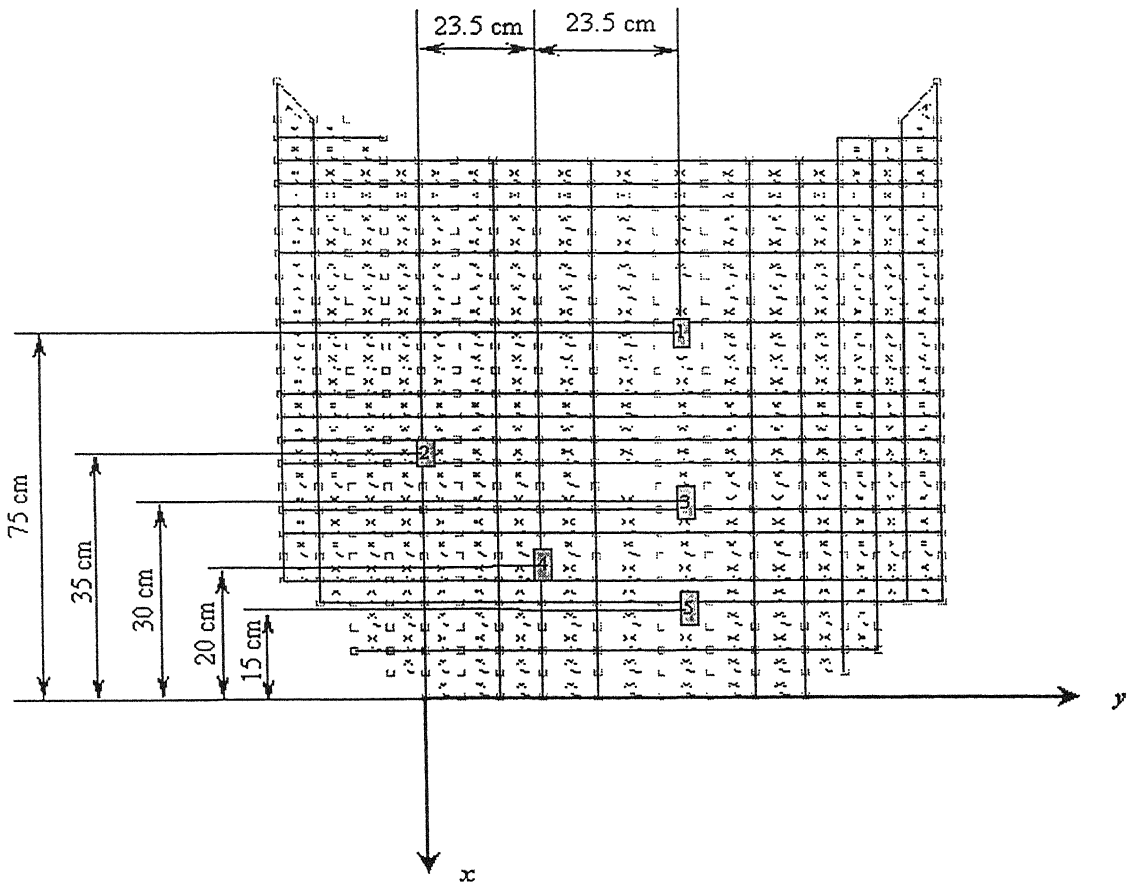
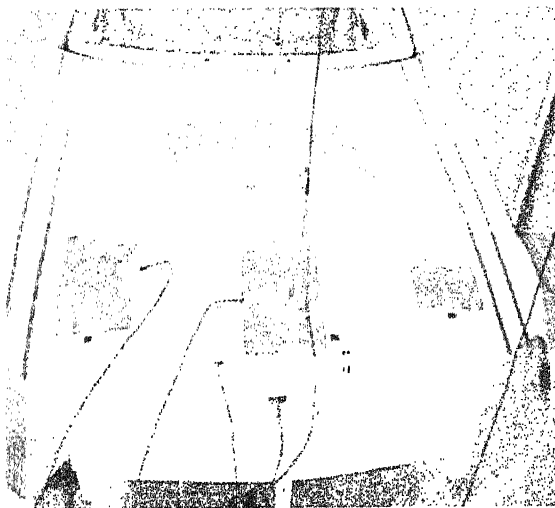


Fig 6.18 : Sensor positions on the Car hood

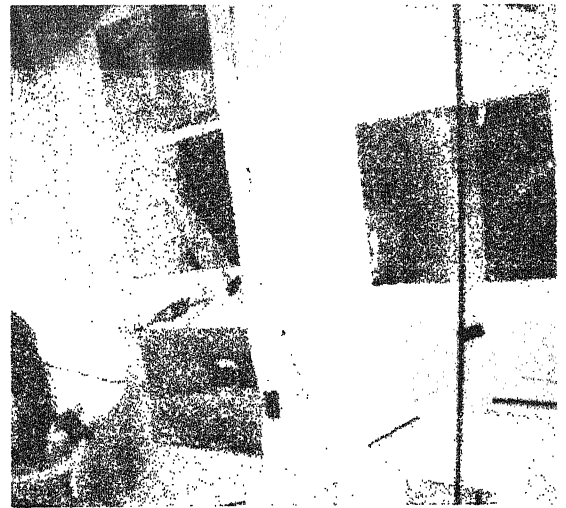
α_{a2}	0.41003
$\alpha_{a\infty}$	0.35703
β_{a2}	0.36954
$\beta_{a\infty}$	0.32533
<i>Cond [C]</i>	7.5725
i_s	0.54144

Table 6.6: Performance indices for the selected sensor combination

The photographs of the actuators and sensors placed on the car hood are shown in fig 6.18 and in the Appendix 5. [a] shows the placement of the PVDF actuators and sensors on top and [b] shows the actuators on the bottom of the hood. The shaker and the point of excitation can also be seen in the second picture. In the performed experiments to control the modes of vibration, only three modes could be controlled as two of the sensors are placed in wrong position due to measurement mistakes. The three sensors and actuators are reconfigured to control the last three modes.



[a]



[b]

Fig 6.19 : PVDF actuators / sensors placed on [a] top and [b] bottom of the hood

6.7 Experimental Set Up for Vibration Control

The experimental set up to control the vibration of the car structure is depicted in fig 6.20. As with the beam experiment the set up consists of two independent circuits, namely the controller circuit and the monitor circuit.

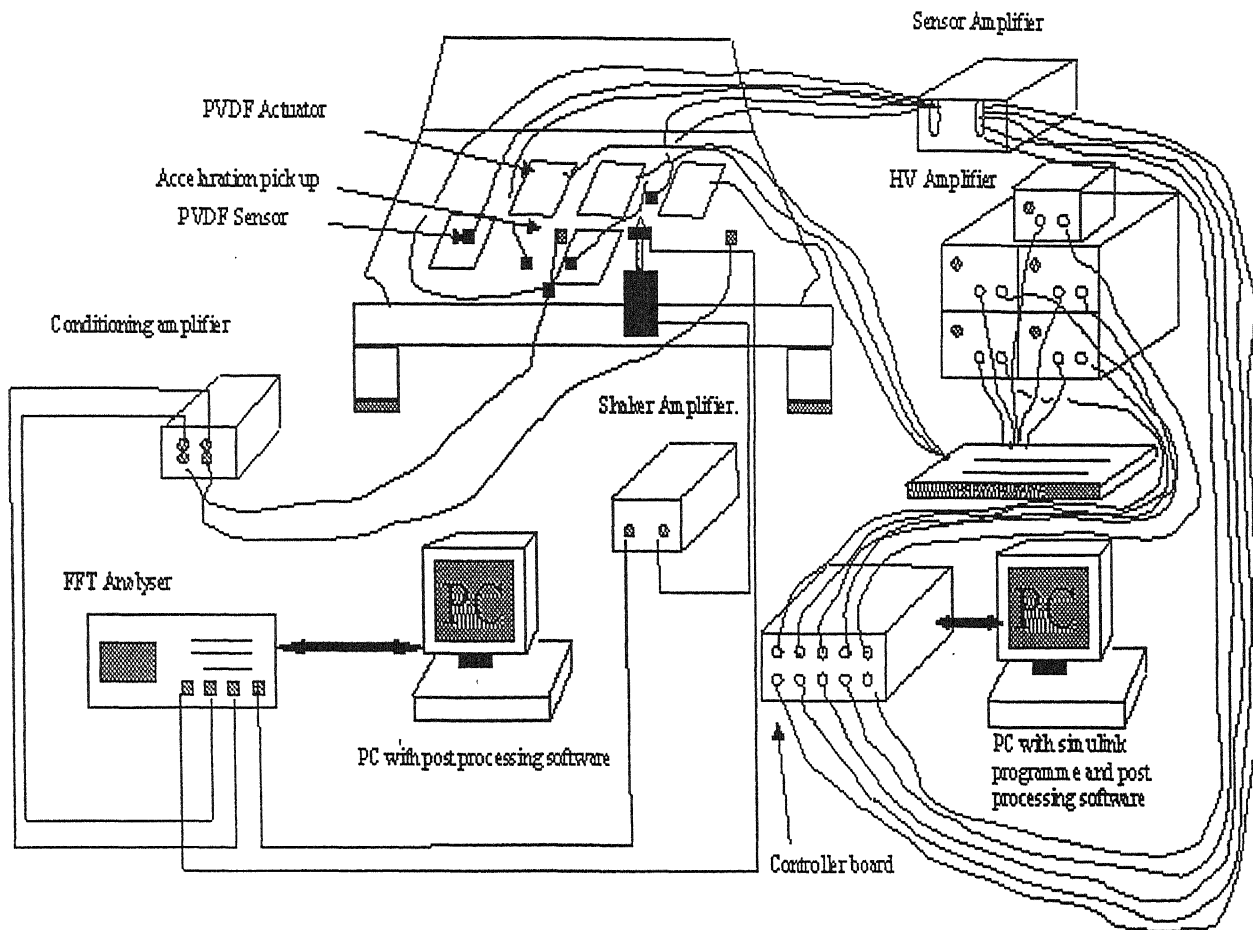


Fig 6.20 : Experimental set up for control of the car structure

The only difference between the experiment with the car structure and the beam is that PVDF materials are used as actuators instead of PZT. The amplification factor of the signal amplifier is set to 100. The maximum actuator voltage is limited to 230 volts so as to be well below the breakdown voltage of the PVDF material.

In the experiment, the number of controlled modes are reduced from five to three, as two of the sensors are placed wrongly during application of the sensors to the hood. Due to time shortage, three modes namely the ones at 144 Hz, 200 Hz and 237 Hz are controlled

after reconfiguring the input and output matrices. Actuators 1, 2, 3 and 4 are utilized for control of the aforementioned modes. Actuators 3 and 4 are working together to control the same mode. The sensors 1, 2 and 3 are used for observing these modes of vibrations.

In the monitor circuit, the electrodynamic shaker is used as vibration source. The excitation signal is sinusoidal covering a frequency band from 140 to 300 Hz. A photograph of the experimental set up is shown in fig 6.20 below.

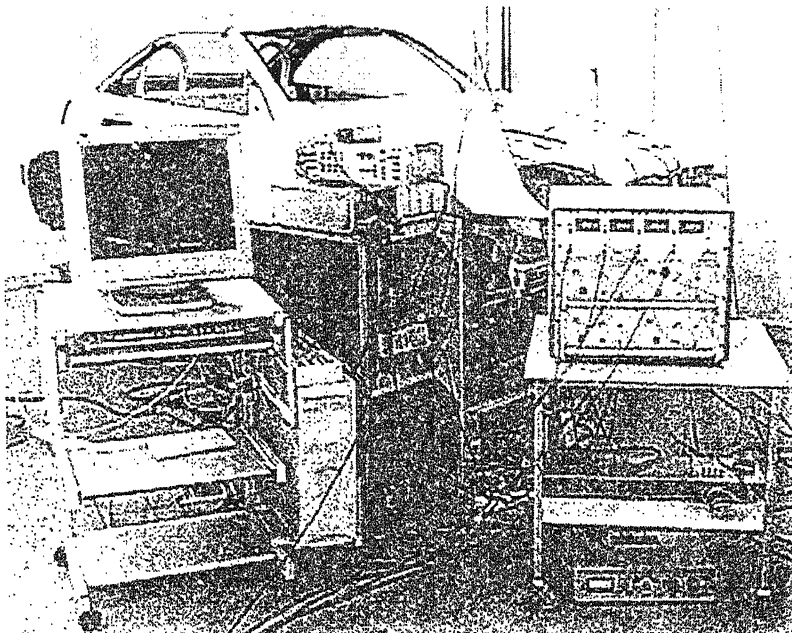


Fig 6.21 : Photograph of the experimental set up for control of Car hood vibration

6.8 Experimental Results of vibration control

The sensors 1,2 and 3 are found to give a good condition number of 4.5 to observe these three modes. The actuators 1, 2 and 3&4 are used for control of the structure.

The results of acceleration measurements of two accelerometers placed at two different positions which does not lie on the nodal lines of the three modes controlled are shown in fig. 6.16. These accelerometer plots are obtained by exciting the structure with sinusoidal excitation and sweeping through the frequency range with a PI controlled force of 4N. It is observed from the figures that the acceleration of the controlled modes are

significantly reduced. It is clear from the second accelerometer plot that a good reduction of acceleration is obtained for mode 2 (200 Hz) and mode 3 (237 Hz), respectively.

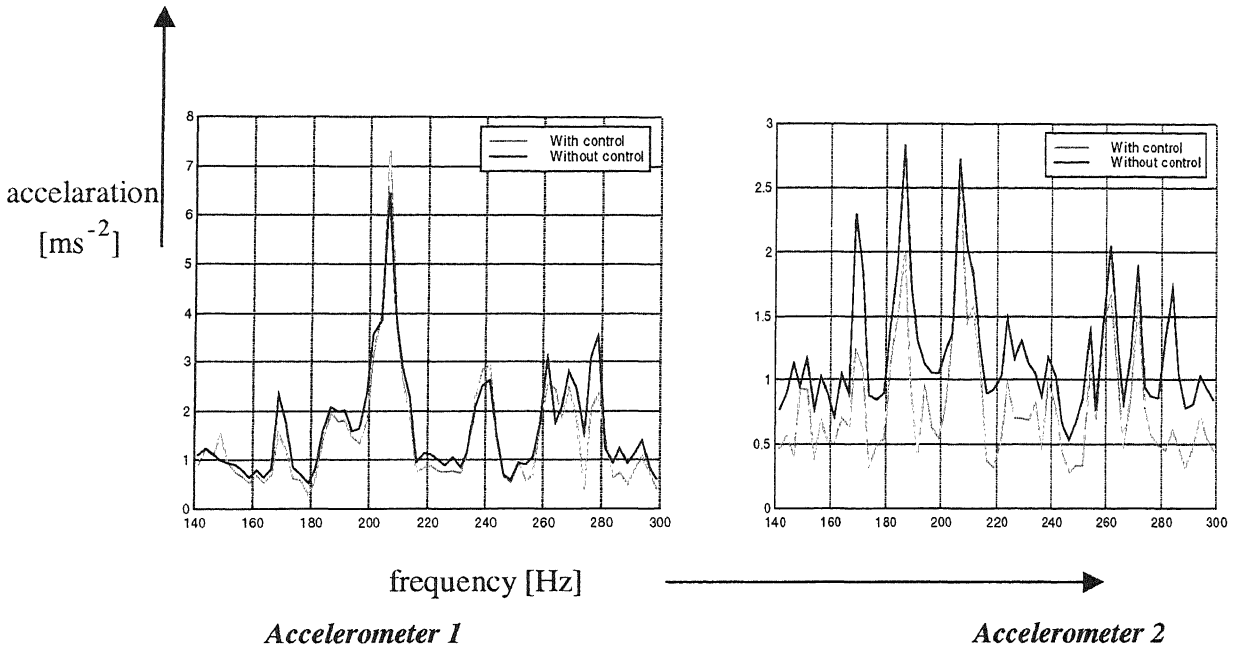
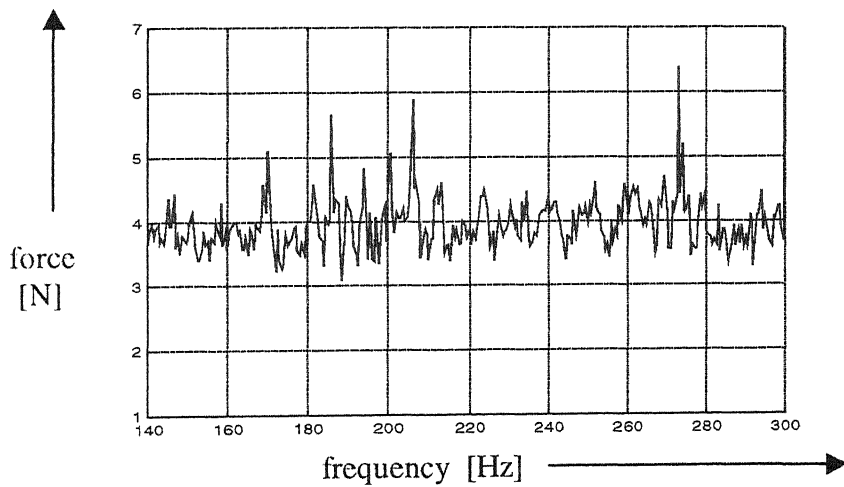


Fig 6.22 : Measured acceleration at two points on the hood

A sound pressure measurement with three microphones located at the center and the edges of the hood is done both with and without control. The results for the three microphones are summed up in fig 6.24. The readings are obtained after exciting the structure with a controlled force of 4 N which is implemented with the help of a PI-algorithm. The force variation over the frequency range is shown in fig 6.23. It is clear from the figure that all microphones which give the local sound pressure at their locations recorded an average decrease of 3 dB over the whole frequency range. Though this is a small value, a reduction of 5-6 dB is obtained for the controlled modes.



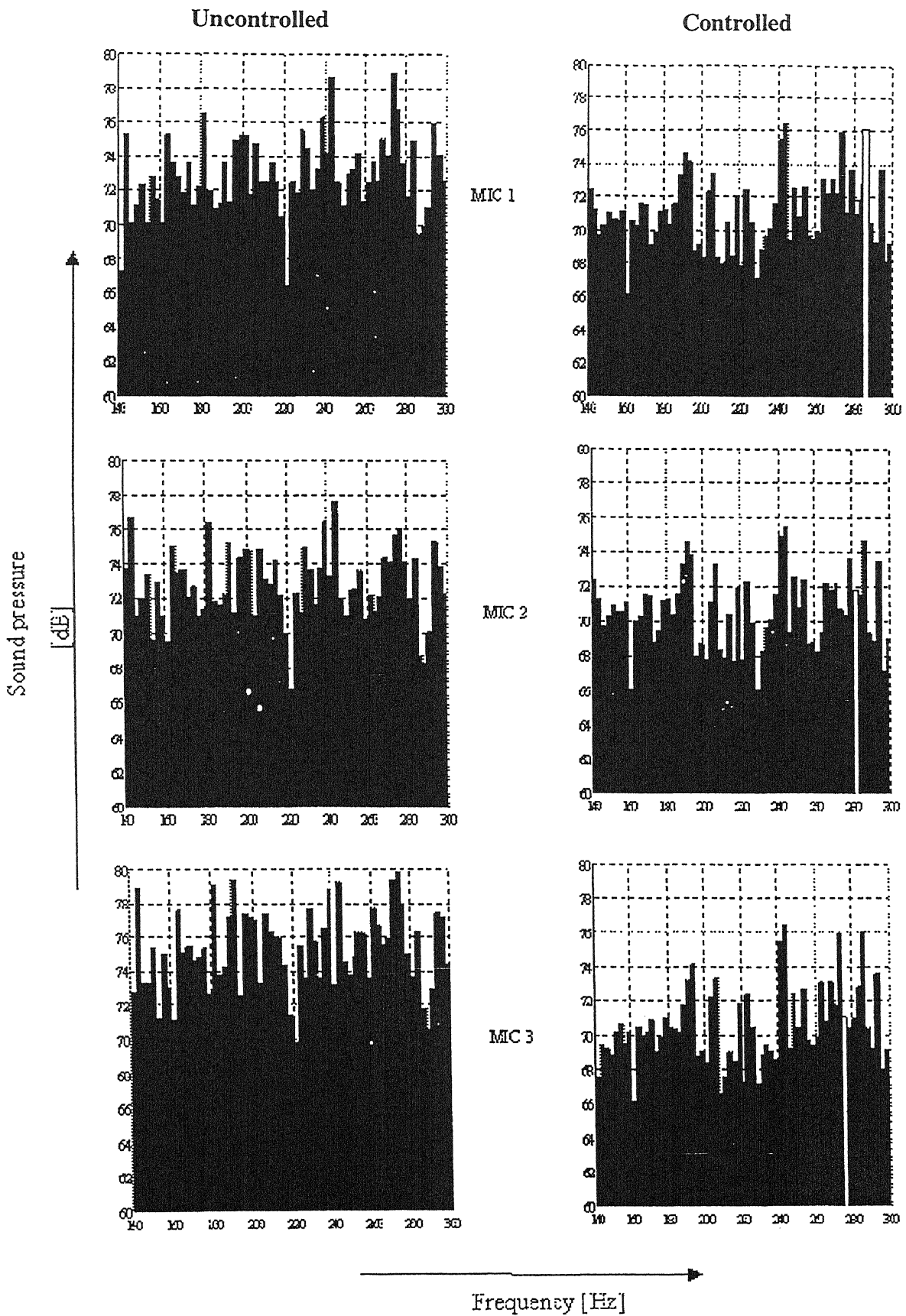


Fig 6.24 : Sound pressure measurement of the car hood with and without control

The fig 6.25 shows the modal velocity vs time plot for the control of mode with eigen frequency 237 Hz. This mode is the 3rd mode for control and hence the third modal velocity has the maximum amplitude, thus showing that the modal filter is working properly. The plot shows the modal velocity - time plot both before and after control.

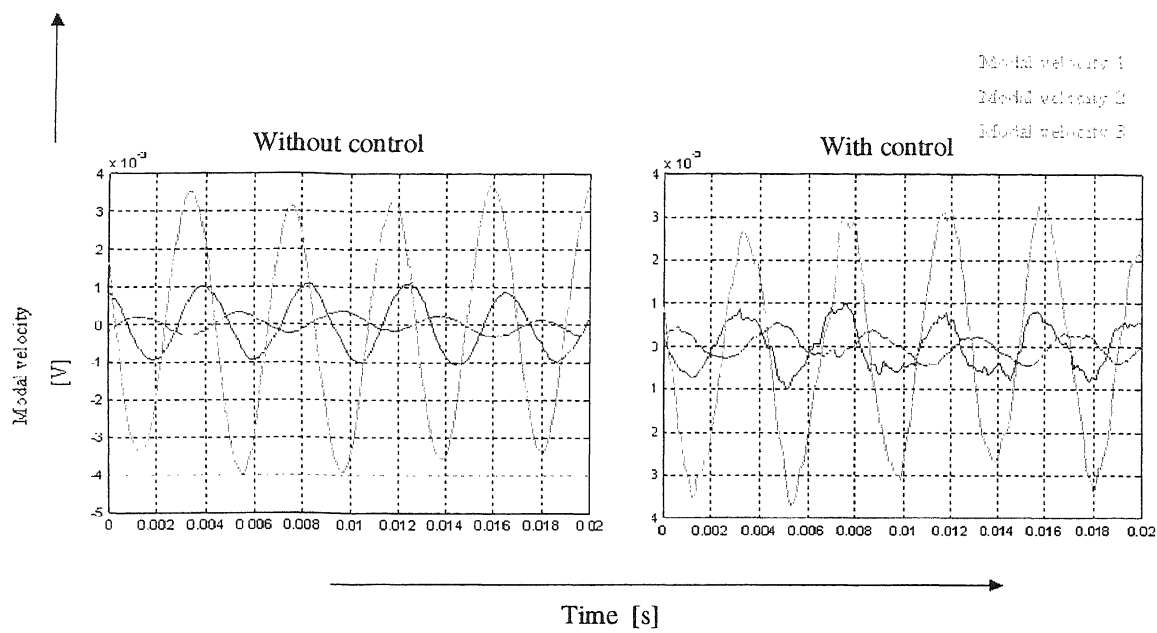
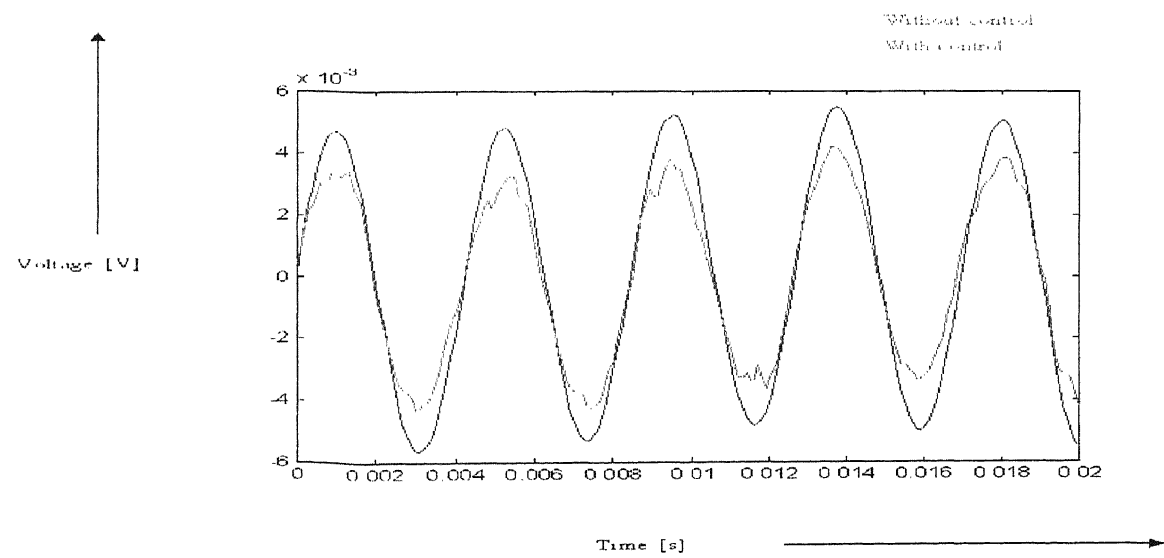


Fig 6.25 : Modal velocity – time plot for the third mode of control – 237 Hz

A comparison plot of the 3rd modal velocity of the third control mode – 237 Hz, before and after control is shown in fig 6.23. It is clear from the figure that there has been a reduction in the velocities thus showing that the structural vibration of this mode has been reduced.



Effect of passive coat

The active modal control was also carried out after applying the passive damping coat on to the bottom of the hood. Fig 6.27 shows the Sound pressure- frequency plot for the excitation of the hood with passive layer. A constant sinusoidal excitation of magnitude 9 N was applied on to the structure.

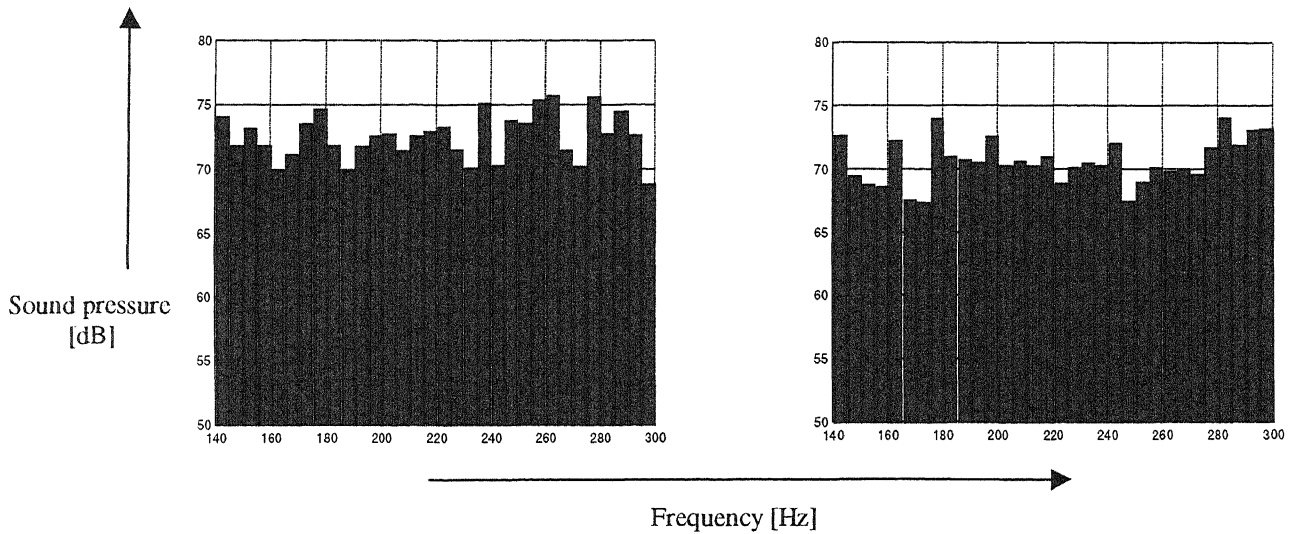


Fig 6.27 : Sound pressure measurement of hood vibration control with passive coat

The acceleration – frequency plot of the vibration level is also obtained by placing an accelerometer on one of the most vibrating parts of the hood. This is shown in fig 6.26.

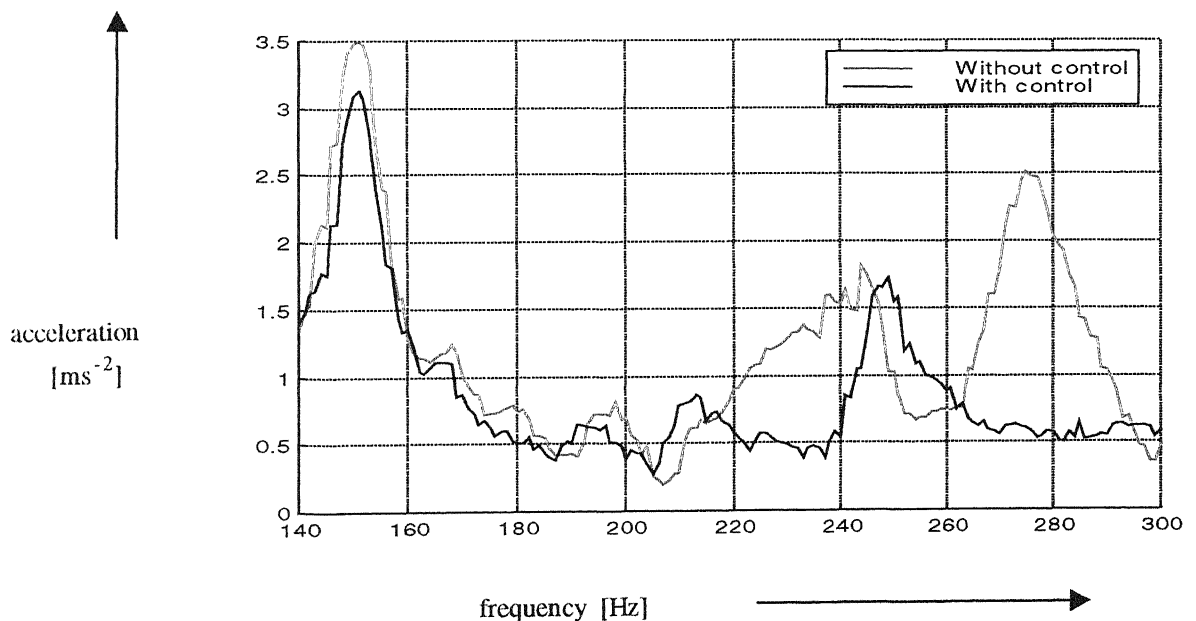


Fig 6.28 : Measured acceleration of hood vibration control with passive coat

Chapter 7

Summary

Modal filtered feedback has been applied to control the structural and acoustic response of the vibration of a car hood using discrete PVDF actuators and sensors. For this a pretest has been conducted by controlling the vibration of a simply supported beam. After modelling the beam with actuators and sensors, the modal superposition has been utilised to obtain the modal input, B and output, C matrices. Independent modal space control (IMSC) is utilised to control the first four modes of the beam vibration.

The success of the vibration control of the beam has been extended to achieve the structural and acoustic control of a car hood. The modal information, namely the modal form functions, eigen frequencies and the damping ratios has been obtained after an experimental modal analysis. The modes which radiate more sound have been identified with the help of a sound pressure measurement set up. The mode shapes have been converted into an analytical closed form by doing an interpolation. The actuators and sensors have been placed on the structure based on the sensor and actuator performance indices. The vibration of three modes of the car hood in the lower frequency band have been controlled.

A hybrid active-passive control has been investigated by attaching a viscoelastic coating on to the bottom of the car hood. The experimental results show that this approach holds much promise in reducing the sound radiation over a wider frequency range.

The following have been achieved :

- control of the first four modes of the vibration of a simply supported beam.
- structural and acoustic control of three modes of a car hood.
- active – passive hybrid control of the vibration and sound radiation of a car hood.

Chapter 8 :

Conclusion

The experiments with the car hood and the beam have shown that the modal controller works with a high efficiency and that vibration can be reduced successfully over a wide frequency band. The concept used has its limitations in the sense that the deviations by the curve fitting and truncation of residual modes, which reduce the accuracy and lead to sub optimal vibration reduction. In addition it has been observed that a hybrid passive and active treatment for vibration and noise reduction has larger implications in the control of sound radiation of a structure as it enables the sound reduction over a wide frequency band.

Scope for future work

It is suggested that the above work can be extended to control more than three modes of the car hood. This can be achieved by designing the actuator and sensor locations to control more modes. A better performance in vibration reduction could then be observed as more energy could be applied into the structure. In addition, a higher level of adaptation could be achieved by going in for unconstrained algorithms such as the adaptive feedforward control where the input to the structure evolves with time as a function of changing environmental or operational conditions. It would also be worthwhile to investigate the effectiveness of modal control over other direct output feedback algorithms such as the Positive position feedback.

Bibliography and References

1. **Fuller, C., Elliott, S. and Nelson, P.** : (1996), *Active control of Vibration* , Academic Press, London.
2. **Preumont, A.** : (1997), *Vibration Control of Active Structures – An introduction*, Kluwer Academic Publisher.
3. **Clark, R., Saunders, W. and Gibbs, G.** : (1998), *Adaptive structures , Dynamics and control* , John Wiley and Sons, Inc.
4. **Gawronski, W.** : (1998), *Dynamics and control of structures*, Springer-Verlag, Inc.
5. **Maia, N., Silva, J.** : (1997), *Theoretical and Experimental modal analysis*, Research Studies Press, England.
6. **Tzou, H.** : (1993), *Piezoelectric Shells* , Kluwer Academic Publishers.
7. **Meirovitch, L.**: (1990), *Dynamics and control of structures*, John Wiley, New York.
8. **Stöbener, U. and Gaul, L.** : (1999), *Active control of plate vibration by discrete PVDF Actuator and sensor segments*, Ninth International conference on Adaptive structures and Technologies, pp. 349-358 , Technomic Co., Inc., Lancaster, PA 17601.
9. **Stöbener,U. and Gaul, L.** : (2000), *Active vibration and noise control for the interior of a Car body by PVDF actuators and sensors segments*, 10th International conference on Adaptive structures and Technologies, pp. 457-464, Technomic Co., Inc., Lancaser.
10. **Albrecht, H., Stöbener,U. and Gaul, L.** : (2000), *Sensor and Actuator Design Methods in Active vibratoin Control for Distributed Parameter Structures*, Presentation, international Centre for Mechanical sciences, Udine.

11. **Hornung, T., Reimerdes, H. and Günnewig, J.** : (1998), *Modal Analysis, Modelling and Control of Vibration Systems with integrated Active Elements*, Proceedings of the Euromech 373 Colloquium.
12. **Wang.T., Rogers, C.:** (1991), *Laminate Plate theory for Spatially Distributed Induced Strain Actuators*, Journal of Composite materials, pp. 433-452 , Vol 25.
13. **Mackiewicz, A. , Holnicki-Szulc, J. and Lopez-Almansa, F.** : (1996), *Optimal sensor location in active control of flexible structures*, AIAA Journal, Vol 34, No 4, Technical Notes.
14. **Clark, R. and Fuller,C.** :(1992), *Modal sensing of efficient acoustic radiators with Polyvinylidene flouride distributed sensors in active structural acoustic control approaches*, Journal of Acoustical society of America, pp. 3321-3329 , Vol 91.
15. **Lee, C.** : (1990), *Theory of Laminated Piezoelectric plates for the design of Distributed Sensors / Actuators. Part1 : governing Equations and Reciprocal Relationships*, Journal of Acoustical society of America, pp. 1144-1158, Vol 87.
16. **Chandrashekara,K., Agrawal,A.:** (1993), *Active vibration control of Laminated Composite plates using Piezoelectric devices : A finite element approach*, Journal of Intelligent Material systems and structures, pp. 496-507 , Vol 4.
17. **Hagood,W., Walter,H., Chung and Andreas** : (1990), *Modelling of Piezoelectric Actuator Dynamics for Active Sturctural Control*, Journal of Intelligent Material systems and structures, pp. 327-353, Vol 1.
18. **Inman,D.** : (2000), *Active modal control for Smart strucutres*. Reivew paper, Smart materials and structures.
19. **Janocha,H.** : (1999),*Adaptronics and Smart Structures-Basics, materials, design,and applications*, Springer Verlag , Berlin.

20. **Press,W., Teukolsky,S., Vatterling,T. and Flannery,B.** : (1994), *Numerical Recipes in C .The art of scientific computing*, Cambridge university press.

21. **Hwang,W., Park,H. and Hwang,W.** : (1993), *Vibration control of a Laminated plate with piezoelectric Sensor/Actuator ; Finite element formulation and Modal analysis*, Journal of Intelligent material system and structures, pp. 317-329, Vol 4.

22. **Crawley,E. and Luis,J.** : (1989), Use of Piezoelectric actuators as elements of Intelligent structures, AIAA Journal, pp1373-1385.

23. **Kwon Yang,W., Hyo Choong Bang** : (1997), *The finite element method using Matlab*, CRC press.

24. **Stöbener,U. and Gaul,L.** : (2000) , *Active vibration and noise control by hybrid active acoustic panels*, Proceedings of GAMM , Göttingen.

25. **Hermman Shen, M.** : (1994), *Analysis of beams containing piezoelectric sensors and actuators*, *Smart materials and structures* , pp 439-447, Vol 3 .

26. **Padma Akella, Xin Chen, Declan Huges & John,T.** :(1994), *Modelling and control of smart structures with bonded piezoelectric sensors and actuators*, SPIE proceedings, Orlando, Florida.

§§ Appendix 1:

Linear Piezoelectric Theory

Linear piezoelectric theory couples the electric and mechanical fields. In this appendix the linear piezoelectric theory is reviewed. This theory is based on the quasi-static assumption in which the electric field is balanced with the elastic field so that these two fields can be decoupled at a given time instant. The direct and converse piezoelectric effects are written as :

$$\{D\} = [e]\{S\} + [\varepsilon^S]\{E\}, \quad (A.1.1)$$

$$\{T\} = [c^E]\{S\} - [e]^T\{E\}. \quad (A.1.2)$$

where $\{T\}$ is the stress tensor (second order); $\{S\}$ is the strain tensor (second order); $\{E\}$ is the electric field vector; $\{D\}$ is the electric displacement vector; $[c^E]$ is the elasticity tensor (4th order) evaluated at constant electric field; $[e]$ is the tensor of piezoelectric stress coefficients (3rd order); $[e]^T$ is the transposed tensor of $[e]$; $[\varepsilon^S]$ is the dielectric tensor (2nd order) evaluated at constant strain. If the piezoelectric tensor $[e]$ is set to zero, the above two equations become the conventional dielectric and Hook's equations.

There are a number of ways to write down the elastic, piezoelectric and dielectric governing equation, of which the strain and electric displacement is most common and outlined below:

$$\{S\} = [s^E]\{T\} + [d]^T\{E\}, \quad (A1.3)$$

$$\{D\} = [d]\{T\} + [\varepsilon^T]\{E\}. \quad (A1.4)$$

where $[d]$ is the piezoelectric strain constant matrix and $[s^E]$ is the compliance matrix evaluated at constant electric field.

The various relationships between the elastic, piezoelectric and dielectric constants are outlined below:

$$[c^E] = [s^E]^{-1} \quad (A1.5)$$

$$[e] = [d][c^E] \quad (A1.6)$$

$$[\varepsilon^S] = [\varepsilon^T] - [e][d]^T \quad (A1.7)$$

§§ Appendix 2:

Fourth Order Runge-Kutta Time Integration For Beam vibration Simulation In Modal Coordinates

For simulation of adaptive structures without control feedback loop, it can be advantageous to use direct time integration schemes to solve the second-order equations of motion. Examples are Houbolt, Wilsons- θ and Newmark schemes. The existence of control feedback loops, especially with actuator, sensor or observer dynamics makes the direct time integration schemes difficult and hence Implicit and Explicit schemes based on the first-order state differential equation are preferred. The well know among them is the old workhorse – The Runge-Kutta method.

The steps for the time integration of the Modal state-space equation is outlined below:

- Assigning the value of the load p_z on the structure.
- Evaluation of the matrices A, B, C, G and force vector h .
- Determination of the initial values of the state space vector x .
- Carrying out the time integration of equation (A 2.1) with definite time step t .

$$\dot{x} = Ax + B(-G C^{-1}x) + hp_z. \quad (A 2.1)$$

The fourth order Runge-Kutta method requires four evaluations of the right hand side of the above equation per step size t . For the integration from the interval t_k to t_{k+1} the evaluations can be done as shown below

$$\Delta x_{1k} = \dot{x}_k \Delta t, \quad (A 2.2)$$

$$\Delta x_{2k} = \left(\dot{x}_k + \frac{\Delta x_{1k}}{2} \right) \Delta t, \quad (A 2.3)$$

$$\Delta x_{3k} = \left(\dot{x}_k + \frac{\Delta x_{2k}}{2} \right) \Delta t, \quad (A 2.4)$$

$$\Delta x_{4k} = \left(\dot{x}_k + \frac{\Delta x_{3k}}{2} \right) \Delta t, \quad (A 2.5)$$

Now the state-space vector for the $(k+1)^{th}$ time step can be written down as :

$$x_{k+1} = x_k + \frac{\Delta x_{1k} + \Delta x_{2k} + \Delta x_{3k} + \Delta x_{4k}}{6} \quad (A 2.6)$$

The integration can be continued till the required final time limit.

§§ Appendix 3:

Condition Of A Matrix By Singular Value Decomposition (SVD)

Any $m \times n$ matrix A can be factored into a set of three matrices $[U]$, $[w]$ & $[V]$ with special characteristics. The matrices $[U]$ and $[V]$ are orthogonal and $[w]$ is diagonal. This factoring is called SVD. Thus,

$$[A] = [U] [w] [V]^T \quad (A\ 3.1)$$

If the matrix A is square, $N \times N$ then, U , V , and w are all square matrices of the same size. Their inverses are also trivial to compute. It follows immediately that the inverse of A is

$$A^{-1} = V \cdot [diag (1 / w_j)] \cdot U^T \quad (A\ 3.2)$$

The only thing that can go wrong with this construction is for one of the w_j 's to be zero, or (numerically) for it to be so small that its value is dominated by round off error and therefore unknowable. If more than none of the w_j 's have this problem, then the matrix is even more singular.

Formally, the condition number of a matrix is defined as the ratio of the largest (in magnitude) of the w_j 's to the smallest of the w_j 's. A matrix is singular if its condition number is infinite and it is ill-conditioned if its condition number is too large, that is, if its reciprocal approaches the machine's floating-point precision, For e.g. less than 10^{-6} for single precision or 10^{-12} for double .

§§ Appendix 3:

Condition Of A Matrix By Singular Value Decomposition (SVD)

Any $m \times n$ matrix A can be factored into a set of three matrices $[U]$, $[w]$ & $[V]$ with special characteristics. The matrices $[U]$ and $[V]$ are orthogonal and $[w]$ is diagonal. This factoring is called SVD. Thus,

$$[A] = [U] [w] [V]^T \quad (A\ 3.1)$$

If the matrix A is square, $N \times N$ then, U , V , and w are all square matrices of the same size. Their inverses are also trivial to compute. It follows immediately that the inverse of A is

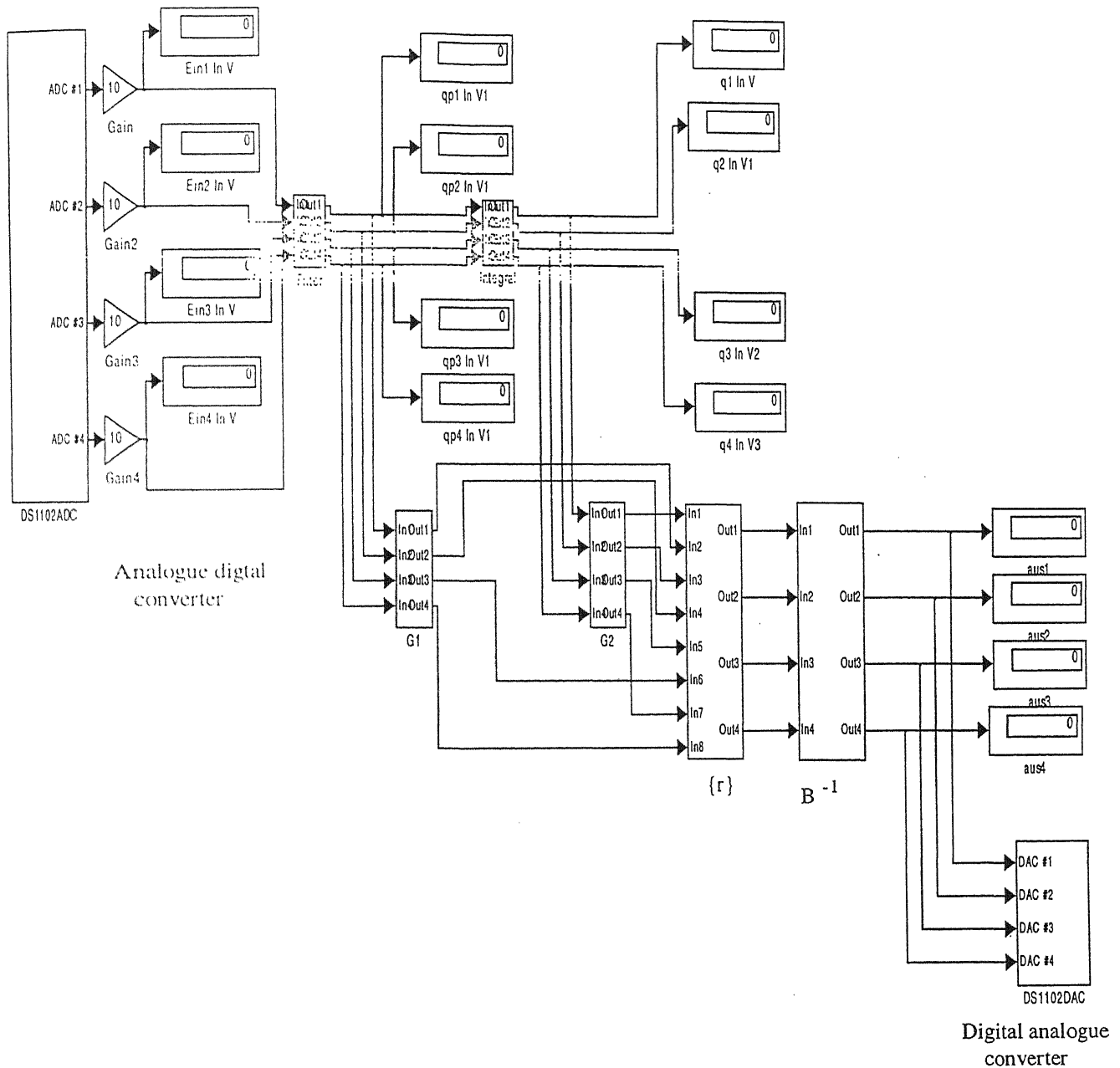
$$A^{-1} = V \cdot [\text{diag}(1/w_j)] \cdot U^T \quad (A\ 3.2)$$

The only thing that can go wrong with this construction is for one of the w_j 's to be zero, or (numerically) for it to be so small that its value is dominated by round off error and therefore unknowable. If more than none of the w_j 's have this problem, then the matrix is even more singular.

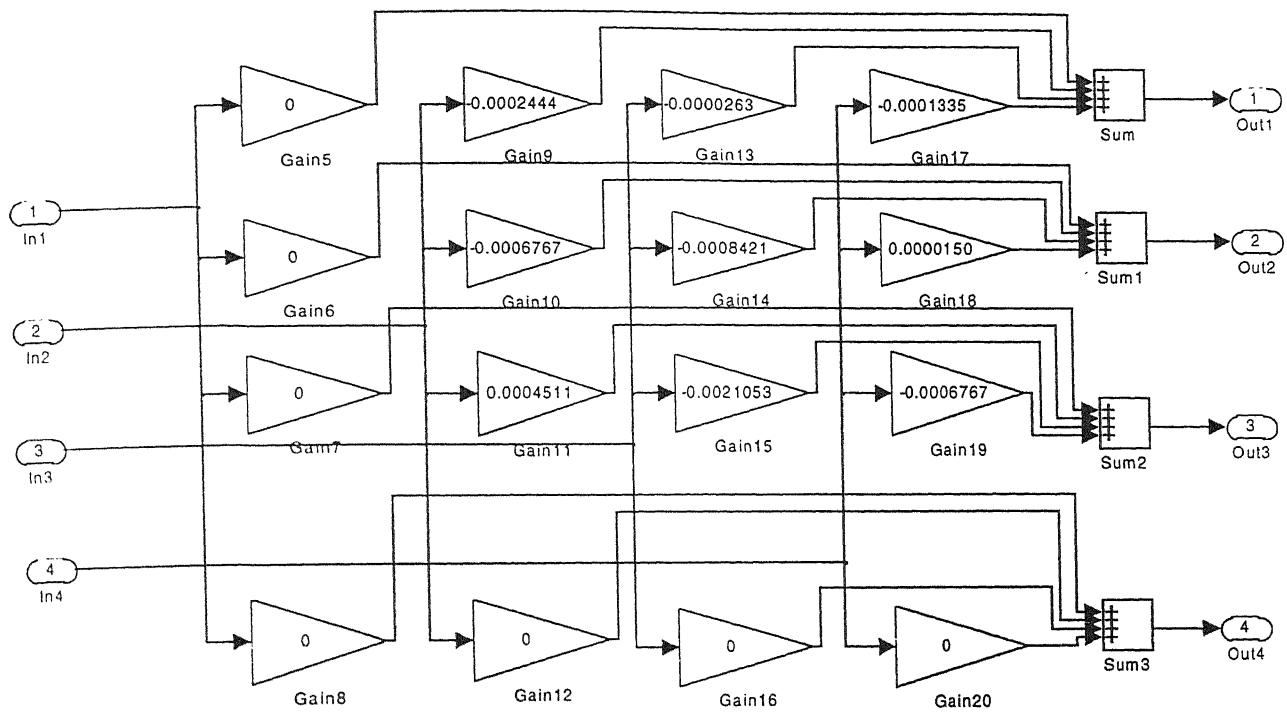
Formally, the condition number of a matrix is defined as the ratio of the largest (in magnitude) of the w_j 's to the smallest of the w_j 's. A matrix is singular if its condition number is infinite and it is ill-conditioned if its condition number is too large, that is, if its reciprocal approaches the machine's floating-point precision, For e.g. less than 10^{-6} for single precision or 10^{-12} for double .

§§ Appendix 4:

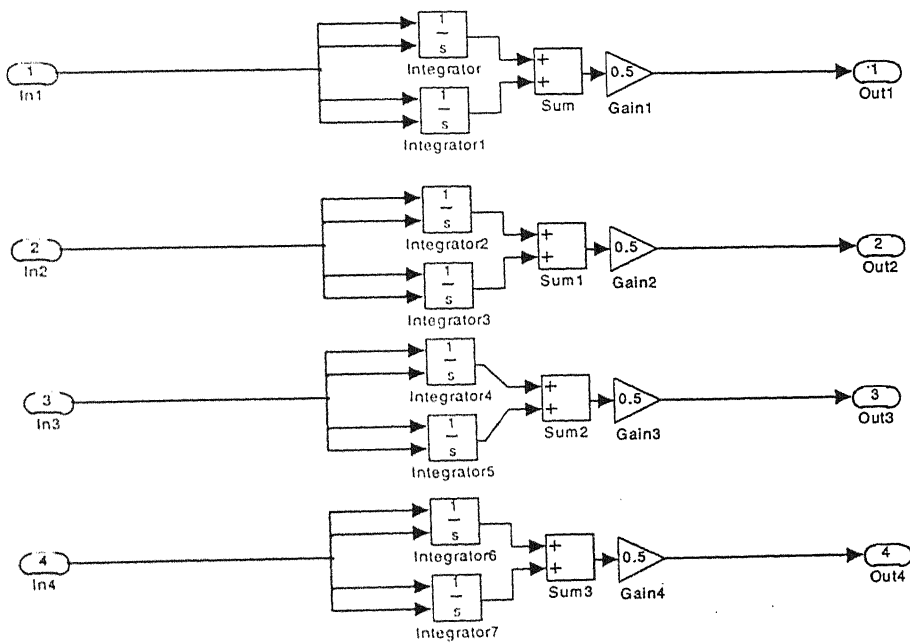
Flow diagram of modal control in Matlab Simulink used for controlling four modes.



Modal filter

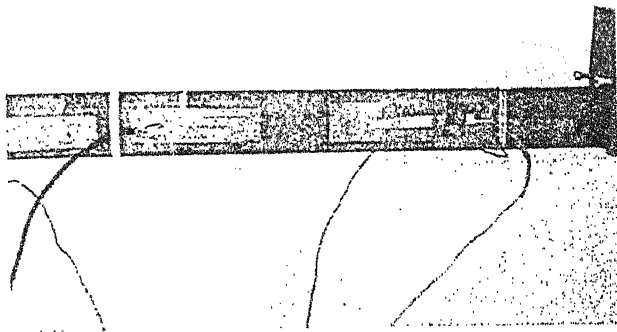


Time integrator

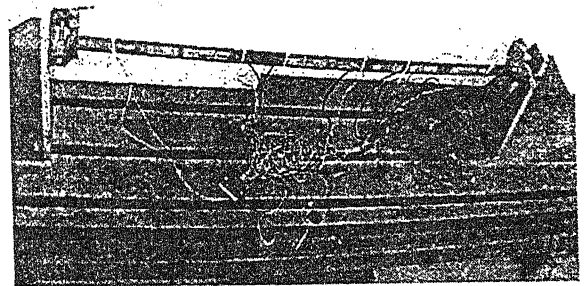


§§ Appendix 5:

Photographs of the beam and car hood specimens

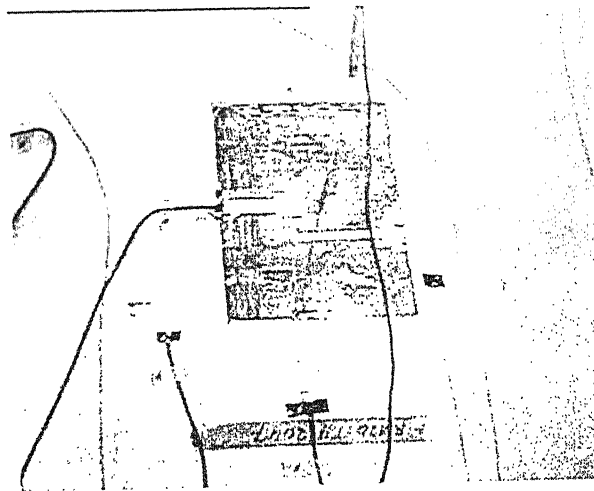


[a]



[b]

[a] and [b] Beam with Sensors and actuators



[c]

[c] Piezoelectric actuator and sensor on the car hood

33654

The book is to be returned on
the date last stamped.

[illegible]

A133654

TH
AE/2001/M
K96a
A133654